Macroscale Modelling Of Ice Drift Inside An Offshore Wind Farm In The Baltic Sea

Vince Deelman

Delft University of Technology

TU Delft

Macroscale Modelling Of Ice Drift Inside An Offshore Wind Farm In The Baltic Sea

by

Vince Deelman

5142490

Dr. ir. Hayo Hendrikse	Delft University Of Technology
Dr. Mukund Gupta	Delft University Of Technology
Dr. Tim Hammer	Delft University Of Technology
Project Duration:	November, 2024 - June, 2025
Faculty:	Civil Engineering and Geosciences

Cover: Image generated using 4o image generation tool from ChatGPT (OpenAI, 2025).

TU Delft

Preface

First of all, I would like to thank my supervisors Hayo, Tim and Mukund. Before starting this thesis, I had not attended any courses on ice mechanics. It was a challenge to get familiar with all the theory regarding ice mechanics, and I did not have any knowledge on image processing. As Hayo pointed out when he explained this thesis topic to me, it would be a challenging topic, and it lived up to the expectation. A major workload of this thesis turned out to be figuring out a methodology to connect satellite imagery to running ice fields within SIBIS. I think the main challenge was connecting all the pieces of this methodology without introducing any undesired errors. Furthermore, I learned a lot from dealing with computational resource-limitations by being very strict in my selection of simulations. I should give a lot of credit to Hayo, Tim and Mukund for guiding me through this process and pointing me towards the right direction. I really appreciate all the time you took for answering my questions, and I enjoyed all the informal meetings we had while looking at animations of drifting ice.

I should give a lot of credit to Matthias Rabatel and Nicolas Serré for all the help they provided during this thesis. Without the updated SIBIS mesh engine I would not have been able to perform the simulations I was planning to. This allowed me to run simulations for several days without any errors and to make such nice visualizations of the simulation results.

I also want to thank the SESAM-ICE JIP and partners, in particular Equinor and DNV for allowing me to use the software SIBIS as part of my thesis work.

To my mother, thank you for your endless care and involvement throughout my studies in the past years.
To my father, thank you for all the bad jokes and inspiring me to pursue a PhD abroad.
Julia, I'm still not sure if you actually know what my thesis is about - and I really appreciate that.

Elise, you contributed much more to this thesis than you probably realize. Your weekly photos of "de knutsel van de week", the early mornings at the train station, and your reminders to take a break helped me through this.

My time in Delft has officially come to an end. I think it's safe to say all the experiences of the past years exceeded far beyond my expectations. I have been to all the highlights across the West Coast of the United States and Canada, experienced life in Texas for a month and did multiple teaching assistant jobs. All my friends made these past 6 years living in Delft fly by and made it so enjoyable.

This thesis was my first introduction into both doing research and the field of Arctic engineering. Fortunately, this does not mark the end of my academic journey and my experience with ice. I am sure I will make much more valuable memories during my life in Norway in the coming 3 years.

Vince Deelman
Delft, May 2025

Summary

In the past, development of offshore wind energy was mainly focused on ice-free regions, but increasing demand has introduced the need for development in sub-Arctic regions, such as the Southern Baltic Sea. The expanding offshore wind development in this area not only presents new opportunities, but also new engineering challenges. In these regions, sea ice may drift against the foundation of offshore wind turbines, introducing dynamic ice loads which can significantly affect the design and safety of offshore wind turbines.

Extensive research has been performed on the ice-structure interaction and the resulting ice-induced vibrations. However, this thesis studies the ice-structure interaction on a macroscale, considering how ice fields interact with offshore wind farms as a whole. The main motivation for this focus is that the presence of multiple structures instead of a single structure will affect the ice drift- and growth within an offshore wind farm. Currently, the designers of offshore structures often assume that the ice drift speed may be correlated to the surface wind speed at 10 m height by a constant factor (Hendrikse, 2024). However, the presence of both a single- and multiple turbines may slow down the ice. Previous research indicates that for low ice velocities, severe loading can occur in the form of intermittent crushing and multi-modal ice structure interaction (Hammer et al., 2023). The presence of multiple turbines may also promote ice growth during winter - leading to stationary ice - as they can function as anchor points for the ice to grow onto. If the wind picks up, the (re)-initiation of the stationary ice sheet may lead to simultaneous loading of all turbines at low relative velocities, resulting in severe ice-induced vibrations (Hammer et al., 2023). This thesis therefore aims to explore the influence of an offshore wind farm on the ice drift speed, leading to the consideration of two scenarios: (1) the drift of an ice floe field that originate from outside the offshore windfarm and (2) the drift of an ice floe that is frozen in around the turbines. This is formulated in the main research question:

How does the presence of an offshore wind farm affect the ice drift speed for both an ice floe field that originates from outside the offshore wind farm and a grown-in condition in the Southern Baltic Sea?

The first objective of this thesis was to establish if the ice drift speed can indeed be correlated to the surface wind speed by a constant factor in the presence of multiple structures. The second objective was to acquire the combinations of ice thickness and wind speeds for which the motion of a frozen in ice sheet could be (re)-initiated.

This thesis applies image processing to the satellite images that were captured from the Baltic Sea during the Copernicus programme. The resulting ice floe size distribution is then coupled to a synthetic floe field generator that randomizes ice floe shapes, orientation and placement within predefined boundaries. This enables the generation of ice floe fields having different sea ice concentrations and maximum floe sizes. These ice floe fields are then converted to SIBIS to enable performing simulations. This thesis only considers ice drift in 2D in the horizontal plane of motion, which implies that bending, rafting and buckling of ice are not modelled, as this concerns ice that is forced up or down due to compressive stress. Rather, the ice-structure interaction is dominated by crushing and splitting. The ice drift is simulated on a timescale up to a few hours and a scaled-down version of a typical offshore wind farm was used due to limitations of computational resources. Whereas typical offshore wind farm layouts consist of 50 turbines, this thesis adopts layouts using an evenly spaced 3 x 3 and 4 x 4 grid, having an inner distance of 1 km.

When the floes are initially positioned outside the offshore wind farm, the results shown that the correlation between the ice drift speed and the wind speed is lost during the ice-structure interaction. The lowest ice drift speeds are found to occur for the floes that are directly in contact with the turbines, experiencing an average velocity reduction of 41.6% as compared to the case without turbines present. These floe speeds are in the range where they can promote intermittent crushing and multi-modal ice-structure interaction. Furthermore, the results show that ice floe velocities at the turbines are affected by the interaction among ice floes that are not in direct contact with the turbines. Due to the rotation

of ice floes around structures, the velocities at a turbine may also be influenced by the presence of neighbouring turbines. These effects lead to a misalignment of the ice- and wind loading, highlighting the importance of macroscale modelling.

Results for the frozen-in scenario indicate that (re)-initiation of the stationary ice sheet may occur for several combinations of wind speed and ice thickness that are typical for the Southern Baltic Sea. The critical wind speed across multiple offshore wind farm layouts - and corresponding ice sheet area - was found to depend on the critical wind drag force. This is the wind drag force for which the resistance of the turbines to the motion of ice is exceeded. For the case of an offshore wind farm modelled after the existing Baltic Eagle wind farm layout, it was found that all wind speeds above 26 m/s can lead to simultaneous loading of all turbines.

For both scenarios, it was not validated how using a low number of turbines - as compared to a real-life offshore wind farm such as the Baltic Eagle wind farm - affects the results that are presented in this thesis. For the simulations in which the floes originate from outside the offshore wind farm, this thesis identifies several effects - such as the spatial extend of the speed reduction across the floe field - that can be attributed to the presence of very large floes within the ice floe field. Furthermore, it is expected that the shielding of secondary- and tertiary rows of turbines may be related to the obstruction of these very large floes. To further explore these phenomena, a high number of simulations should be performed - that include a high number of turbines - to address the stochastic behaviour of an ice floe field interacting with an offshore wind farm. For the grown in scenario, the sensitivity of the identified critical wind speeds to changes in the offshore wind farm layout and the geometry of the ice sheet has not been validated.

Furthermore, this thesis assumes a water current equal to zero, as both the magnitude and the direction of the current in the Baltic Sea were found to be highly varying. However, an offset between the direction of water currents and wind is commonly observed under natural conditions. Hammer et al. (2023) showed that misalignment of wind- and ice loading direction can result in ice-induced vibrations developing for higher ice drift speeds as compared to an aligned scenario. This effect has thus not been incorporated in this thesis. Finally, the crack paths are only drawn in straight lines during splitting and crack propagation is not modelled. It is speculated that this can affect the macroscale ice drift.

Contents

Nomenclature

Symbols

Symbol	Definition	Unit
x_{min}	Lower boundary of floe size within power-law regime	km^2
r_{min}	Lower bound floe radius in synthetic floe field generator	m
x_{bound}	Upper boundary of floe size within power-law regime	km^2
x_{max}	Maximum observed floe size	km^2
r_{max}	Upper bound floe radius in synthetic floe field generator	m
α	Power law exponent floe size distribution	[-]
Na	Nansen Number	[-]
C_w^F	Ice-water form drag coefficient	[-]
C_w^S	Ice-water skin drag coefficient	[-]
C_a^F	Air-ice form drag coefficient	[-]
C_a^S	Air-ice skin drag coefficient	[-]
ρ_w	Density water	[kg/m^3]
ρ_a	Density air	[kg/m^3]
f	Coriolis parameter	$1/s$
γ	Wind factor	[-]
β	F_Y/F_X	[-]
F_Y	Crack opening force in lateral direction	N
F_X	Ice force in direction of relative ice-structure velocity	N
β_{min}	Minimum split force ratio	[-]
$u_{wind,10m}$	Wind speed measured at 10 m height	m/s
u_{water}	Current speed	m/s
$Hice$	Ice thickness	m
C_R	Ice strength coefficient	MPa
ρ_{ice}	Ice density	m^{-3}
σ_f	Flexural strength	MPa
K	Fracture toughness	kPa $\cdot\sqrt{\text{m}}$
E	Youngs Modulus	GPa
ν	Poisson ratio	[-]
τ	Shear strength	MPa

1 Introduction

1.1. Research Motivation and Problem Statement

The seasonal ice in the Baltic Sea imposes unique conditions, as drifting sea ice may result in high loads on offshore wind turbines when the ice floes drift against the foundations. Figure 1.1a shows an example of such icing conditions at the Nissum Bredning Vind Offshore Wind Farm during the winter of 2018. Figure 1.1b shows the grown-in Tahkoluoto offshore wind farm at the Finnish coast during winter (NREL, 2023). Over the past decade, research has been done on the dynamic loads of drifting sea ice on individual turbines, as ice action may lead to ice-induced vibrations such as intermittent crushing and multi-modal ice structure interaction (Hammer et al., 2023). The main guideline for the design of offshore structures that experience dynamic ice loads, ISO 19906, distinguishes between three ice-structure interaction regimes: intermittent crushing, frequency lock-in and continuous brittle crushing. These may be classified based on their periodicity (Hammer et al., 2022). If neither the time series of global ice load and the structural displacement indicate periodicity, the structure is not significantly interacting with the ice and vice versa. This regime is defined as continuous brittle crushing. The structure moves through the ice with small-amplitude oscillation around a mean displacement. Once periodicity is observed, interactive behaviour between the ice and the structure is likely to take place. If the global frequency of interaction is below the first eigenfrequency of the turbine, the vibration is classified as intermittent crushing. This regime occurs at very low ice drift speeds, for example 0.005 m/s for a 14 MW turbine. Once the interaction frequency is close to the natural frequency of the structure, the interaction can be classified as multi-modal interaction or as frequency lock-in, depending on the number of structural modes involved. This depends on the number of modes of the structure that contribute to the interaction. Once the response only shows vibrations in a single structural mode, it can be classified as frequency lock-in. If multiple modes are present in the response, the vibration is defined as multi-modal interaction. For Baltic Sea structures, frequency lock-in develops for ice drift speeds between 0.04 - 0.10 m/s (Hammer et al., 2022). The occurrence of these loading conditions is thus dependent on the velocity of an ice floe during interaction, as low drift speeds result in the most severe load cases (Hendrikse, 2024). However, the sea ice concentration, floe size and ice-ice interaction in an ice floe field will affect the velocities of individual floes as well. Furthermore, these parameters may be influenced by the presence of other turbines. Therefore, the ice-structure interaction should be studied on a macroscale. This means that the focus of this thesis lies on how ice fields interact with the offshore wind farm as a whole, rather than analysing local phenomena at individual turbines. An example of this macroscale modelling can be found in Figure 1.1c.

The presence of multiple structures instead of a single turbine could affect the ice drift and growth within an offshore wind farm (OWF). This is in particular relevant for the definition of the joint-probability of the occurrence of specific ice- and wind conditions, which is related to fatigue and ultimate limit state (ULS) design load cases. These conditions may occur as the presence of other turbines can slow down the ice, promoting severe load cases that occur at low drift velocities. During the design of offshore structures it is often assumed that the ice drift speed can be correlated to the wind speed at 10 m height by a constant factor. This assumption implies that the drift of ice floes is unaffected by the presence of turbines. For a single small structure that encounters ice, this may be a good approximation. However, it is unclear whether this still holds in the case of multiple structures. The turbines may act as obstructions, leading to lower drift speeds or even stationary ice due to the resistance that the structures provide (Hendrikse, 2024). The presence of turbines may also induce ice growth during extended periods of low wind speeds (Croasdale, 1975). This can result in a fully grown-in OWF, that is covered by a stationary ice sheet, and in which the turbines act as anchors for the ice. This condition is shown in Figure 1.1d. If

the wind speed picks up again, it could (re-)initiate the movement of the ice, leading to full-thickness contact as described by Croasdale (1975). The simultaneous loading of all turbines at low relative velocity has been shown to result in severe ice-induced vibrations (Hammer et al., 2023). The crushing load that can occur in this intimate contact condition is not accounted for in current design standards such as ISO 19906 alongside existing design load cases (van der Stap et al., 2024), but is likely to occur as tidal variations in the Baltic Sea are minimal (Finnish Meteorological Institute, 2025).

(a) Offshore wind turbines in icing conditions at the Nissum Bredning Vind Offshore Wind Farm in winter of 2018 (Siemens Gamesa Renewable Energy, 2018).

(b) Tahkoluoto Offshore Wind Farm at the Finnish coast during winter grown-in by sea ice (Baltic Sea, Finland) (NREL, 2023).

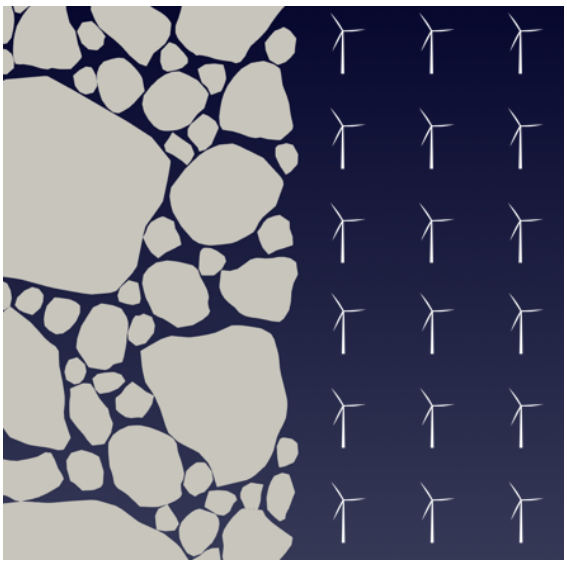

(c) Floes initially positioned outside the offshore wind farm. This is the first scenario that is studied in this thesis.

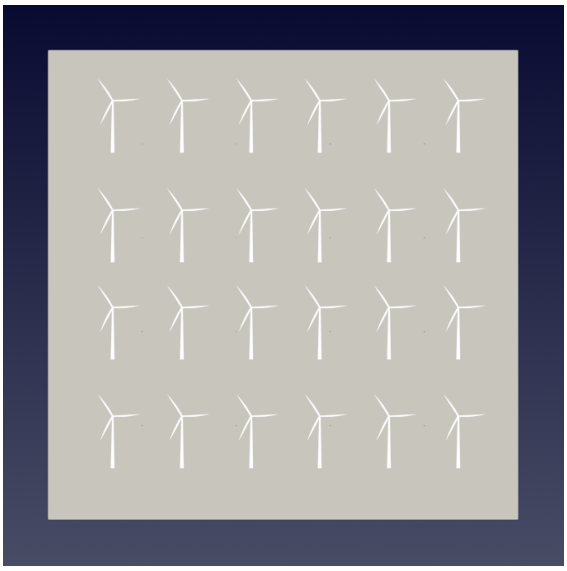

(d) Grown-in condition, which is the second scenario that is explored in this thesis.

Figure 1.1: Images of offshore wind farms encountering ice and overview of the two simulation scenarios that are considered in this thesis.

1.2. Objective and Scope

This thesis aims to address the effect of the presence of multiple structures on ice drift by simulating an ice floe field that enters an OWF in the Southern Baltic Sea. The study employs a combination of observational data from satellite images and synthetic floe field generation to obtain an ice floe size

distribution that is representative of the Southern Baltic Sea. This enables modelling of ice drift under varying floe field layouts. Two scenarios are investigated: (1) the drift of ice floes originating from outside the OWF as in Figure 1.1c and (2) the drift of an ice floe that is initially frozen-in around the turbines, displayed in Figure 1.1d. The first scenario provides insight into the influence of OWFs on ice drift speed, while the second scenario examines the wind forcing required to (re-)initiate ice drift in frozen-in conditions. This leads to the main research question of this thesis:

How does the presence of an offshore wind farm affect the ice drift speed for both an ice floe field that originates from outside the offshore wind farm and a grown-in condition in the Southern Baltic Sea?

The main research question is answered by splitting it into two subquestions:

- How does the presence of an offshore wind farm affect the drift speed of ice floes when they originate from outside of the offshore wind farm?
- What critical combination of wind speed and ice thickness is required to (re-)initiate the movement of a stationary ice sheet in a frozen-in offshore wind farm, leading to an intimate contact condition?

By addressing these questions, this study aims to improve the understanding of macroscale ice drift in offshore wind farms and contribute to the development of more resilient wind energy infrastructure in cold regions.

This thesis only focuses on level ice floes, which are defined as any relatively flat piece of ice 20 m or more across and unaffected by deformation (Leppäranta, 2011). Thus, rafted-, bended- or ridged ice - sea ice that is forced up or down due to compressive stress - is not considered. This thesis uses the existing software SIBIS (Simulation of Interaction between Broken Ice and Structures). SIBIS is a discrete element method that simulates the interaction of offshore structures with sea ice and solves multiple ice failure processes relevant to macro- and mesoscale modelling, for example ice-structure- and ice-ice-crushing, bending, splitting and buckling (Metrikin, 2014; Serre, 2019). Only ice drift in 2D - in the horizontal plane of motion - is considered in this thesis, which means that bending, rafting and buckling of ice are not modelled. The primary ice failure processes in this study are crushing and splitting. It should be noted that ice-ice interaction is only resolved via crushing (no splits can occur due to interaction between ice floes) and that fracture can only occur along straight lines. Furthermore, velocity dependent crushing is not implemented in SIBIS. External forces due to wind and current are implemented using a constant mesh over the domain. SIBIS does not incorporate hydrodynamic coupling, consequently the ice motion is not updated using simulated current velocities. Furthermore, wave fields are not included as SIBIS does not consider first- and second-order hydrodynamic effects. The dynamics of sea ice is strongly coupled to thermodynamics, as freezing strengthens the ice and melting weakens it. Ice growth and melt are influenced by the ice motion via transport and differential motion of the ice (Leppäranta, 2011). SIBIS does not model thermodynamics. However, the timescale of the simulations that were performed in this study only span a few hours. This thesis therefore assumes that thermodynamics can be neglected, thus ice growth- and melt are not simulated. SIBIS is currently verified using analytical benchmark tests, model- and full-scale data. Furthermore, it follows ISO 19906 guidelines that provide requirements for the design and construction of offshore structures in Arctic and cold regions.

1.3. Reading Guide

In this section, a short description of each chapter is given.

Chapter 2 **Ratio of Ice Drift Speed to Wind Speed**

This chapter provides the reader with background information on the dynamics of sea ice and the characteristics of ice floe fields. It describes how a distinction can be made based on the sea ice concentration of an ice floe field and what implications this has for ice drift. The dynamics of an object drifting in water are presented along with assumptions that can be made for the scale of an offshore wind farm. It is then explained what the expected ice drift- to surface wind speed ratio is for the ice floe sizes that are considered in this thesis.

Chapter 3 **Boundary Conditions**

This chapter presents the parameters that must be selected to perform simulations. First, the environmental conditions in the Southern Baltic Sea - such as wind speed and water current speed - are considered. Then, it is explained how the drag coefficients are implemented in SIBIS, what ice parameters are used and what mesh settings are implemented. Next, first verification simulations are performed to verify if the free drift speed of an ice floe is in line with the theory from Chapter 2. It is then formulated how crushing and splitting are performed in SIBIS. Lastly, this chapter presents an overview of all the boundary conditions that will be used throughout the simulations.

Chapter 4 **Capturing The Sea Ice Characteristics**

This chapter explores the current methods that are available for obtaining an ice floe size distribution at the spatial scale of an offshore wind farm. Next, it is explained why image processing is selected in this thesis and how it can be applied to satellite images from the Baltic Sea. Lastly, the image processing results are evaluated by performing statistical tests, and the acquired floe size distribution is compared to literature for other icing seas.

Chapter 5 **Synthetic Ice Floe Field Generation**

This chapter describes how the floe size distribution for the Southern Baltic Sea can be used to create a synthetic floe field. This requires implementation of the parameters of the floe size distribution into a floe field generator that creates an ice floe field by randomizing floe shapes, orientation and placement. The synthetic fields that are created for the Baltic Sea are then verified. Finally, the introduction of unforeseen errors due to the floe field generator and image processing is examined.

Chapter 6 **Simulation**

This chapter describes the theory behind the two simulation scenarios that are considered in this thesis. First, it explains how the case of ice floes initially positioned outside the offshore wind farm is implemented. Then it describes the theory behind a frozen-in offshore wind farm. For both scenarios, this chapter then describes what ice floe fields and offshore wind farm layouts are selected for answering the two research questions that were formulated in the introduction. It then explains what variables are considered to conduct a sensitivity analysis that will be treated in the discussion. Lastly, it presents the theoretical expectations and insights from trial simulations.

Chapter 7 **Results**

First, this chapter explores the simulation results for the scenario in which the ice field

is initially positioned outside the OWF. The analysis starts by observation of the ice floe velocities at both a single- and multiple turbines. Then, the interaction between ice floes is studied further by considering the histograms of the ice floe velocities with- and without the presence of turbines. Then, the spatial distribution of the ice drift speed across the floe field is explored by considering the effect of changing sea ice concentration and maximum floe size. Secondly, the grown in scenario is treated. Critical combinations of ice thickness and surface wind speed that lead to crushing are presented. Next, the effect of increasing the number of turbines and ice area is explored and the results are extrapolated to the offshore wind farm modelled after the existing Baltic Eagle wind farm. Finally, the influence of the distance between the turbines and the surrounding ice is shown.

The concluding chapters analyse the findings of this thesis, respond to the research questions, discuss the results and offer recommendations for future research.

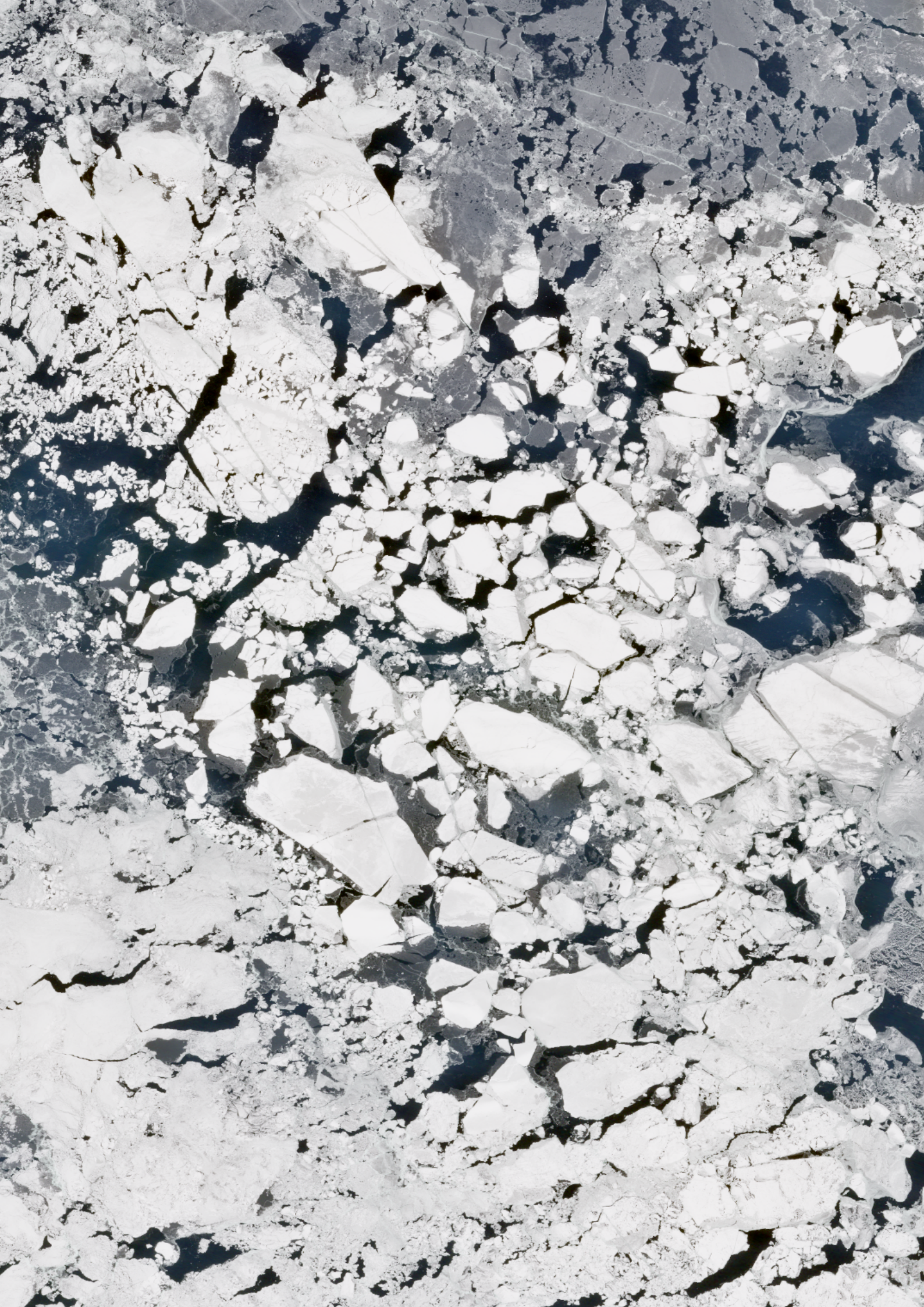

2

Ratio of Ice Drift Speed to Wind Speed

This chapter delves into the theory behind sea ice dynamics. Ice is driven by the wind and ocean currents and responds to forcing by adjustments in the state field (the material properties of ice), the inertia and the internal friction of ice (Leppäranta, 2011). First, it describes the basic regimes of sea ice drift, namely free drift and drift in the presence of internal friction of ice. The next section describes the motion of objects that drift in water by considering two limit cases. It is then explained what factors determine the occurrence of these limit cases.

2.1. Ice Drift Regimes

The ratio between the ice drift speed and wind speed can be described by the Nansen number, named after the Norwegian explorer and scientist Fridtjof Nansen. During his Arctic expeditions, he observed that ice drifts at a certain angle to the wind direction and at a fraction of the surface wind speed. The Nansen number is defined as in (2.1).

$$Na = \sqrt{\rho_a/\rho_w}\sqrt{C_a/C_w} \tag{2.1}$$

This number reflects how efficiently the wind transfers its momentum to the sea ice and quantifies the relative importance of atmospheric versus oceanic forcing on the motion of sea ice. The Nansen number plays an important role in modelling the movement of sea ice, particularly in free-drift conditions. An important factor that influences the Nansen number is the sea ice concentration (SIC). A sea ice concentration of 80-85% generally marks the boundary between free drift and drift in the presence of internal friction. When the ice concentration exceeds this boundary, the internal friction between the ice floes leads to more complex behaviour, changing the drift speed. An example of a high-concentration Arctic floe field can be found in Figure 2.1a. The high concentration allows for sufficient collisions between the ice floes so that internal ice stresses can be transmitted over a distance greater than the floe width (Heorton et al., 2019). The presence of internal friction has a few consequences for the sea ice motion (Leppäranta, 2011):

- The overall drift speed is lowered since part of the mechanical energy is transferred into ice deformation.
- The ice is motionless if the external forcing does not exceed the yield limit of the ice.
- The internal stresses in the ice field allow the transfer of mechanical energy over long distances.

Below 80%, the ice drifts freely and the drift speed is primarily determined by the wind- and current speed, as collisions between floes occur less frequently due to the distance in between the ice floes. An example of such a floe field is found in Figure 2.1b. Nansen found that in free drift, ice drifts at an angle of 20 - 40 degrees to the right of the surface wind direction in the Northern Hemisphere due to the Coriolis effect. For freely drifting ice floes in the Baltic Sea, a Nansen number of 0.020-0.025 has long been observed, meaning that ice floes typically move at a speed of 2% - 2.5% of the surface wind speed (Leppäranta, 2011). This relationship generally holds for all floating objects, such as Arctic icebergs, oil slicks, mangrove drifters and lost cargo containers. Despite significant differences in material properties, object shapes and sizes, all these floating objects drift at a ratio of 2% - 4%. This equivalent sensitivity to the wind forcing can be explained in an intuitive way by using the leeway modelling approach (Wagner et al., 2022) as outlined in the following section.

(a) High concentration floe field in the Arctic (ten Broecke, 2016).

(b) Example of a floe field in the Arctic characterized by a low sea ice concentration (Alfred Wegener Institute, 2019).

Figure 2.1: Example of Arctic ice floe fields with different sea ice concentrations.

2.2. The Dynamics Of Sea Ice Drift

The motion of sea ice results from the drag forces that are exerted by the wind- and ocean current. The atmospheric and oceanic drag coefficients are dependent on the ice surface roughness, floe size and ice concentration. Because of changing ice morphology, the drag coefficients may vary in time (Lu et al., 2011). The wind- and ocean drag forces can be split up into two terms: the form drag and skin friction. The form drag is related to the pressure differential between the front and rear of an object, caused by the flow separation from an object. Form drag describes the normal force on the face of an ice floe while it moves through a fluid and is determined by its size and shape. Skin friction is related to the shear stress that occurs along the surface of the object and is induced by surface velocity fluctuations and eddy viscosity (Lu et al., 2011). While skin- and form drag follow equivalent drag equations and both scale with the relative velocity between object and fluid, skin drag coefficients are generally smaller (order 10^{-3}) than form drag coefficients (order 1) (Wagner et al., 2022).

The water-induced drag force can be written as in (2.2)

$$\mathbf{F}_w = \frac{1}{2}\left(C_w^F A_w^V + C_w^S A_w^H\right)\rho_w |\Delta\mathbf{v}_w|\Delta\mathbf{v}_w, \tag{2.2}$$

Where $\Delta\mathbf{v}_w = \mathbf{v}_w - \mathbf{v}$ describes the velocity $\mathbf{v}$ of the object relative that of the water $\mathbf{v}_w$, and C_w^F and C_w^S are the form drag and skin drag coefficients for water, A_w^V and A_w^H are the cross-sectional vertical and tangential horizontal surface areas of the object facing the flow of water. ρ_w denotes the density of water. The wind-induced drag force is described by (2.3).

$$\mathbf{F}_a = \frac{1}{2}\left(C_a^F A_a^V + C_a^S A_a^H\right)\rho_a |\Delta\mathbf{v}_a|\Delta\mathbf{v}_a, \tag{2.3}$$

Where the definitions for all terms are similar as to those for water, except for that the subscript have been changed from w (water) to a (air). The momentum equation (2.4) for a drifting object can be written as:

$$m\frac{d\mathbf{v}}{dt} = \mathbf{F}_w + \mathbf{F}_a + \mathbf{F}_c + \mathcal{F}, \tag{2.4}$$

Equation 2.4 displays the Maxey-Riley equation in a simplified form. The Maxey-Riley equation considers the force balance for spherical particles that are immersed in unsteady and non-uniform flow (Wagner et al., 2022). The traditional Maxey-Riley equation considers additional terms such as the added mass of an immersed particle, which are captured by the placeholder $\mathcal{F}$, representing any other forces acting on the object. Equation 2.4 models the motion of an inertial particle in a flow, hence it is a Lagrangian description. In this equation, m is the mass of the object, $\mathbf{F}_c = mf\hat{\mathbf{k}} \times \mathbf{v}$ is the Coriolis force (with f the Coriolis parameter and $\hat{\mathbf{k}}$ the vertical unit vector).

The case is now considered in which the Coriolis force, inertial effects and other forces are relatively small compared to the water- and wind-drag forces. To ensure this assumption is acceptable, the ratio of water drag is compared to the Coriolis force (2.5):

$$\frac{|\mathbf{F}_w|}{|\mathbf{F}_c|} \sim \frac{\rho_w |\Delta \mathbf{v}_w|}{\rho\, l f}, \tag{2.5}$$

Here ρ is the density of an object and l is its length. Generally, $\rho_w/\rho \sim 1$ and $|\Delta \mathbf{v}_w| \leq 0.1\ m/s$. Using a Baltic Sea latitude value for the Coriolis parameter $f \sim 1.42 \times 10^{-4}\ s^{-1}$ it is found that the water drag force dominates the Coriolis force when $l \leq 704$ m. Analysing the ratio of air drag to Coriolis (2.6):

$$\frac{|\mathbf{F}_a|}{|\mathbf{F}_c|} \sim \frac{\rho_a |\Delta \mathbf{v}_a|^2}{\rho\, l f |\mathbf{v}|^2}. \tag{2.6}$$

In this example, $\rho_a/\rho \sim 10^{-3}$ and $|\Delta \mathbf{v}_a| \sim 10\ m/s$, meaning wind drag is dominant when $l \leq 10\ km$. Considering the results that are presented in Chapter 4, the range of floe diameters that was found is 564 - 9700 m. Thus, the water drag force does not dominate the Coriolis force for all floe sizes. However, Lappäranta (2011) states that when ice thickness is small, the Coriolis term is small as well. Therefore, it is assumed the Coriolis force can be neglected. The steady drift of small floating objects can now be described as (2.7):

$$m\frac{d\mathbf{v}}{dt} = \mathbf{F}_w + \mathbf{F}_a = 0. \tag{2.7}$$

The objects can be schematized as rectangular shapes, such that:

$$A_a^V = wb, \quad A_w^V = wd, \quad \text{and} \quad A_a^H = A_w^H = wl,$$

In which w is the width of the object, b its freeboard (height above the waterline), d is the draft (depth below the waterline) and l is the along-flow length of the object. The across-flow width w is assumed to be the same for all surfaces and thus cancels out in the equations below. Therefore, a two-dimensional system is considered, having vertical and along-flow dimensions. Expressing the freeboard and draft as a function of its height h, its density ρ and the density of water ρ_w results in:

$$b = h(1 - \rho/\rho_w) \quad \text{and} \quad d = h\rho/\rho_w.$$

As turning angles due to the Coriolis force are not considered, drift speed can be considered in a one-dimensional system. It can be stated that Δv_a = $v_a - v \approx v_a$, as the surface wind velocity is typically much larger than the velocity of the object. Now substituting the expressions for the drag forces into equation 2.7 for steady drift and solving for v, the following expression is obtained (2.8):

$$v = v_w + \gamma v_a, \tag{2.8}$$

Where γ is called the leeway factor, or wind factor that describes the sensitivity of an object to wind-forcing. This wind factor is defined as equation (2.9):

$$\gamma = \sqrt{\frac{\rho_a}{\rho_w}} \sqrt{\frac{bC_a^F + lC_a^S}{dC_w^F + lC_w^S}} \tag{2.9}$$

In this expression, the numerator under the second square root describes the contribution of form- and skin air drag. The denominator reflects the form- and skin water drag. The length-to-height ratio l/h is called the aspect ratio. A limit state for dominant skin drag can now be defined, which is called the 'membrane limit'. In this case, $l \gg h$ and the wind factor simplifies to (2.10):

$$\gamma \approx \sqrt{\frac{\rho_a}{\rho_w}} \sqrt{\frac{C_a^S}{C_w^S}} \tag{2.10}$$

If the skin drag coefficients are replaced by the effective drag coefficients C_a and C_w that include both skin drag and form drag, the expression for the wind factor is equal to the Nansen number in equation (2.1) (Leppäranta, 2011). The air and water skin drag coefficients are approximately equal for

many materials since the roughness of the upper and lower surfaces are to some degree correlated (Leppäranta, 2011), leading to a wind factor of $\gamma \approx (\rho_a/\rho_w)^{1/2} \approx 3\%$ (assuming $\rho_w \approx 10^3\ kg\ m^{-3}$ and $\rho_a \approx 1\ kg\ m^{-3}$). This means that thin objects drift at an approximate speed of 3% of the surface wind speed relative to the water, independent of an object's density and aspect ratio. This membrane limit corresponds to the horizontal purple line in Figure 2.2. However, the geometry of many floating objects does not correspond to the membrane limit. Nonetheless, it can be shown that the wind factor of 3% is applicable to a wide range of objects.

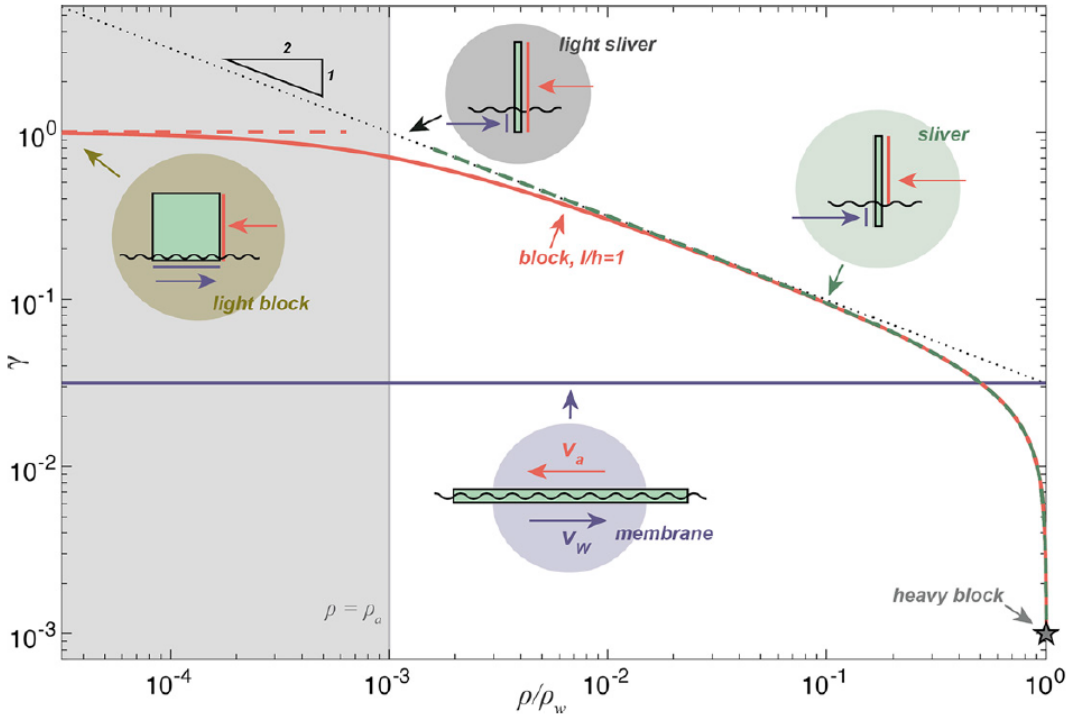

Figure 2.2: Dependency of the wind factor γ on the ratio ρ/ρ_w for different aspect ratios. In between the membrane limit case and the sliver limit case, the full solution for the wind factor (red curve) is displayed (Wagner et al., 2022).

Form drag coefficients are typically in the order of 1, while skin drag coefficients are in the order of 10^{-3}, implying that skin drag is only dominant in the exceptional case when $l > 10^3 h$. For most objects, $l \ll 10^3 h$ and the force balance is primarily between the air- and water form drag. Sea ice is an intermediate case, since very thin, young and uniformly grown ice is mainly subject to skin drag, while broken-up and deformed ice floes (such as pressure ridges) are most influenced by form drag. When $l \to 0$ the wind factor can be written as (2.11):

$$\gamma = \sqrt{\frac{\rho_a}{\rho_w}} \sqrt{\frac{bC_a^F}{dC_w^F}} = \sqrt{\frac{\rho_a}{\rho_w}} \sqrt{\frac{C_a^F}{C_w^F}} \sqrt{\frac{1-\rho/\rho_w}{\rho/\rho_w}}. \tag{2.11}$$

This theoretical object is referred to as a theoretical 'sliver' with finite height and zero along-flow length. In Figure 2.2 this sliver limit is displayed by the green dashed line. When $l/h \leq 1$ and $\rho/\rho_w > 10^{-2}$ the sliver limit is almost equal to the full solution (shown in the red curve), which corresponds to a square block with l/h = 1. For aspect ratios smaller than one, the full solution approximates the green dashed line even better. For l/h = 10 and $\rho/\rho_w > 10^{-1}$ the sliver is still a good approximation for the full solution (not shown in Figure 2.2). This range covers most floating solid objects in a geophysical setting. The analysis of the two limits shows that as aspect ratio increases, the density of an object becomes of less importance for determining the wind factor. In the membrane limit, the wind factor does not depend on ρ/ρ_w, corresponding to the upper bound of aspect ratio in Figure 2.3. The force balance is then dominated by the surface skin drag at the air- and water-interface. These surfaces do not depend on the density, as the density only determines what fraction of the object is submerged in water. Likewise,

the force balance for objects with small aspect ratios is highly dependent on the density, as form drag is the primary driving force. This density-dependent behaviour is seen in the left part of Figure 2.3. Measurements of sea ice densities show typical values of 740 to 917 kg m^{-3}. Now using the wind factor equation for $l \to 0$ and assuming the wind and air form drag coefficients are approximately equal, an upper bound for the wind factor of $\gamma = 2.5\%$ is found. For pure ice (when $l/h = 1$) a lower bound of $\gamma = 1.3\%$ holds. As the aspect ratio increases, these bounds converge towards the membrane limit of $\gamma = (\rho_a/\rho_w)^{1/2} \approx 3\%$ (Wagner et al., 2022).

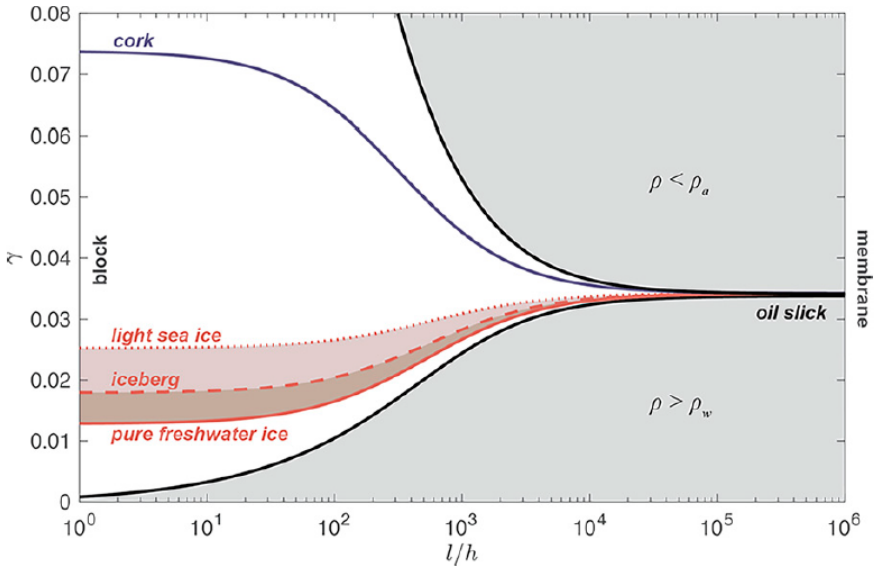

Figure 2.3: The wind factor γ as function of the aspect ratio l/h for multiple object densities. On the left side, the curve is bounded by a block shape having aspect ratio l/h=1. On the right side, the membrane limit is approached as $l \gg h$ (Wagner et al., 2022).

The ratio between ice drift speed and wind speed can also be analysed for various ice concentrations. Based upon observations, Figure 2.4 shows that the ice drift speed (scaled with the theoretical free drift speed) is relatively constant below a sea ice concentration of 80%. As this boundary is exceeded, the mean wind factor decreases while the variance of the wind factor highly increases. In this case, the wind factor is less predictable by free drift theory, as it becomes highly sensitive to small compactness changes in the ice (a substitute term for ice concentration). This sudden change in sensitivity is caused by the internal friction of the ice (Leppäranta, 2011). Therefore, the correlation between surface wind and sea ice drift tends to be lower at high ice concentrations (Nakayama et al., 2011).

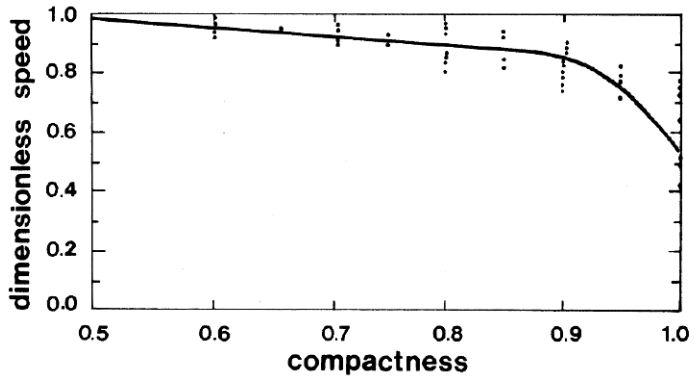

Figure 2.4: Observations of ice drift speed scaled with the theoretical free drift speed as a function of ice concentration (or compactness) (Leppäranta, 2011).

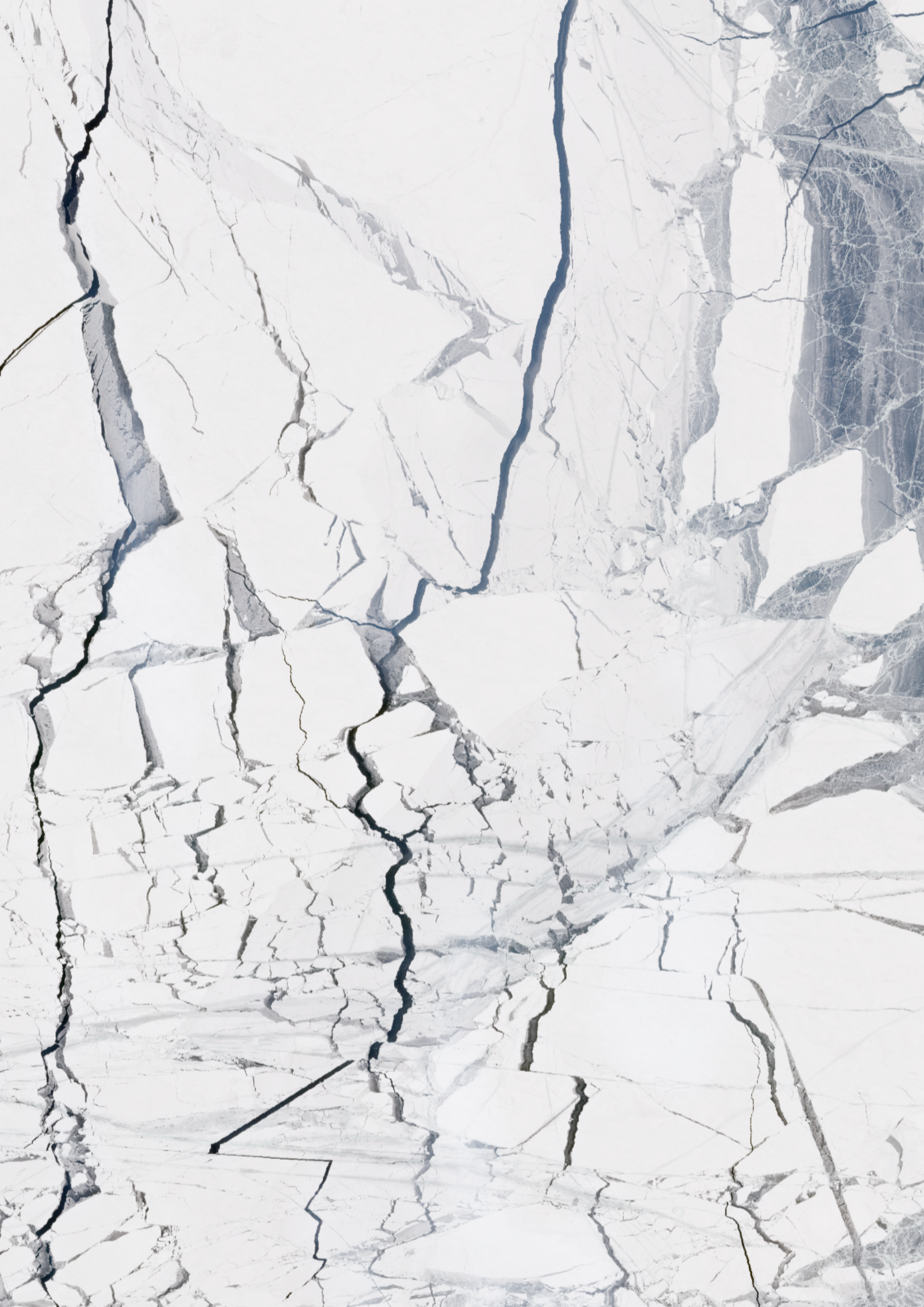

3
Boundary Conditions

The parameters required for simulations are now selected. A number of these parameters, such as the form- and skin-drag coefficients were described in Chapter 2. Other parameters concern environmental conditions such as wind speed and water currents. These parameters will be treated in this chapter. It is then explained what mesh settings were used for the simulations in SIBIS. Next, the chosen input parameters are validated to ensure consistency with the theory presented in Chapter 2. Finally, an overview of the boundary conditions that are used for the simulations is presented.

3.1. Environmental conditions

Multiple sources report different values for the surface wind speed in the Baltic Sea. In the Baltic Sea sub-basins, wind speeds of 5-10 m/s occur most often (measured at 10 m height) (Cieślikiewicz et al., 2024). Zhang et al. (2011) conclude that statistical results indicate the 50-year average wind speed in the Southern Baltic Sea is 7.5 m/s. An offshore energy potential investigation from the Energy Ministry of Lithuania shows that the average annual wind speed at 100-200 m height is 9.0-9.6 m/s with a peak of 12.5 m/s during the winter. In February, the month in which the Sentinel-2 L2A images used for image processing were captured, the wind speed is approximately 11 m/s (Lietuvos Respublikos Energetikos Ministerija, 2023). Based on all these sources, the constant wind velocity in the Southern Baltic Sea is estimated to be $u_{wind,10m}$ = 10 m/s at 10 m height. Winds having a SSW-direction were most frequently observed for the Baltic Sea during the period 1958-2001, which is therefore the constant boundary condition for surface wind direction (Cieślikiewicz et al., 2024).

Currents in the Baltic Sea depend primarily on weather conditions and may thus be highly varying. Momentary flow velocities in the surface layer are typically 0.05 - 0.1 m/s. Permanent currents that can be found in oceans do not apply to the Baltic Sea. Medvedev et al. (2013) collected long-term hourly tidal data from 35 tide gauge stations across the Baltic Sea to analyse tidal variations. A maximum tidal oscillation of 0.17 - 0.19 m was found in the Gulf of Finland. In the upper water layer, tidal amplitudes of 0.05 - 0.06 m/s have been observed at the southern coast of the Gulf of Finland (Lilover, 2012). Therefore, it is assumed tidal currents can be neglected. During heavy storms, surface currents in the Baltic Sea can reach up to 0.5 m/s. These currents are also dependent on topography, as currents of over 1 m/s have been measured in some narrow straits such as the Bothnian Sea. Generally, the velocity of sea currents is about 1% of surface wind speed (Finnish Meteorological Institute, 2022), which would result in a current of u_{water} = 0.1 m/s. Current direction in the Baltic Sea thus depends primarily on weather. Choosing a wind- and current that are in the same direction will amplify the ice drift speed, and most likely lead to a higher ratio of ice drift speed to wind speed (Sinsabvarodom et al., 2022).

Strictly speaking, the wind factor is defined as the wind-driven component of sea ice drift relative to the surface wind speed. However, if the wind factor is only calculated from the time series of wind and sea ice drift, the temporal variation of water currents underneath the ice is neglected. This often happens due to a shortage of current observations underneath the ice that is presently available. In this case, the wind factor thus contains the effect of temporally varying water current, possibly increasing or decreasing the wind factor (Nakayama, 2011). According to Leppäranta (2011), the ice drift may be calculated from Equation 3.1 under the assumption that the Coriolis term is small when the ice thickness is small:

$$u = Na \exp(-i\theta_0) U_a + U_{\mathrm{wg}} \tag{3.1}$$

In this equation, Na is the Nansen number that equals the wind factor, $\theta_0 = \theta_w - \theta_a$ is the deviation

angle from the wind-driven ice drift direction to the wind direction, u is the ice drift velocity, U_a is the wind velocity and U_{wg} is the geostrophic water velocity. The ice drift speed is thus expressed as the summation of a wind- and water-driven component. Since the near-surface water current in the Baltic Sea is found to be highly varying in both magnitude and direction, it is chosen to only focus on the effect of the wind speed and set the current speed to zero.

3.2. Drag Coefficients

To determine the drag coefficients, it is important to first know the type of ice that is present in the Southern Baltic Sea. Since Sentinel-2 L2A satellite images show that Southern Baltic Sea ice melts during spring and summer every year, first year ice conditions are assumed. This will lead to lower drag coefficients compared to multi-year ice, as it is generally smoother (Cole et al., 2017). In SIBIS, first year ice will also be assumed for the surface material properties of the ice floes, such as the friction coefficients for contact resolution at the structure. First year ice often has a relatively smooth bottom that results in an ice/water skin friction coefficient of C_w^S = 2×10^{-3} (Lu et al., 2011). Based on a series of measurements in the Fram Strait at 1.7 m above large- and relatively flat ice floes (Hanssen-Bauer et al., 1987), a value of C_a^S = 2×10^{-3} is chosen for the ice-wind skin friction coefficient.

Observational studies provide form drag coefficients for sea ice ranging from 0.5 to 1×10^{-3} (Alek et al., 2017). In SIBIS, the form drag coefficients are adjusted to match analytical solutions from classical quadratic equations that describe current- and wind drag. Therefore, C_w^F and C_a^F should both be set to 0.5. Another reason for this is that SIBIS does not include Coriolis force and there are only a few damping laws. Damping forces on ice floes only account for heave-, roll- and pitch motions. No damping forces are applied to sway, surge and yaw. Artificially increasing the form drag coefficients is also done to model the effects of compression of ice (Rabatel, 2025). The ocean drag- and atmospheric drag-coefficients, Cd_{ocean} and Cd_{atm} acting on the turbines are set to zero as they are modelled as fixed (immobile) and rigid structures. Drag coefficients remain constant throughout the simulation in SIBIS, they are not time-dependent.

3.3. Ice Parameters

The physical properties that can be used to describe ice operate at distinct scales. Properties such as ice density, ice strength coefficient and fracture toughness determine the mechanical response of ice under stress on a relatively small scale. These properties determine the formation of cracks, splitting and crushing events. The parameters that are selected to define the ice at such a small scale are listed in Table 3.1.

Parameter	Symbol	Value	Unit
Ice Density	ρ_{ice}	920	kg m^{-3}
Ice Strength Coefficient	C_R	0.725	MPa
Fracture Toughness	K	250	kPa $\cdot\sqrt{\text{m}}$
Youngs Modulus	E	1.22	GPa
Poisson Ratio	ν	0.3	-
Shear Strength	τ	0.3	MPa

Table 3.1: Ice parameters that are chosen for the simulations in SIBIS. The ice strength coefficient is retrieved from Gravesen et al. (2009). This value is low compared to what is generally used, as it reflects an average annual strength value rather than a maximum. First-year sea ice density, shear strength, Youngs Modulus, poisson ratio and fracture toughness are provided by Timco et al. (2009).

Large scale characteristics of ice are due to the collective behaviour of an assortment of individual ice floes. These characteristics determine the response of the ice field over several tens of meters to a few kilometers. The ice field characteristics - for example the sea ice concentration - define how the ice dynamics are affected by processes such as wind forcing. The large-scale characteristics that are relevant for this thesis will be addressed in Chapter 4.

3.4. Mesh Settings

Mesh settings in SIBIS can be adjusted according to the geometry of the structure and the ice floe sizes. It was found that the two scenarios that are explored in this thesis require different mesh settings. These can be found in Table 3.2 at the end of this chapter. This table presents a summary of all the parameters that are related to the mesh settings.

3.5. Benchmarking

3.5.1. Free Drift Speed In SIBIS

The free drift speed of a single ice floe can be analysed in SIBIS for the assumptions that were previously described. The free drift speed is first verified for an ice floe that corresponds to the membrane limit case, having an aspect ratio of $l/h > 10^3$. This ice floe is defined in SIBIS as a rectangular floe with a diameter of 1000 m and a thickness of 0.4 m. Applying equation (2.9) and using the selected skin drag coefficients, the theoretical wind factor γ is equal to 3%. It is thus expected that this type of ice floe would freely drift at a speed close to 0.30 m/s. In Figure 3.1a the result from the test in SIBIS is shown. The ice floe gradually reacts to the wind-forcing and eventually stabilizes at a free drift speed of 0.30 m/s. The second case that will be tested is one in which the ice floe has a diameter of 10 m and a thickness of 0.40 m. The aspect ratio is then equal to 25, close to the case of a block ($l/h = 1$). Applying equation (2.9) and using the selected skin- and form drag coefficients, it is found the wind factor equals 1.3% and therefore the steady state free drift floe speed should equal 0.13 m/s. From Figure 3.1b it is concluded that the floe speed in SIBIS stabilizes at 0.13 m/s. As the results from SIBIS are close to the drift speed that was expected based on the theory in Chapter 2, it is assumed that the selected skin- and form-drag coefficients yield physically correct results.

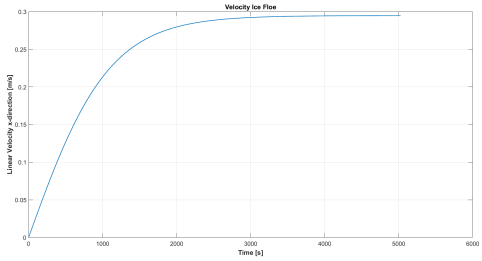

(a) Steady-state free drift velocity of a 1000 x 1000 m ice floe in SIBIS. For a wind speed of 10 m/s, the floe speed stabilizes at 0.30 m/s.

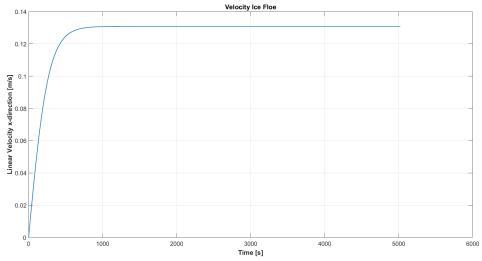

(b) Steady-state free drift velocity of a 10 x 10 m ice floe in SIBIS. For a wind speed of 10 m/s, the floe speed stabilizes at 0.13 m/s.

Figure 3.1: Comparison of the free drift speed of an ice floe for two limit cases for verification of the skin- and form drag coefficients.

3.5.2. Crushing

In contrast to reality, crushing in SIBIS is independent of the relative ice-structure velocity. The crushing force $\mathcal{L}_{cr}$ is described according to ISO 19906 (Paquette et al., 2017) and is described by equation (3.2):

$$\mathcal{L}_{cr} = C_R \left(\left(\frac{h}{h_1} \right)^n \left(\frac{w}{h} \right)^m + e^{-\frac{w}{3h}} \sqrt{1 + 5 \left(\frac{w}{h} \right)^{-1}} \right) \cdot h \cdot w \tag{3.2}$$

where:

- w = projected width of structure [m]
- h_1 = reference thickness of 1 m [m]
- h = ice thickness [m]
- C_R = ice strength coefficient [MPa]
- $n = \min\left(-0.5 + \frac{h}{5}, -0.30\right)$
- $m = -0.16$

The ice breaking in SIBIS is solved based upon multiple ice breaking settings that can either be set to true or false. In order to match the analytical solution from ISO 19906, it was found that the input parameter ”CrushPenetratedFloes” should be set to false. If set to true, the ice floes penetrating the structure with an absolute penetration larger than a specified threshold will be crushed independently of the computed contact force. This can improve simulation stability in detriment of accuracy when large penetrations are observed. Furthermore, ”AllowsBreakingForSmallFloes” is set to true as it has no significant effect on simulation time. ”ActiveIceIceCrushing” is set to true to accurately resolve the ice-ice interaction. If set to false, the ice-ice interaction would be treated as rigid. For full-width contact of the turbine (7.5 m) and an ice thickness of 0.4 m, these settings lead to a maximum force of 1.99 MN for a floe drifting towards a turbine in SIBIS. Equation (3.2) gives a value of 2 MN. As the differences are minor relatively, it is assumed that the selected ice breaking settings do not introduce major errors in the computation of the crushing force.

3.5.3. Splitting

The splitting force in SIBIS is in accordance with API-RP-2N (Bhat, 1988) and follows equation (3.3):

$$\mathcal{L}_S = 3.3hK\sqrt{L_i} \tag{3.3}$$

where:

- K = ice fracture toughness [N/m]
- L_i = minimal distance to the open water from the splitting origin [m]

This equation applies for square floes. The ice-splitting process is decomposed in multiple steps in SIBIS:

1. The first step consists of creating a selection of points on the ice-structure interface that are within an angle of 160 degrees of the relative ice-structure velocity vector (denoted in Figure 3.2a as $CPSEA$). Additionaly, an ice floe can only be split into two pieces if for each piece, the ratio between the length and width of the piece is smaller than 5. This is denoted by the parameter $MaxFloeSidesRatio$. Furthermore, the floe area must be greater than 20 m^2 to fall into the splitting failure mode, defined by the parameter $MinimalAreaForSplitting$.
2. For each point, the distance to the open water L_i (corresponding to $\vec{d_s}$ in Figure 3.2b) and its corresponding angle is computed. If this angle is within the cone of 160 degrees, the point is considered eligible for splitting. The maximum angle that is considered for the selection of eligible splitting points is a user setting. The values that are stated in Table 3.2 are default. From the eligible splitting points, the point with the minimal distance to the open water is defined as the splitting origin. The shortest splitting path through the ice floe will only be searched within a cone of 40 degrees centred at the structure-ice relative velocity vector (denoted in Figure 3.2b by $ESOA$). Splitting will initiate from the breaking point with the maximal contact force for the API-RP-2N model.

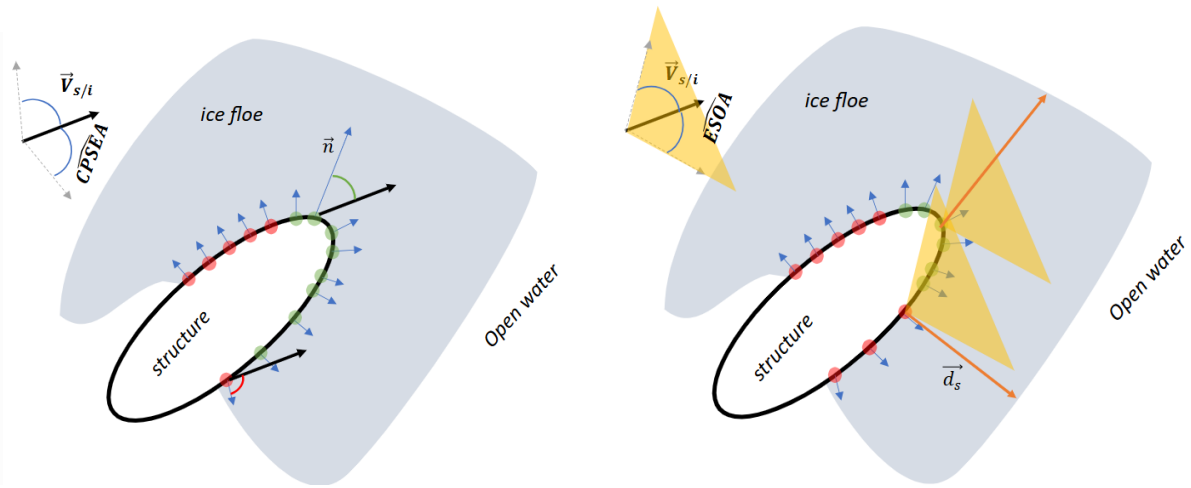

(a) The first splitting step.

(b) The second splitting step.

Figure 3.2: Ice splitting steps in SIBIS

With the API-RP-2N model, the splitting is only triggered if the magnitude of the global contact force applied to the floe is greater than $\mathcal{L}_S$, in addition to the split length smaller than the maximum allowed split length "SplitLengthMax".

(Bhat, 1988) and (Lu et al., 2014) found that the force required for splitting only increases up to the point where the crack length is a fraction of the floe diameter. Beyond this point, the crack propagation becomes unstable and the force required for splitting reduces significantly. The location of this point is highly affected by the parameter $\beta = \frac{F_Y}{F_X}$, in which F_Y is the crack opening force in the lateral direction, while F_X is the ice force in the direction of the relative ice-structure velocity, as seen in Figure 3.3b. This decomposition depends primarily on the contact geometry and the ice-structure interaction process. (Lu et al., 2014) and (Bhat, 1988) assume one fixed load ratio to generalize this problem and avoid solving the stress distribution within the contact zone for specific structural geometries. A possible way of estimating β is to require that β corresponds to the minimal value for which splitting will still occur. If β would be lower, it would result in overlap of the crack surfaces due to compression in the contact zone, which is unphysical (Bhat, 1988). As the splitting load increases with decreasing β, this approach will yield a conservative estimate for the splitting load. This results in an approximate value of $\beta_{min} = 0.3$ that is in correspondence with equation (3.3). From Figure 3.3a it can be seen that β_{min} results in a significant peak split load compared to higher values for β. For all values of β, it can be assumed that if the peak split load is reached, the split fails catastrophically and complete splitting failure occurs (Bhat, 1988;Lu et al., 2014). Figure 3.3a shows that this point is reached for β_{min} when the crack length is less than 10 percent of the diameter of the ice floe. Other parameters may influence the splitting load as well. For example, a higher lateral confinement of an ice floe leads to a higher force required for splitting (Lu et al., 2014). However, this effect is not accounted for. Utilizing this high peak splitting load without specifying a maximum splitting length is considered the most realistic approach within SIBIS, as crack propagation is not modelled.

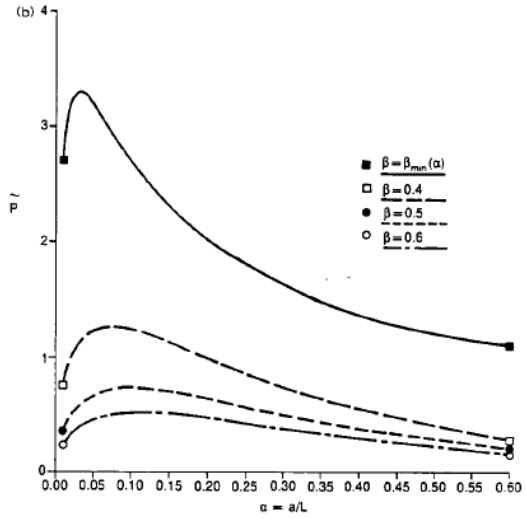

(a) Ice splitting load for varying values of β. β_{min} leads to a significantly higher peak splitting load as compared to higher values for β (Bhat, 1988).

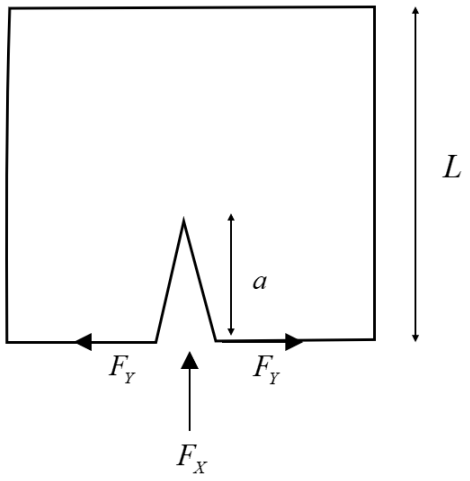

(b) Geometry of the ice splitting process. The crack length is defined as a and the floe diameter as L. F_Y is the crack opening force and F_X is the ice force in the direction of the relative ice-structure velocity.

Figure 3.3: Ice splitting

3.6. SIBIS Settings

Table 3.2 presents the final list of SIBIS input and settings that will be used during the simulations.

Atmospheric Conditions	
$u_{wind,10m}$	10 m/s
Wind direction	SSW
C_a^F	0.5
C_a^S	$2 \times 10^{-}3$
Oceanic Conditions	
u_{water}	0 m/s
C_w^F	0.5
C_w^S	2×10^{-3}
Ice Parameters	
$Hice$	0.4 m
C_R	0.725 MPa
ρ_{ice}	920 kg m^{-3}
K	250 kPa $\cdot\sqrt{\text{m}}$
E	1.22 GPa
ν	0.3
τ	0.3 MPa
Mesh Settings - Outside Drift	
H_{min}	3 m
H_{max}	150 m
H_{grad}	2.4
H_{limmax}	30 m
$H_{sizecontacticeice}$	5 m
$H_{sizecontactstructureice}$	3 m
ϵ_{Geom} (Boundary smoothing)	0.05
Max distance smoothing (Boundary smoothing)	0.05
ϵ_{Geom} (Contact structure-ice)	0.01
Max distance smoothing (Contact structure-ice	0.01
Mesh Settings - Grown-in	
H_{min}	5 m
H_{max}	500 m
H_{grad}	2.4
H_{limmax}	150 m
$H_{sizecontacticeice}$	10 m
$H_{sizecontactstructureice}$	5 m
ϵ_{Geom} (Boundary smoothing)	0.5
Max distance smoothing (Boundary smoothing)	0.5
ϵ_{Geom} (Contact structure-ice)	0.1
Max distance smoothing (Contact structure-ice	0.1
Ice Model Settings	
Active ice-ice crushing	True
Allows breaking for small floes	True
Crush penetrated floes	False
Ice Crushing Model	ISO19906
Ice Splitting Model	API-RP-2N
Ice Buckling Model	API-RP-2N
Ice Ridge Plug Failure Model	ISO19906
Ice Bending Model	LU
Splitting Parameters	
MaxFloeSidesRatio	5
MinimalAreaForSplitting	20
ContactPointEligibleSplittingAngleDeg	80°
EligibleSplitOpeningAngleDeg	20°
SplitLengthMax	-

Table 3.2: Boundary conditions that will be used for the simulations.

4

Capturing The Sea Ice Characteristics

This chapter addresses what methods are available for obtaining an ice floe size distribution at the spatial scale of an offshore wind farm. The first section aims to give an overview of the currently existing models for acquiring an accurate representation of the ice field in the Southern Baltic Sea. It then analyses how one of these methods, image processing, can correctly be applied to images that are available for the Northern Baltic Sea, as no imagery showing sea ice was available for the Southern Baltic Sea. Next, the results are evaluated using a statistical test and a comparison to literature for other icing seas.

4.1. Floe Size Distribution

Ice fields generally consist of an assortment of individual ice segments, so called floes, that can differ in size, shape and thickness. An effective way of describing these fields is by classifying them based on their floe size distribution (FSD). The FSD captures the sea-ice response to oceanic and atmospheric forcing and helps understanding its seasonal evolution. A field that consists of a high fraction of small floes will melt more rapidly and drift with less resistance than a field with predominantly large floes. This interplay between the ice and ocean goes both ways, as gaps in the ice field can influence energy transfer between the atmosphere and ocean (Bateson et al., 2020). The FSD also affects mixing in the upper-ocean layer, resulting in buoyancy fluxes that may lead to small ocean currents. The slope of the FSD also follows seasonal trends, as Denton et al. (2022) found a steepening of the FSD-slope during summer, implying the proportion of small floes to large floes is increasing. This may be related to the melt and breakup of floes starting in spring and continuing into summer. By the end of summer, the large ice floes have broken into smaller floes surrounded by more open water (Perovich et al., 2014). Therefore, an accurate FSD should be obtained for characterizing the state of the sea ice in the Southern Baltic Sea. The next section aims to answer which methods are available for obtaining an ice floe size distributions at the spatial scale of an offshore wind farm.

4.2. Obtaining the Floe Size Distribution

Large scale climate models capture global physical phenomena and are traditionally made to provide output such as ocean currents and wind speed with grid cells having dimensions of 50 – 100 km. As ice cover is an important factor in modelling the climate, these models also provide information on ice extent and thickness. However, ice breaking physics are not included in these models, therefore they impose the FSD shape, rather than allowing it to emerge from physical processes acting on individual floes. Recent studies exist that describe how ice physics can be included into large scale climate models, and show to capture first-order characteristics of FSDs (Roach et al., 2018). Observations of ice floes indicate that they range from several tens of meters to a few kilometers in diameter, while wind farms can span an area of 10 x 10 km. Distinguishing a high number of floes in a 10 x 10 km area would thus require a resolution up to several tens of meters. Thus, the spatial scale of climate models is too coarse for the purpose of obtaining a representative FSD for the scale of an offshore wind farm.

The NEMO (Nucleus for European Modelling of the Ocean) is a coupled ocean-sea ice model that can simulate sea ice dynamics on both long- and short term and provides ice thickness and concentration (Hordoir et al., 2019), but accurately simulating the FSD remains challenging (Herman et al., 2011). Furthermore, the highest resolution implemented in a global NEMO domain is 6.25 km (Iovino, 2014), which is still too coarse for the purpose of this thesis.

The CICE (Community Ice CodE) is a sea ice model that simulated thermodynamic and dynamic pro-

cesses of sea ice. It can be coupled with large scale climate models to accurately simulate sea ice characteristics. It can capture the most important processes of sea ice dynamics, such as fragmentation and drift, but does so on a scale that is still too large for providing accurate conditions within a wind farm. The smallest grid that can be achieved with CICE is approximately 2.8 km (Roach et al., 2018; Bateson et al, 2022) on a 24-hour timescale (Hopkins, 2006). Challenges remain in simulating the FSD accurately at higher resolution, since relevant small-scale processes are not resolved within each grid cell (Gao, 2011).

The Helsinki Discrete Element Model (HiDEM) is capable of simulating ice dynamics up to 100 x 100 km at 8 m resolution and can provide the according FSD (Åström et al., 2024). This is because it uses discrete elements to represent floes (which are adjustable in size), and thus resolves the interactive forces between them. HiDEM focuses on mechanical behaviour and fracture of ice and relies on external data or models to provide environmental conditions, such as large scale climate models. The ability of HiDEM to simulate ice dynamics is limited to certain time constraints. A challenge with HiDEM is that simulating fracture dynamics requires a time step of 0.0025 seconds, while timescales for sea ice dynamics are much longer. To simulate 1 hour of ice dynamics, 3.6 million time steps are needed. Therefore practical simulation times are constrained to a maximum of several tens of hours, depending on the available computational resources. Considering the presently available resources, HiDEM is not a feasible option.

An alternative approach to creating a digitalized broken ice field is to apply image processing on satellite images. These algorithms identify individual floes and fit a power law to describe the FSD (Zhang et al., 2015; Zhou et al., 2023). This method is one of the best ways to observe ice conditions, as it can suppress ambiguities, uncertainties, incompleteness, and errors about the ice floes and their environment. The precise, spatially continuous measurements that can be collected by cameras are very suitable to obtain detailed localized information on the geometry of sea ice floes (Zhang et al., 2015). However, the limited field of view of satellite instruments often leads to capturing very large floes incompletely (Stern et al., 2018). Furthermore, the number of images that are available are determined by the revisit time and orbital path of a satellite. This can lead to extended periods for which there is no imagery available.

Given that cloud cover is sufficiently low and the image resolution is high, image processing can thus yield very accurate floe size distributions for a selected day. It is therefore chosen to apply image processing for acquiring an FSD that is representative of the Southern Baltic Sea.

4.3. Image Processing

The image processing in this thesis is conducted using satellite images from the Multispectral Imager (MSI) instrument aboard Sentinel-2 L2A that samples 13 spectral bands, enabling for a resolution of 10 - 60 m (European Union et al., 2018-2024). This means that all floes larger than 60 m can be identified. A cloud cover up to 25% is chosen to be accepted here. This is necessary, as the greyscale of cloud pixels can not be separated from ice pixels, thus ice floe boundaries are not identified properly. For acquiring the images, the Copernicus Browser was used that contains the images captured during the Copernicus programme (European Union et al., 2018-2024). As no Copernicus imagery was available that shows ice conditions for the Southern Baltic Sea, images from the Northern Baltic Sea are used. This results in 20 images that are all captured in February during the period 2018 – 2024. In this month, the ice extend in the Baltic Sea is maximum (Karvonen et al., 2024). For all other images, the satellite paths did not cross the Baltic Sea or the cloud cover was too high. Furthermore, only floes with sufficient thickness can be used, as thin ice is less reflective, making it harder to separate from ocean pixels. Therefore, only images from February provided sufficient quality for image analysis. An example of an image from February 18th 2024 can be found in Figure 4.1a. An overview of the settings that were used to retrieve the images from the Copernicus Browser (European Union et al., 2018-2024) can be found in Table 4.1.

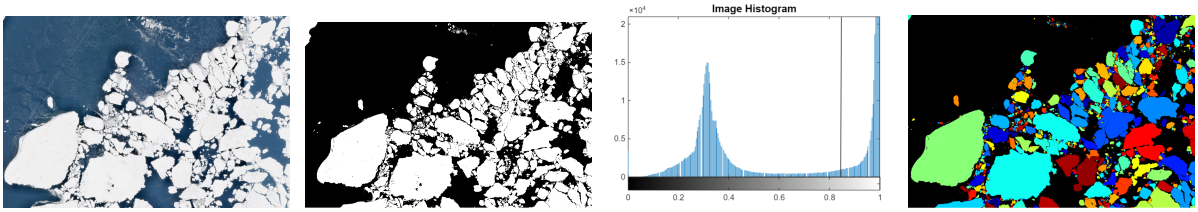

Figure 4.1: Detailed image processing steps for ice floe area detection. (a) Original image (European Union et al., 2018-2024), (b) Classified image using binary thresholding, (c) Image histogram using a threshold of 0.85 depicted by the black vertical line, (d) Processed image before cut-off along edges.

Details	Description
Satellite	Sentinel-2 L2A
Instrument	Multispectral Imager (MSI)
Selected layer	True Color (bands B2, B3, B4)
Period	2018 - 2024
Location	Southern Baltic Sea
Average Image Dimensions	50 x 25 km (x/y)
Accepted cloud cover	25%

Table 4.1: Copernicus Browser settings that were used for retrieval of the satellite images.

The image processing described by Denton et al.(2022) can now be applied, using the approach that is outlined in the following. Each image is classified into ocean pixels and ice pixels based upon a greyscale threshold. Ice pixels correspond to pixel values close to one, while dark ocean pixels correspond to values near zero. The binary black-white image that is used for this can be seen in Figure 4.1b. Ideally, the greyscale histogram contains a peak at the low end of the spectrum and a peak at the high end of the spectrum. The threshold must then fall in between these peaks. An example is shown in Figure 4.1c, for which a greyscale threshold of 0.85 was found to be optimal. For most images, the peaks are flattened or a third peak appears that corresponds to thin ice or melt ponds. Selecting a low threshold can reduce these features, but small floes ($<$ 40 m) do not separate well as the pixel values of the floe-edges are often similar to the values of these features. Therefore, a sufficiently high threshold should be chosen so that these small-floe-boundaries are well defined, which can be checked visually. Floe edges of large floes remain well-defined, even though a high threshold may lead to the growth of ocean pixels in the interior of large floes. For the Sentinel-2 L2A images, the optimal threshold values were found to range from 0.75 to 0.95. After choosing a threshold, the image is then segmented via an iterative erosion-expansion scheme in which the algorithm converts floe-edge pixels to ocean pixels until a clear separation of floes is achieved. This can be verified by a visual check. The segmented floes are then labelled and expanded to their original size. During the first iteration, only the largest floes are eroded while during the subsequent iterations the small unsegmented floes are separated. The number of iterations can be specified by the user, but for all images four iterations were sufficient for segmenting the floes. Choosing a high threshold value will also lead to less iterations being required (Denton et al., 2022). The resulting image is displayed in Figure 4.1d. Lastly, the floes that cross the image borders are removed (since these are 'incomplete'). To enable correctly extracting the floe areas from an image, it is essential that the image is exported as TIFF (Tag Image File Format). This format preserves geospatial metadata, so that the image resolution is defined as a specific number of degrees per pixel in both latitude and longitude using the WGS84 (EPSG:4326) coordinate system. A MATLAB code was created that identifies the number of pixels in each image and converts the image dimensions to meters, knowing that: $1^\circ_{\text{lat}} = 110.57$ km and $1^\circ_{\text{lon}} = 111.32 \cdot \cos(\text{latitude})$ km. The code can be found in Appendix A.1. The floe areas can then be retrieved from the image to construct the FSD.

4.4. Statistical Analysis of the Floe Size Distribution

Many observational studies have been conducted for acquiring an ice floe size distribution. While the spatial and temporal varying nature of the floe size distribution can explain part of the variability between studies, it may also be because there is no standardized way of describing FSDs. FSDs are most often reported to follow a power law distribution. A common approach is to plot the data on log-log scale and use least-squares method to estimate the slope of the straight line. This method generates significant errors under common conditions and therefore yields biased estimates. Maximum likelihood estimation has in general proved to be the most accurate way of fitting the corresponding parameters according to Virkar et al. (2014). Therefore, this method is chosen in this thesis. Afterwards, a goodness-of-fit test should be conducted to test if a power law is an appropriate way of describing the FSD.

The power law distribution follows the probability function $p(x) \propto x^{-\alpha}$ in which $\alpha > 1$ is the exponent or scaling parameter and the power law is valid above the lower boundary of the observed floe sizes, defined as x_{min}. A set of methods was introduced by Clauset, Shalizi and Newman (2009) for fitting and testing the power law hypothesis for both continuous and discrete data. This approach combines maximum likelihood estimation for fitting a power law model, a distance-based method for automatically identifying x_{min} and a goodness of fit test based upon the Kolmogorov-Smirnov (KS) statistic to verify if the power law hypothesis is valid. The maximum likelihood estimator is in general the preferred method for determining the parameters of the FSD as it does not rely on specified bins or fitting ranges (Hwang et al., 2017; Stern et al., 2018). The output of this method is the power law exponent α, x_{min} and the $p - value$ (or probability value). The $p - value$ is defined as the probability of obtaining test results at least as extreme as the results that are actually observed, assuming that the null-hypothesis is correct. The null-hypothesis in this thesis is that the FSD can be described by a power law model. A small $p - value$ indicates that such extreme data would be very unlikely to occur under the null-hypothesis, indicating that the null-hypothesis should be rejected. A large $p - value$ means that the data is more likely under the null-hypothesis. According to Virkar et al. (2014), if $p \geq 0.1$, a power law is considered as a plausible distribution for describing the floe size distribution.

It is important to note that the FSD can be represented in two ways. It may be described in a non-cumulative form $f(x)dx$ or a cumulative form $F(x)$, which are related via $f(x) = -dF/dx$. Officially, the non-cumulative form is called the probability density function and the cumulative form is the complementary cumulative distribution function, but in literature they are often both referred to as the FSD. The main difference between these is that the cumulative FSD is a power law with exponent one greater than that of the non-cumulative FSD (Stern et al., 2018). The method described by Clauset, Shalizi and Newman (2009) uses the cumulative FSD to fit a power law. This procedure was applied to the 20 Sentinel-2 L2A images. The fit that was made to the image shown in Figure 4.1a can be found in Figure 4.2.

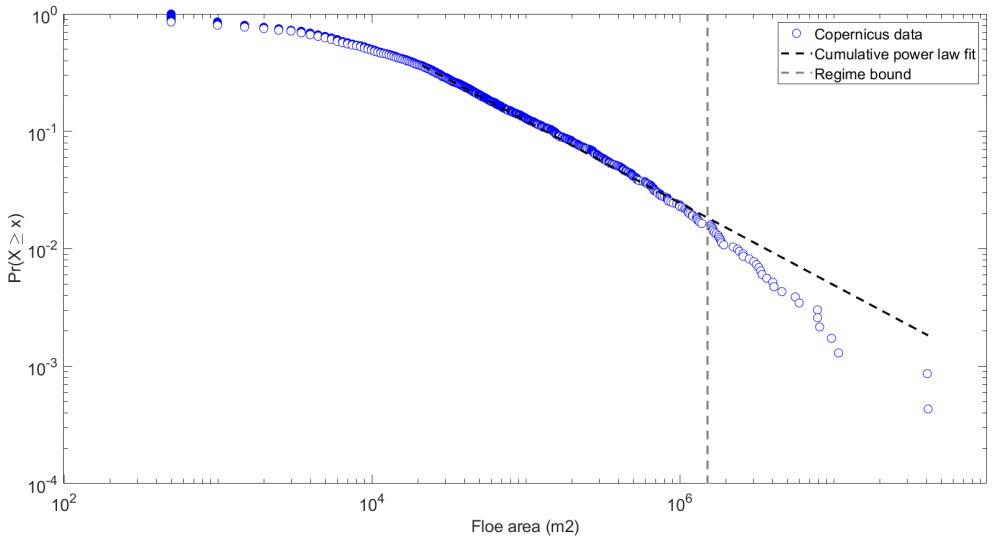

Figure 4.2: Upper-truncated power law that has been fitted to the cumulative FSD of Feb 18 2024-2, having properties $\alpha = 1.70$ and $x_{min} = 2.14 \times 10^{-2}\ km^2$. The dashed grey line shows the boundary between the power law regime and the fall-off regime, which is marked by a floe size of $x_{bound} = 1.52\ km^2$. For $x > x_{bound}$ a clear fall-off regime is visible and the FSD can no longer be described by one single power law.

An implicit assumption in using $F(x)$ for fitting is that the range of floe sizes can extend to infinity, since $F(x) \to 0$ only if $x \to \infty$. In reality, the floe size is bounded by a maximum floe size b because of physical limitations, the cut-off from image processing and satellites often failing to capture the largest floes. If a is defined as the minimum floe size, the non-cumulative form follows a power law $p(x) \propto x^{-\alpha}$ over the range $a \leq x \leq b$, while the cumulative form follows $F(x) = (x/a)^{-\alpha+1}$ for $x \geq a$ and $b \to \infty$. Now, an upper-truncated cumulative power law $F(x) = (x/a)^{-\alpha+1} - R$ can be introduced that ensures $F(b) = 0$, in which $R = 1/(r^{\alpha-1} - 1)$ with $r = b/a$. The non-cumulative form of the power law follows a straight line with slope $-\alpha$ on a log-log plot in between the bounds a and b. However, the cumulative power law shows concave-down curvature for larger floe sizes. This effect is due to the mathematical behaviour of the cumulative power law. It can also be explained by satellite images often failing to capture the largest floes (Stern et al., 2018). This can be amplified by the image processing algorithm, as it cuts off the floes along the edges, which often tend to be the largest.

For the upper truncated power law, two zones can now be defined. Since the cumulative FSD will be near a pure power law for $(x/a)^{-\alpha+1} \gg R$, it is said that $F(x)$ is in the power law zone for $(x/a)^{-\alpha+1} \geq 10R$. In this regime, the distribution can be described by one single power law. For $(x/a)^{-\alpha+1} < 10R$, $F(x)$ shows concave down behaviour, which is called the fall-off zone. The size of the power law zone increases for larger values of α and a wider range of floe sizes (high b/a). For these values, the majority of the fitted distribution would fall within the power law zone. The point where the upper-truncated power law equals $10R$ thus marks the boundary between the two regimes (Stern et al., 2018). The floe size that corresponds to this value is called x_{bound}. The characteristics for the 20 Sentinel-2 L2A images that have been processed in the above described way can now be found in Table 4.2.

Image-id	α	$x_{min}\,[km^2]$	$x_{max}\,[km^2]$	$x_{bound}\,[km^2]$	$p-value$
10 Feb 2024-2	1.78	0.011	18.2	0.95	0.32
18 Feb 2024-1	1.65	0.019	69.8	1.96	0.51
18 Feb 2024-2	1.70	0.021	41.1	1.52	0.34
18 Feb 2024-3	1.75	0.025	26.3	1.23	0.69
18 Feb 2024-5	1.76	0.0048	9.60	0.49	0.80
18 Feb 2024-7	1.80	0.00093	4.31	0.24	0.29
25 Feb 2023-1	1.67	0.21	103	3.21	0.77
25 Feb 2023-2	1.76	0.094	114	5.41	0.94
28 Feb 2018-3	1.72	**0.25**	774	31.6	0.96
28 Feb 2020-1	1.76	0.082	74.7	3.65	0.89
26 Feb 2020-3	1.79	0.0011	18.5	1.01	0.60
11 Feb 2019-2	1.74	0.020	59.6	2.69	0.41
11 Feb 2019-3	1.64	0.023	40.8	1.11	0.42
11 Feb 2019-4	1.62	0.017	39.9	0.93	0.78
11 Feb 2019-5	1.63	0.0058	12.7	0.32	0.77
11 Feb 2019-6	1.82	0.014	30.5	1.83	0.14
11 Feb 2019-7	1.63	0.015	32.8	0.85	0.61
25 Feb 2021-4	1.62	0.0013	1.47	0.034	0.73
25 Feb 2021-7	1.66	0.0046	5.44	0.16	0.56
25 Feb 2021-8	1.69	0.0013	1.97	0.69	0.48
Average	**1.71**	**0.041**	**73.9**	**2.96**	**0.60**

Table 4.2: Characteristics of the power law that is fitted to 20 Sentinel-2 L2A Images. α is defined as the slope of the power-law, x_{min} is lower boundary of floe sizes within the power law regime. x_{max} is the maximum observed floe size across al images, x_{bound} is the upper boundary of floe sizes within the power-law regime. The $p-value$ is the probability of obtaining results at least as extreme as the results that are actually observed, assuming the null-hypothesis is correct. The null-hypothesis in this thesis is that the FSD can be described by a power-law model. If $p \geq 0.1$, a power law is considered as a plausible distribution for describing the FSD. Therefore the null-hypothesis is accepted. The last number of the image-id refers to the subsection of the image that was used for a certain date, as the satellite path can be divided into multiple images. The acquired parameters can be used for the generation of synthetic ice floe fields.

It should be noted that a high $p-value$, as observed in Table 4.2, does not verify the correctness of a power law fit to the data. Therefore, selecting the parameters corresponding to the image with the highest $p-value$ is not a correct approach. This can be due to two reasons. First, there may exist alternative distributions that fit the data equally well or even better, as the $p-value$ only gives an indication of the fit of the model under the assumed null-hypothesis. In this case, a likelihood ratio test can provide additional verification. Secondly, for a low amount of data points, the observed data may follow a power law distribution even if it is not the underlying distribution. This is because very little data makes it difficult to rule out the power law (Virkar et al., 2014). As the power-law, or upper-truncated power-law, is the most widely accepted way of describing the FSD in sea ice dynamics, this thesis assumes that performing the likelihood ratio test is not necessary. Therefore the FSD will be described by a power-law in this thesis. From Table 4.2 it can thus be concluded that for all images the power law is a plausible way of describing the FSD. To improve the statistical representativeness of the FSD-characteristics that will later be used for simulations, the average of all the values in Table 4.2 is taken. This results in $\alpha = 1.71$, x_{min} = $0.041\ km^2$, x_{bound} = $2.96\ km^2$ and x_{max} = $73.9\ km^2$.

4.5. Comparison to Other Icing Seas

Because of the spatial and temporal variability of the FSD and different fitting procedures being used in literature, it is difficult to compare the obtained FSD to other studies. Studies that used the cumulative distribution for fitting generally state an α-value in the range of 1 - 2. Denton et al. (2022) applied the same image processing algorithm and found a most-likelihood estimation of $\alpha = 1.77 \pm 0.11$, using a non-cumulative distribution. The lower bound to the power law behaviour x_{min} was found to vary significantly for the different images used by Denton et al. (2022) , ranging from 10 - 10000 m^2. The results from the 20 Sentinel-2 L2A images also show a highly varying x_{min}, ranging from 928 - 250000 m^2. The different ranges of x_{min} may be explained by the Sentinel-2 L2A images having a lower resolution (max. 10 m compared to 1 m), while the higher upper bound can be explained by bigger

Sentinel-2 L2A image dimensions, identifying more large floes. The value of $\alpha = 1.71$ is however very similar to the one found by Denton et al. (2022) for the Canada Basin. Part of the discrepancy in α might be explained due to variations in latitude and months in which the images were captured. Images from the Canada Basin span all months, which can explain a lower probability of observing very large floes (corresponding to a higher α), caused by melt of ice during summer. This may be partially compensated by the Canada Basin being at higher latitude than the Baltic Sea. It can therefore be assumed that the obtained statistical characteristics for the sea ice in the Baltic Sea result in an accurate representation of the FSD.

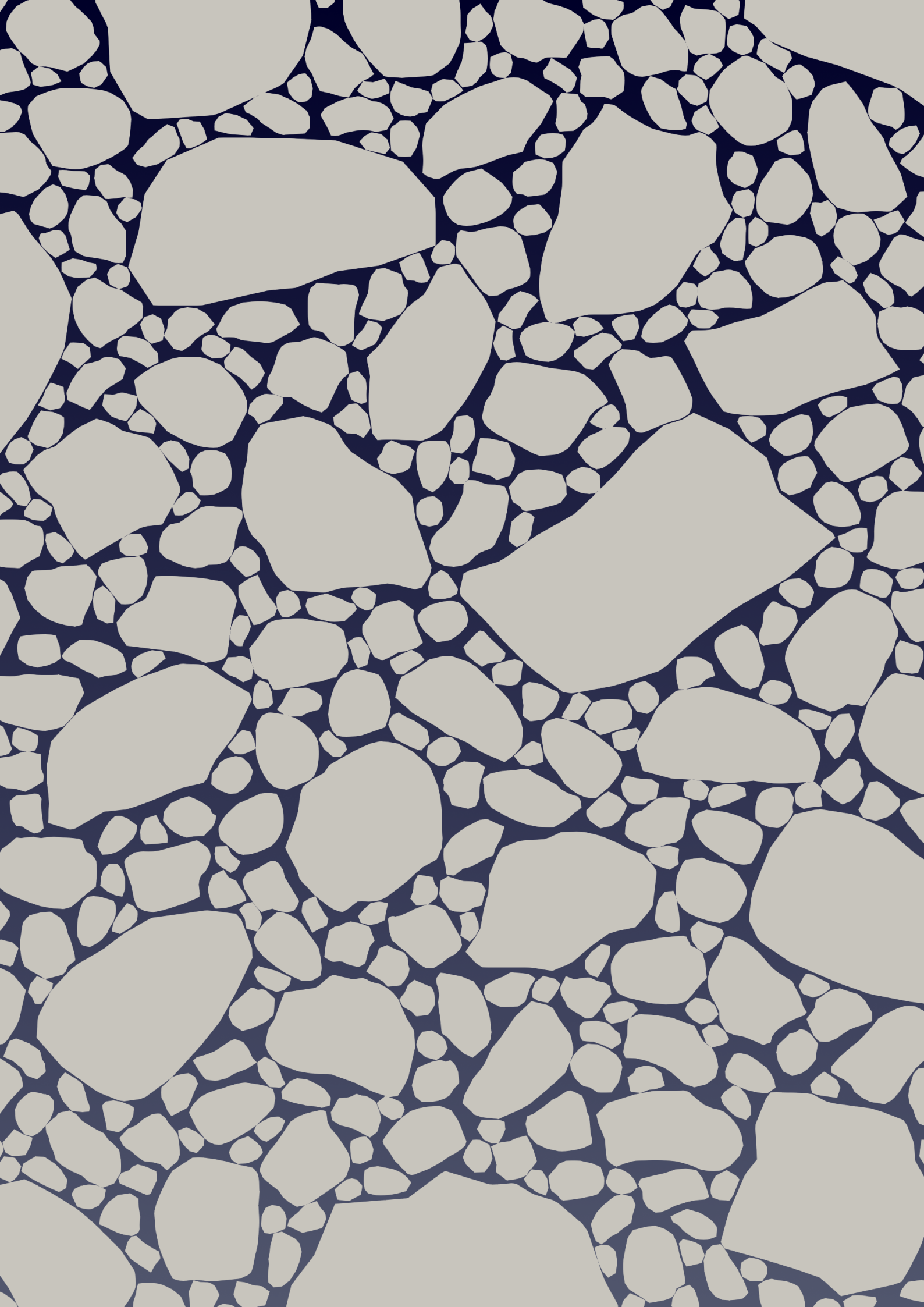

5
Synthetic Ice Floe Field Generation

The present Chapter is a continuation of Chapter 4 and aims to address how the acquired FSD can be accurately translated into a representative ice floe field within the offshore wind farm domain. This chapter will therefore establish a method for accurately converting the image processing results to a floe field that can be implemented in SIBIS. First, it describes the code that is used for the creation of a synthetic floe field. Then, it is explained how the FSD-parameters should be implemented in the floe field generator, connecting the two methods. In the last part of this chapter, the synthetic floe field that is created based on the image processing results is verified to ensure that the floe field generator does not introduce any errors.

5.1. Floe Placement Procedure

The FSD that was found using image processing is representative of a typical floe size distribution in the Southern Baltic Sea. Therefore, it will be used for generating synthetic floe fields. The use of synthetic ice floe fields enables the development of a generalized method for generating floe fields with varying size, scale, and sea ice concentration, suitable for application in SIBIS. The code that will be used for generating these fields has been developed by Brenner (2024). This code takes a specified sea ice concentration and floe size distribution as input and randomly generates an ice field within an adjustable domain. The procedure is as follows:

1. First, a list of floe sizes is generated that follows the prescribed FSD and satisfies the sea ice concentration within the defined boundaries. For a fixed minimum- and maximum floe size, increasing the domain thus leads to more floes being generated.
2. The floe shapes are randomly selected from an inventory of floe shapes (created by tracing a satellite image of sea ice floes) by sampling from a uniform distribution. After this, they are scaled and randomly rotated by sampling rotation angles from a uniform distribution. Lastly, the floes are placed inside the specified boundaries. For the placement, first a list of candidate floe positions is created by sampling random locations from a 2D probability distribution P. For each draw, it generates a uniformly random number between 0 and 1 and uses the inverse transform to map the number into the shape specified by P. The inverse transform finds the position for which the CDF of P is equal to the randomly drawn number. The result is still random but biased according to P. The probability distribution favours locations farther away from previously selected locations by updating P after each floe placement. This makes floe placement near other floes less likely. This procedure starts with the largest floes and then fills up the rest of the domain. In this way, it creates candidate floe positions in between the previously placed floes, as seen in Figure 5.1a.
3. The inverse transform sampling happens inside the creation of candidate positions. The placement of each floe is rejected or accepted based on overlap with neighbouring floes. A limit is placed upon the number of allowed rejections to avoid an infinite loop. If the limit is exceeded, the placement fails and the algorithm tries to place the floe at another empty location. The procedure stops checking the list of candidate floe positions once a candidate position for a specific floe is accepted. The probability distribution P is then updated and the procedure is repeated for the next ice floe.
4. This procedure is repeated until all the floes have been placed. For high sea ice concentrations ($\geq 80\%$), convergence is not guaranteed since the algorithm needs to fill up more tiny spaces in between floes. This can especially be the case for a high lower limit x_{min} of floe size, since this

increases the probability of overlapping. A narrow range of minimum- to maximum floe size can also lead to nonconvergence.

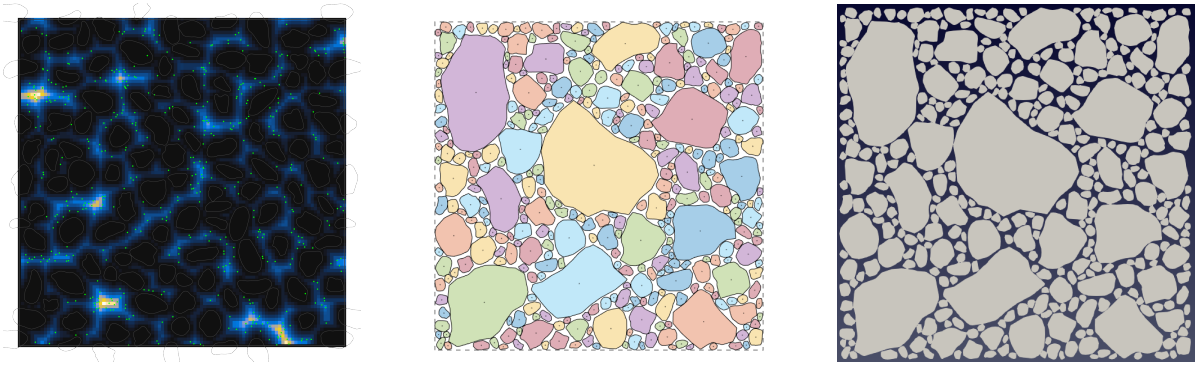

(a) Candidate floe positions (displayed by the green dots) are created in between the previously placed floes using a probability density function (Brenner, 2024).

(b) The ice field that is generated by the floe field generator for a 30 x 30 km ice field with floe radii of 282 - 4850 and SIC 80%.

(c) The floe field that is converted to SIBIS-format and visualized in Paraview. The floe field is 30 x 30 km, floe radii of 282 - 4850 m and SIC 80%

Figure 5.1: Procedure of floe field generation

5.2. Connecting Image Processing To Synthetic Floe Fields

The averaged FSD-parameters from image processing can be used to create a synthetic floe field that is typical for the Southern Baltic Sea. A necessary step for making use of the floe field generator is to convert the floe areas in Table 4.2 to an equivalent circle having radius r. The floe field generator accounts for the concave-down behaviour of the upper-truncated power law in the fall-off regime. Thus, the average x_{max} can be used as input for the maximum floe size, instead of x_{bound}. The range of $x_{min} - x_{max}$ that the floe field generator can handle is limited. Thus, the minimum floe size should be increased to ensure convergence, as lowering the maximum floe size will most likely be more impactful for simulation results. x_{min} is therefore chosen as the maximum value of the smallest observed floes, namely $0.25\ km^2$ as marked in Table 4.2. This results in r_{min} = 282 m, r_{max} = 4850 m and $\alpha = 1.71$ as input for the floe field generator. The cumulative distribution of floe areas that corresponds to this input is displayed by the blue line in Figure 5.3. Within the prescribed boundaries of floe sizes, the floe field generator then creates randomly shaped polygons by reshaping these circles and subsequently creates a floe field. The output of the floe field generator is shown in Figure 5.1b. Lastly, a MATLAB script was made to convert the floes to SIBIS by extracting the coordinates of the floe outlines, writing them to an XML-format and rearranging them in a counterclockwise manner. This code can be found in Appendices A.2 and A.3. A visualization in Paraview of the generated floe field can be seen in Figure 5.1c.

5.3. Verification Of The Generated Floe Field

The FSD corresponding to the synthetic floe field presented in Figure 5.1c can now be compared to the Sentinel-2 L2A imagery. In Figure 5.3, the light blue line represents the cumulative distribution of floe sizes for the synthetic floe field, while the other lines correspond to the cumulative distribution of the image processing results. Note that the data in Figure 5.3 is only plotted for $x > x_{min}$, which explains why the lines do not show concave behaviour for the lowest floe sizes, as was seen in Figure 4.2. To clarify this, the dataset of February 18th 2024-2 shown in Figure 4.2 is also displayed in Figure 5.3 by the green line. Now the synthetic floe field can be compared to the image processing results. As expected, their slope of $\alpha = 1.71$ is equal and the floe field generator samples floes in the full range of the prescribed $x_{min} - x_{max}$. While the Sentinel-2 L2A images show a light concave-down tendency for large floe sizes, this behaviour is not apparent for the synthetic floe field. This can be explained by the image processing that cuts off the floes along the edges of the satellite imagery, while the floe field generator only creates floes within predefined boundaries. Therefore, no floes are cut-off from the synthetic floe field. For verification, the image processing was also applied to the synthetic floe field. The procedure can be seen in Figure 5.2.

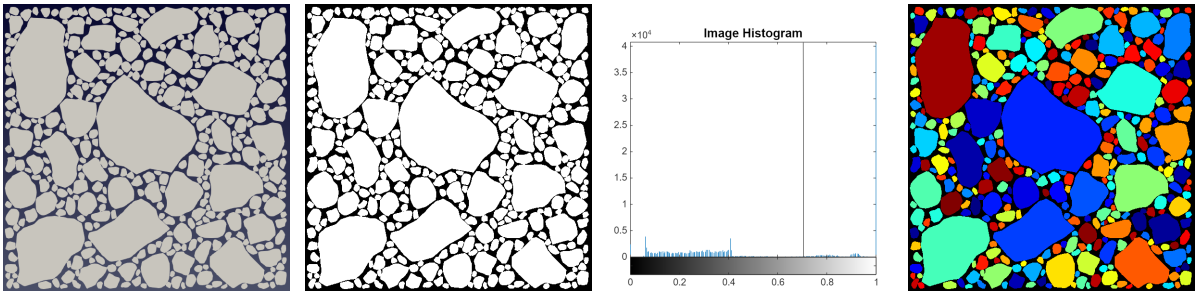

Figure 5.2: Verification of the image processing applied to the synthetic floe field. (a) Original image of the synthetic floe field, (b) Classified image using binary thresholding, (c) Image histogram using a threshold of 0.70 depicted by the black vertical line, (d) Processed image after cut-off along the edges.

As the synthetic floe field can not be exported as TIFF, the PNG is scaled based upon the largest observed floe size. In this case, the cut-off effect is not visible, as the floe field generator creates a floe field that fits between predefined bounds. This can be seen in Figure 5.2d, showing the floe field after cut-off. The resulting FSD that is found by applying the image processing to the synthetic floe field is depicted by the orange markers in Figure 5.3. It can be observed that the image processing does not affect the floe size distribution for the synthetic floe field.

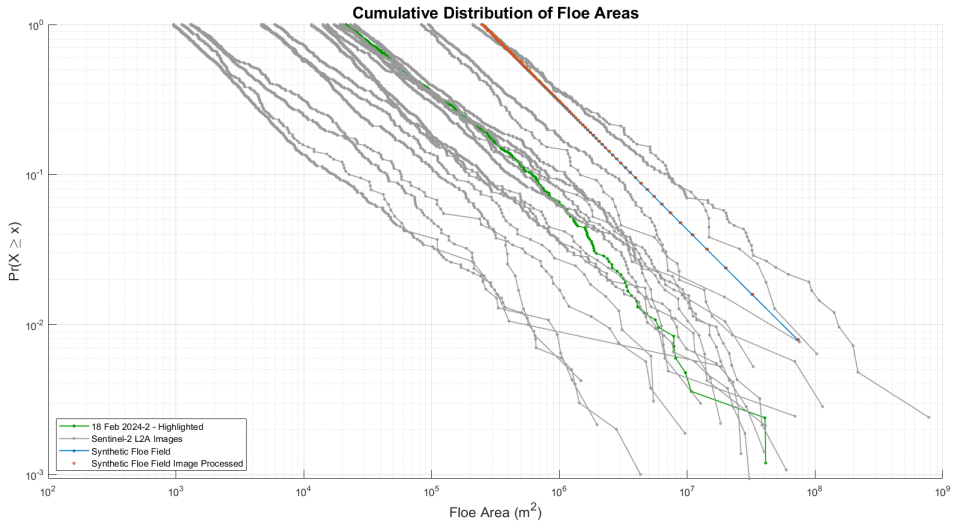

Figure 5.3: FSD's obtained from image processing the Sentinel-2 L2A images are plotted cumulatively using log-log axes and compared to the cumulative FSD from the floe field generator. The image processing is also applied to the synthetic floe field. As shown, it does not introduce any errors.

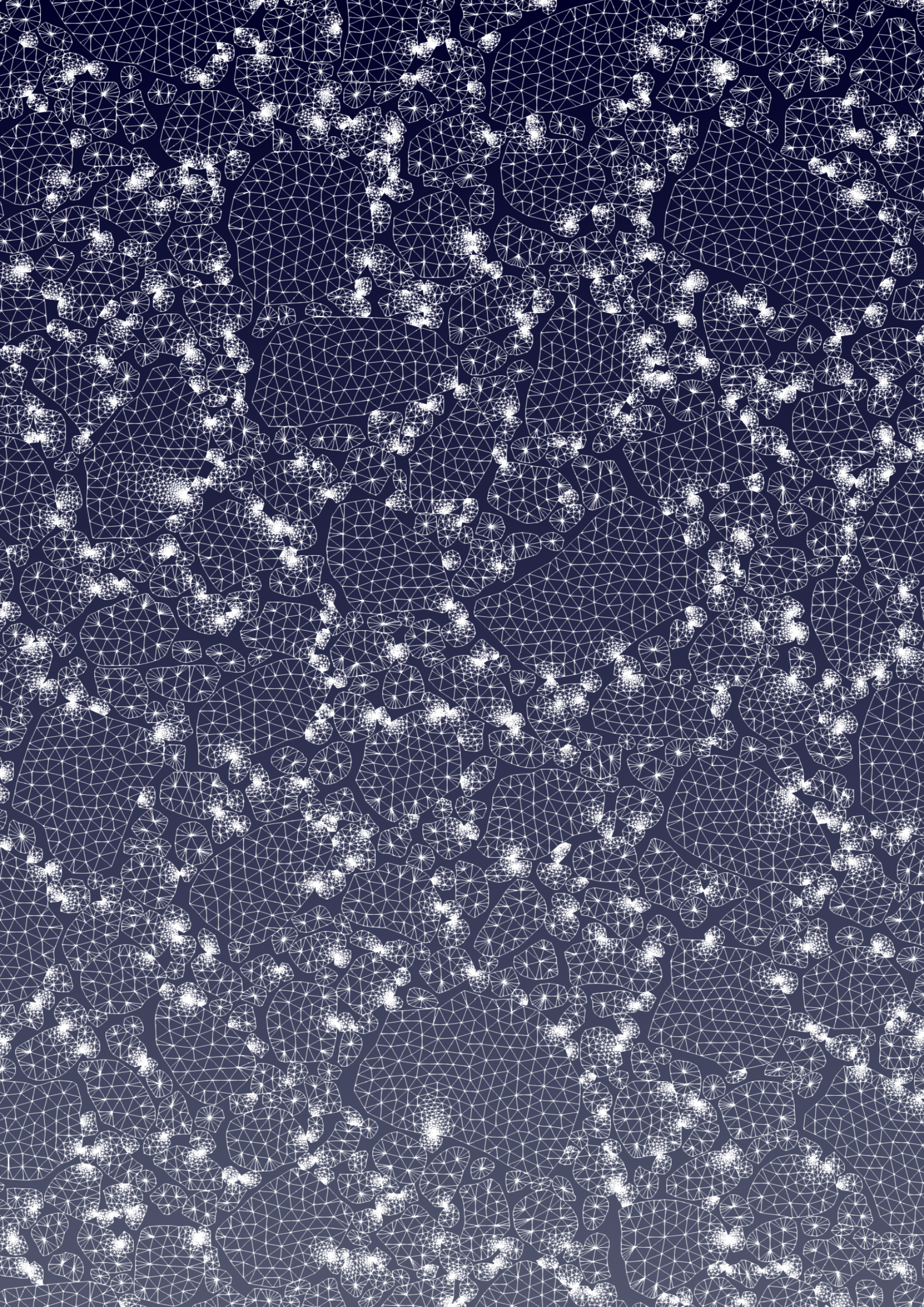

6
Simulation

The main motivation behind this chapter is that it describes the floe fields, variables and wind farm layout that are selected for performing simulations in order to answer the subquestions as formulated in the introduction. The connection between the floe field generator and SIBIS enables to apply floe fields in SIBIS for every type of FSD, varying dimensions of the floe field, different sea ice concentrations and even vary the shapes and orientation of the floes. This will recreate, to some extend, the diverse nature of ice floe fields in reality. The floe fields will be used to simulate two different scenarios. The first scenario being the case where the ice floes are initially located outside the offshore wind farm (OWF), and pushed inside the OWF by the wind. In the second case, a scenario is simulated in which the turbines are fully frozen in by the ice.

6.1. Floes Initially Positioned Outside the OWF

Fast ice consists of stationary ice sheets that are anchored to the coastline, the seafloor, icebergs or other anchor points (Leppäranta, 2011). For most of the ice season, fast ice is stationary, but during a storm it could detach from its anchoring point. The internal stresses due to the drift motion would break up the ice into smaller floes, thus creating a floe field. Assuming a constant wind-forcing over an extended period, the floe field would drift at a velocity of approximately 3% of the wind speed in SIBIS. When this floe field meets an OWF, the ice drift speed will reduce due to the interaction with the support structures. High ice loads will occur due to intermittent crushing and multi-modal interaction at low floe velocity. In combination with wind speeds of 11 to 13 m/s, where turbine operation shifts from optimal power production to steady max power production, high dynamic loads may thus occur (Gravesen et al., 2023). Currently, the design of offshore structures does not account for the ice drift speed reduction, therefore potentially underestimating the fatigue damage. The low ice drift speeds can introduce a new regime - multimodal interaction or intermittent crushing - and can thus become driving for ULS. To assess the reduction of ice drift speed, multiple simulations are performed in SIBIS. A number of floe field layouts is implemented, varying the minimum- to maximum floe size and sea ice concentration. For offshore wind turbine design, a maximum level ice thickness of 0.26 to 0.44 m was found for a 50-year return period in the Southern Baltic Sea (Tikanmäki et al., 2021). An ice thickness of 0.40 m will be used across all simulations for the described scenario. It will now be explained why selecting the sea ice concentration and the maximum floe size as variables is done to perform a sensitivity analysis.

6.1.1. Sea Ice Concentration

There is a possible correlation between sea ice concentration (SIC) and slope α of the FSD. For the Beaufort and Chukchi Seas, the decrease of SIC into summer follows the same behaviour as α (which increases during summer, resembling the melt and breakup or large ice floes, reducing the proportion of larger to smaller floes) (Stern et al., 2018). However, at the Northern Canada Basin there exists no correlation between SIC and FSD-slope from spring to fall (Denton et al., 2022). Since for the image analysis based upon Sentinel-2 L2A data, only images from February were used, is is assumed that the SIC can be varied without having to change α.

When the broken-up fast ice moves towards the OWF, the floes may disperse and lead to different ice concentrations in the OWF. This can highly affect the ice-structure interaction, as a lower sea ice concentration gives more space for redistribution of floes within the wind farm. This is related to the blocking that can occur when multiple floes interlock and start behaving like one large interconnected floe. This process is called bridging (van den Berg et al., 2019). It was found that below a sea ice concentration of 60%, ice-ice interaction rarely happens since the floes are separated far from each

other. The simulations go towards the point of a single floe interacting with a single structure, which is not desired for the purpose of macroscale modelling. Furthermore, Figure 2.4 showed that below a SIC of 80%, the ice drift speed is relatively constant and can still be predicted by free drift theory. Moreover, the floe field generator does not converge for sea ice concentrations above 80%. Therefore, the range of sea ice concentration across the simulations is set to 60 - 80%.

6.1.2. Maximum Floe Size

A single ice floe with a diameter smaller than the distance in between the turbines - which is 1 km - has a relatively high chance of drifting in between the turbines unobstructed, or impacting and rotating around the turbines without breaking. At higher concentrations, some redistribution might be required, but all the floes can drift in between the turbines without having to break. If the floe diameter is equal to 1000 m or higher, breaking or rotating becomes necessary to pass the turbines. Therefore, the maximum floe radius is varied. In addition to a floe radius range of 282 - 4850 m, simulations were performed for 80 - 1000 m and 80 - 300 m.

6.1.3. OWF Layout

All simulations were conducted using a 3 x 3 turbine layout, having an inner distance of 1 km in both x- and y-direction, as seen in Figure 6.1. In reality, offshore wind farms may consist of 50 turbines, which will be referred to as a 'full-scale' layout from now on. This thesis thus only uses a fraction of such a layout. As lateral confinement of the floe field should be ensured, a larger OWF also requires a much larger floe field. The largest floe field in terms of number of floes that is currently implemented consists of $\approx$ 2400 floes. It takes $\approx$ 120 hours for SIBIS to simulate 6 hours of ice drift for this floe field and a 3 x 3 turbine configuration. It is therefore chosen to not increase the number of turbines any further.

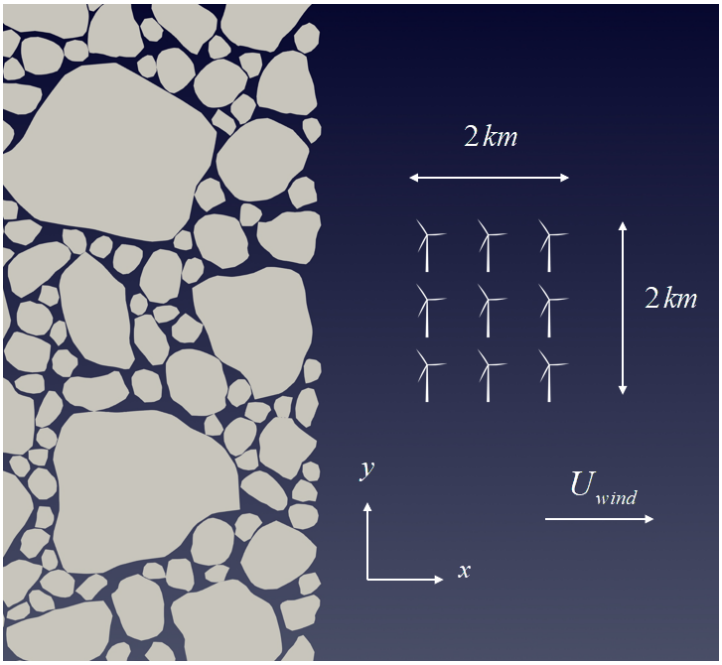

Figure 6.1: Top view of simulation layout (not to scale) for a floe field initially positioned outside the wind farm for a 3 x 3 turbine configuration.

6.1.4. Overview Simulation Cases Floes Originally Outside OWF

Table 6.1 describes all the simulations that were done for the case in which the floes are initially located outside the wind farm. It was found that for the 3 x 3 layout and a maximum floe radius of 300 and 1000 m, a floe field of respectively 12 and 20 km width ensures that the floes interacting with the structures are confined perpendicular to the flow-direction by surrounding ice. This means that the boundaries of the floe field do not expand laterally due to the ice-structure and ice-ice interaction. This expansion is not desired, as the ice floes would start drifting around the offshore wind farm. As ice floe fields in reality

are likely much larger than the offshore wind farms they encounter, the confinement by surrounding ice should be ensured. An alternative for this would be to introduce rigid boundaries along the edges of the ice field, reducing the number of required floes. For large floe radii up to 4850 m, additional confinement should be introduced, as the rotation of large floes during ice-structure impact pushes the other floes towards the boundaries. It is therefore advised to use larger floe fields as the maximum floe radius increases. This leads to a floe field width of 30 km. Figure 6.2 shows the effect of insufficient lateral confinement using a floe field width of 20 km. After 20000 seconds, the interaction with the structures has caused the lateral boundaries to slightly expand.

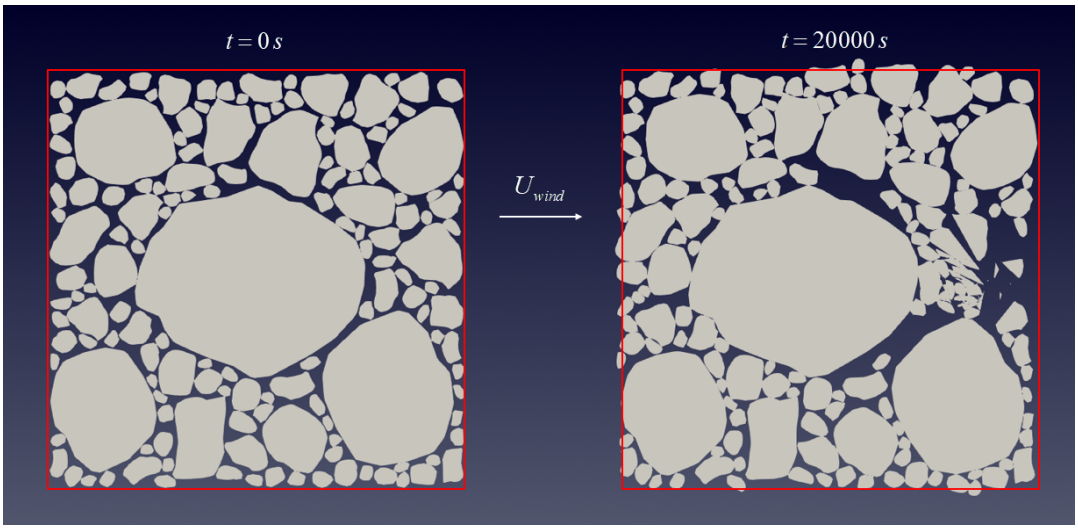

Figure 6.2: The effect of insufficient confinement as shown for a floe field of 282 - 4850 m SIC 80% and dimensions of 20 x 20 km. After 20000 seconds, the ice-structure interaction has pushed the lateral boundaries outward.

Furthermore, it was found that the floe field should be of sufficient length in the flow-direction to enable the first front of floes to be ”pushed” through the OWF. Therefore, all floe field layouts have dimensions of either 12 x 12 km, 20 x 20 km or 30 x 30 km, depending on maximum floe radius.

In addition to performing simulations for varying sea ice concentration and maximum floe size, for each wind farm layout, a simulation was done with the FSD that was found to be representative for the Southern Baltic Sea, covering floe radii of 282 - 4850 m. This simulation serves as a baseline to analyse the influence of changing variables. It was found that for floe fields that either have a high SIC or a narrow range of minimum- to maximum floe size, the minimum floe size should be lowered to achieve convergence of the floe field generator. In these cases, the minimum floe size is selected so that it is still larger than the lowest observed x_{min} = 0.00093 km^2 (or r_{min} = 17 m) during image processing.

OWF-Layout	SIC [%]	Floe Radius [m]	Floe Field Dimension [km]	Description
3 x 3	60	282 - 4850	30 x 30	Baseline
3 x 3	70	282 - 4850	30 x 30	Baseline
3 x 3	80	282 - 4850	30 x 30	Baseline
3 x 3	60	80 - 1000	20 x 20	Vary SIC
3 x 3	70	80 - 1000	20 x 20	Vary SIC
3 x 3	80	80 - 1000	20 x 20	Vary SIC
3 x 3	60	80 - 300	12 x 12	Vary max floe radius

Table 6.1: Simulation cases and their parameters for the scenario in which the floes are initially positioned outside the wind farm.

6.1.5. Theoretical Expectations and Insights from Trial Simulations

At $t = 0$, the floe field is located outside of the wind farm and the ice drift speed is equal to zero. At $t > 0$ the drift speed gradually starts increasing due to the wind forcing. It was found that the floes should be positioned at approximately 400 m distance from the wind farm to reach a steady state free drift speed. This can be found in Figure 3.1a. If the floes that are listed in Table 6.1 were schematized as circles, it would result in a minimum diameter of 160 m and a maximum of 9700 m. Since for all floes the thickness is set to 0.40 m, the aspect ratio l/h is higher than 10^3 for most of the floe field. Therefore the ratio between the ice drift speed and the wind speed is generally expected to be close to the membrane limit of 3%.

The distance in between the wind turbines is equal to 1 km. Only for the last simulation that is described in Table 6.1, all floes have a diameter that is smaller than 1 km. For this floe field, it is expected that the majority of the floes pass the turbines without splitting. All other simulations in Table 6.1 implement floe fields where the majority of the floes have a diameter that is larger than 1 km. Thus, a large fraction of the floes impacts the turbines, rather than drifting in between them. As soon as impact initializes, the free drift condition no longer holds and the ice drift speed / wind speed ratio of 3% is abandoned. The first front of floes fractures into smaller floes as the drift speed is still relatively high (close to 0.3 m/s) for a constant wind speed of 10 m/s. The fracturing front leads to a stagnation of the ice field behind it, reducing its speed while increasing the compactness. Therefore, the ratio between the ice drift speed and wind speed most likely decreases for the second front. Simultaneously, the drift motion for the broken-up front (re)-initiates, and they start to drift towards the second row of turbines. This behaviour was observed in the first trial simulations. Thus, it is expected that the outer edge of turbines at the direction from which the ice field is drifting from, acts as a shield for the other turbines. This outer edge grinds the floe field into smaller pieces that are less affected by the presence of the turbines. Therefore they maintain a higher drift speed. A higher sea ice concentration is expected to generate more stagnation at the first row of turbines, as bridging is more likely to occur. Furthermore, a high SIC is expected to lead to more floes being affected by the presence of the OWF, as floes are positioned closer to each other, leading to more collisions between floes.

6.2. Grown-in Condition

During a winter season, the presence of the turbines creates fixed support points for the ice to grown onto. This can develop into one continuous ice sheet that fully covers the OWF. Such a situation can also occur near shore, where landfast ice is more likely to occur. Under insufficient driving forces, the ice will remain stationary (van der Stap et al., 2024). This intimate contact condition, as described by (Croasdale, 1975), can result in high ice forces when the wind-forcing is sufficient to (re)-initiate the movement of ice. Significant driving forces would be necessary to start up the movement of ice in this condition, as the full-thickness contact leads to high resistance, especially in the case of multiple frozen-in turbines. ISO19906 prescribes the consideration of vertical loads due to tidal variations during a frozen in condition. Furthermore, it considers horizontal thermal expansion loads and horizontal loads induced by ice drift in this scenario. For an 8 m monopile, the thermal expansion force only exceeds the crushing force for an ice thickness lower than 0.21 m (assuming a C_R of 0.98 MPa). It is therefore assumed that crushing is the governing loading mechanism. ISO 19906 states that the horizontal loads from ice drift can occur when the structures are located in an open sea with minimal tidal range and insufficient driving forces, so that the stationary ice prevails for a sustained period (van der Stap et al., 2024). As tidal variations are reported to be minimal in the Baltic Sea (Finnish Meteorological Institute, 2025), a stationary ice sheet is likely to from. Currently, no design standard includes this frozen in scenario alongside existing design load cases (van der Stap et al., 2024). It is therefore tested what wind speeds provide sufficient driving force to initiate the horizontal ice drift in this situation.

6.2.1. Wind Speed

Since the turbines act as anchors to the ice, the ice sheet most likely remains stationary at commonly observed wind speeds of 10 m/s. When the OWF encounters a storm, the turbines remain operable up to wind speeds of 30 m/s and the ice may start to move and crush onto the turbines. Therefore, the wind speed is varied across 10 - 30 m/s.

6.2.2. Ice Thickness
This wind speed at which the ice starts to move is affected by the ice thickness. Low ice thicknesses result in lower resistance. Therefore, crushing, or even splitting of the ice, is initiated more easily. The process is analysed for the maximal level ice thickness that is considered for offshore wind turbine design over a 50-year return period in the Baltic Sea. This results in an ice thickness range of 0.26 - 0.44 m (Tikanmäki et al., 2021).

6.2.3. Distance Outer Turbines - Open Water
It was found that when the distance from the open water (the open water is located at the edge of the ice sheet) to the outer turbines exceeds 1500 m, the ice-structure interaction solely consists of crushing. Below this distance, splitting occurs. Therefore, it is chosen to limit this distance by a minimum of 1500 m to prevent splitting and allow analysing the combination of wind speed and ice thickness that initiates movement of the ice sheet via crushing.

6.2.4. Gap Between Turbine And Surrounding Ice
One of the input parameters that the user can define in the slice tool of SIBIS - the tool that allows positioning the turbines in the middle of the ice sheet by creating circular holes - is the distance between the grown-in turbine and the surrounding ice sheet. When the wind picks up, a bigger margin between the structure and the surrounding ice provides more time for the ice sheet to build up speed. Thus, the spacing between the turbines and the ice is varied across 0.01, 0.1 and 1 m.

6.2.5. OWF Layouts
The grown-in scenario was performed for a 3 x 3 and 4 x 4 turbine layout, as seen in Figure 6.3. For the two configurations, the inner distance between the structures is 1 km in both x- and y-direction. The turbines are positioned at the centre of the ice sheet.

6.2.6. Overview Simulation Cases Grown In
An overview of the simulation cases can be found in Table 6.2. The floe geometry is chosen to be a square as it allows to easily define the surface area and the distance from the outer turbines to the open water.

OWF-Layout	Ice Thickness [m]	Wind Speed [m/s]	Floe Area [km^2]	Gap [m]
3 x 3	0.26 - 0.44	10 - 30	25	0.01 - 0.1 - 1
4 x 4	0.26 - 0.44	10 - 30	36	0.01 - 0.1 - 1

Table 6.2: Simulation cases and their parameters for the grown-in scenario.

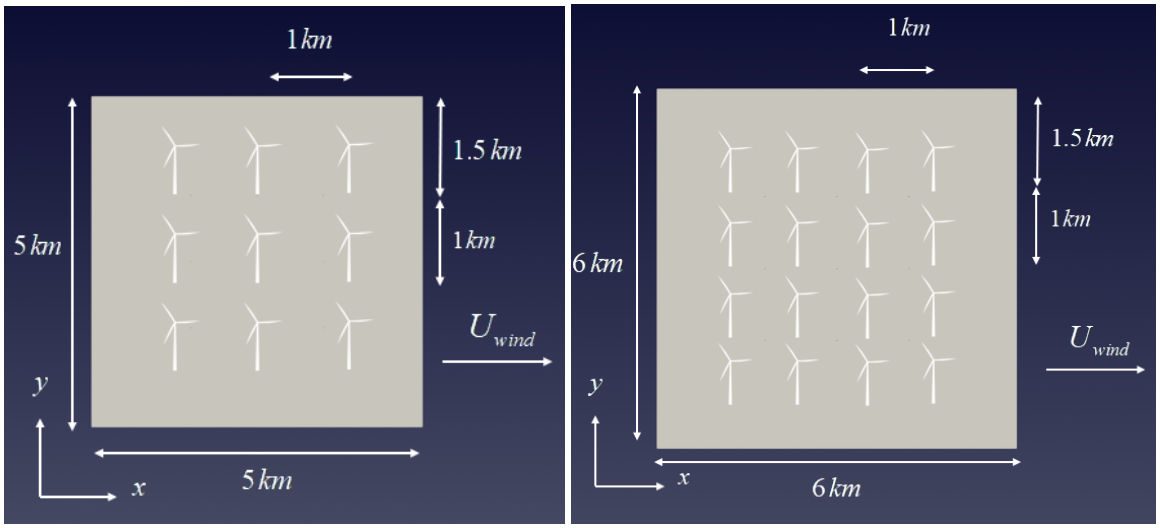

(a) 3 x 3 turbine configuration **(b)** 4 x 4 turbine configuration

Figure 6.3: Top view of simulation layouts (not to scale) for grown-in conditions.

6.2.7. Theoretical Expectations and Insights from Trial Simulations

At $t = 0$ the floe field is located inside the wind farm by using the SLICE tool for SIBIS. At $t > 0$ the wind forcing moves the ice so that it makes contact with the turbines. Before contact, it was observed that the ice has a brief moment to speed up. The speed at the moment of contact is dependent on the distance in between the turbines and the surrounding ice. Due to the full-contact resistance, it is expected that only the highest wind speeds in combination with a low ice thickness initiate sustained crushing. For all other combinations, the ice remains stationary. Furthermore, trial simulations showed that as the distance in between the turbines and the surrounding ice increases, the turbines start penetrating into the ice for lower wind speeds. However, this low wind speed is not sufficient to maintain the crushing of the ice. It is thus expected that the critical wind speed necessary for sustained crushing is not dependent on the distance in between the turbines and the ice.

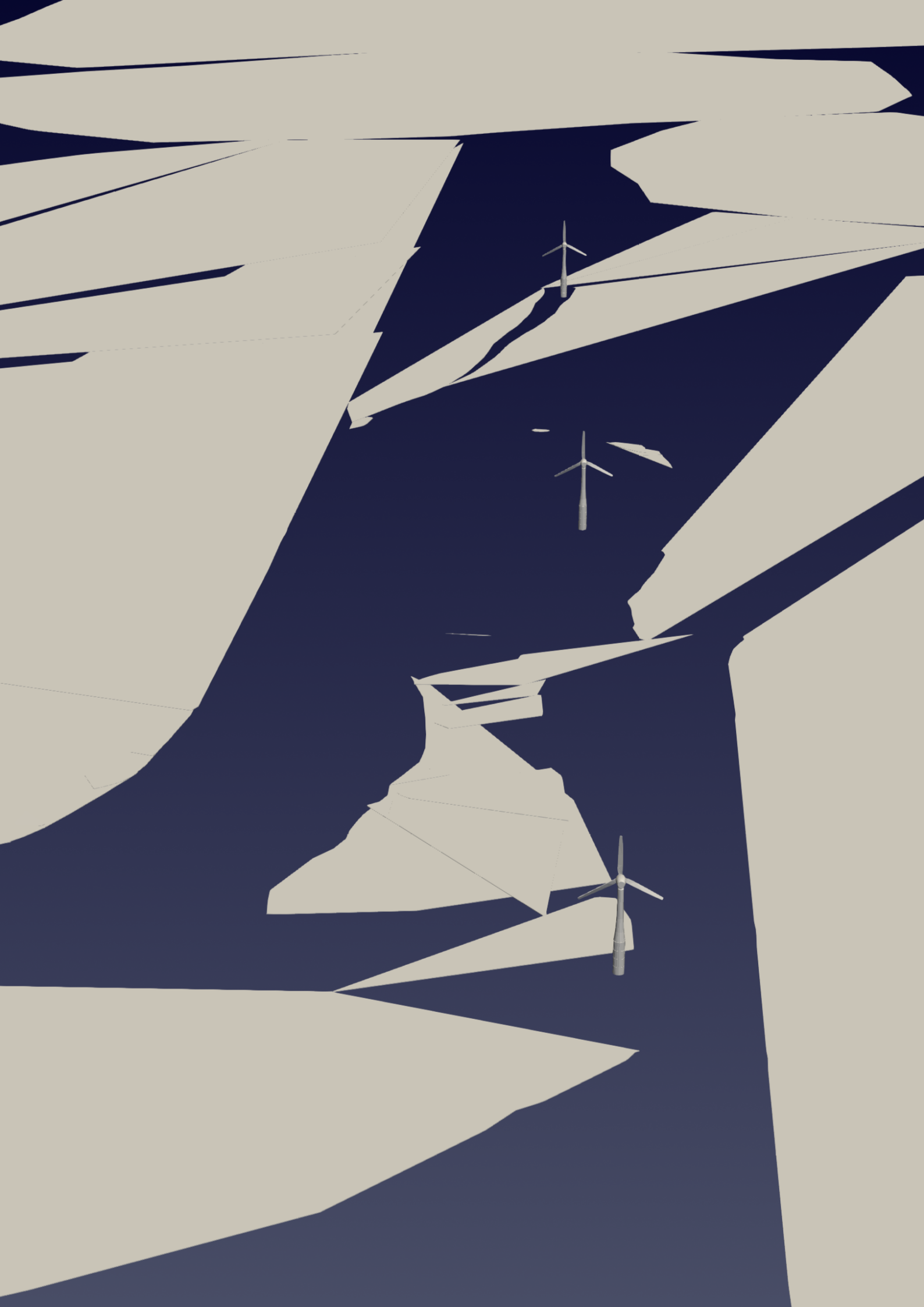

7
Results

This chapter presents the results from the simulations that have been performed in SIBIS as described in Chapter 6. First, the results are shown for the scenario in which the ice floes are initially positioned outside of the offshore wind farm. For this scenario, it is discussed how the presence of the OWF affects the ice drift speed. Several ice fields were selected with varying SIC and maximum floe size to simulate the diverse and dynamic nature of ice floe fields in reality. The influence of these varying parameters on the change in drift speed is explained in the next section, and will be treated further in the discussion. This scenario is displayed in Figure 7.1a to remind the reader of the context. Next, the grown-in scenario is treated, which is displayed in Figure 7.1b. It is examined what combinations of wind speed and ice thickness lead to the intimate contact condition. It is also discussed how the occurrence of the intimate contact condition is affected by the area of the stationary ice sheet and the number of grown in turbines. This effect will be further evaluated in the discussion.

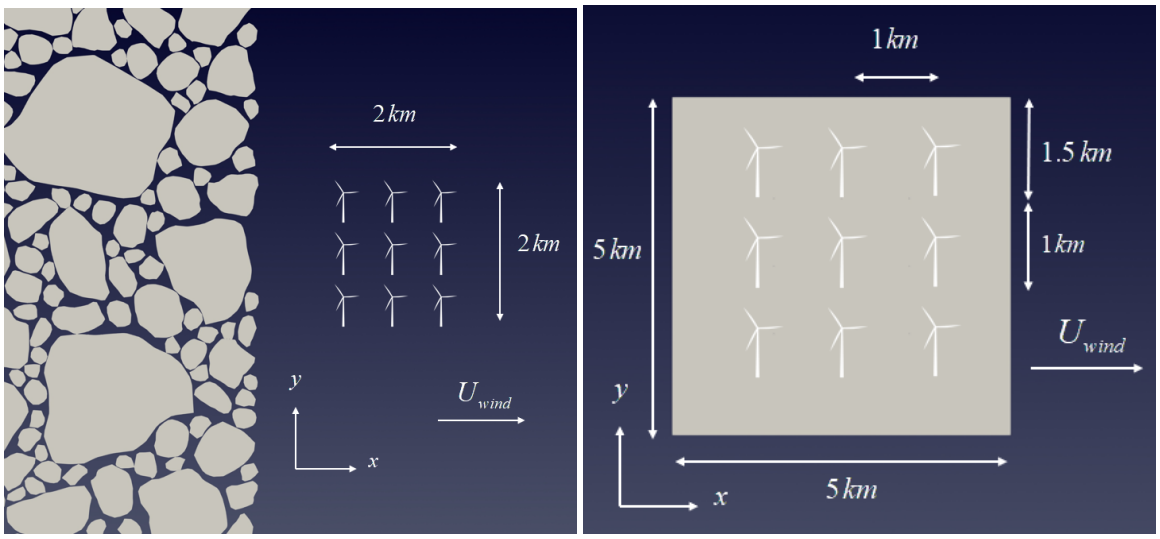

(a) Outside drift scenario **(b)** Grown-in scenario, only 3 x 3 layout shown here

Figure 7.1: Simulation scenarios that will be discussed in this chapter.

7.1. Outside Drift

7.1.1. Baseline Simulations

Figure 7.2 presents the ice drift velocity at the location of a single turbine within an ice field characterized by a sea ice concentration of 60% and floe radii ranging from 282 to 4850 meters. As formulated in the introduction, the assumption of a correlation between the wind speed and ice drift velocity - governed by a constant factor - may still hold for a single turbine. However, Figure 7.2 illustrates that the presence of a single structure leads to a reduction in ice drift speed. During the time intervals 6000 - 12000 s and 23000 - 25000 s, the turbine is in contact with ice. At all other times, no ice-structure interaction is observed. The correlation between the wind speed and the ice drift speed is lost during the ice-structure interaction, demonstrating that the assumption is incorrect for a single turbine.

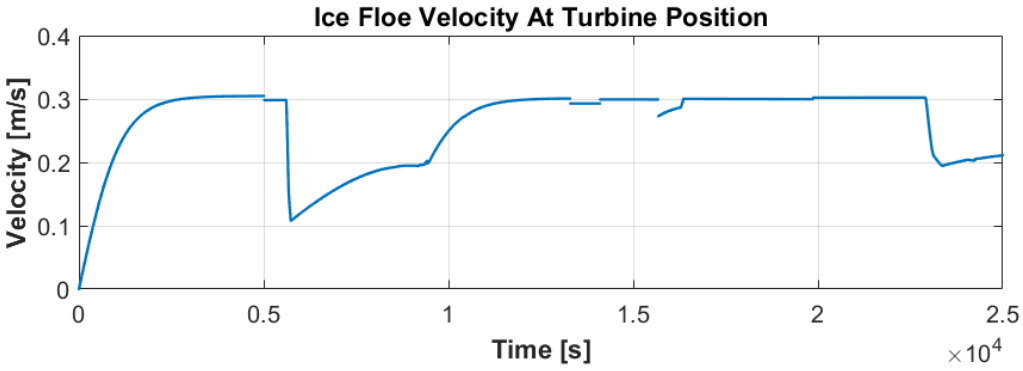

Figure 7.2: Time series of ice floe velocity at the turbine position for a floe field of SIC 60% and floe radii 282 - 4850 m.

In the following, the analysis is extended to configurations involving multiple structures. Figure 7.3 shows the results for the simulations with a 3 x 3 turbine layout, floe fields of 30 x 30 km, floe radii of 282 - 4850 m and sea ice concentrations of 60, 70 and 80%. The purpose of these simulations was to serve as a baseline as they cover the full range of floe sizes that are observed in the Southern Baltic Sea. The ice floes approach the wind farm having an average drift speed of 0.29 m/s. This average drift speed corresponds to the membrane limit, as expected. The average drift speed for the case without the OWF present is shown in gray. The average floe velocity in the presence of turbines is depicted by the other colours. When the first front of floes encounters the turbines, the average floe velocities start to decrease and they drop below the free-drift velocities. The dynamics of the floe field and the resulting ice-ice and ice-structure interaction is a highly stochastic process. Floe velocities and their direction are affected, among other factors, by floe shape, orientation and floe area of each individual floe as the floes move through the offshore wind farm. The decay of the average drift speed shown in Figure 7.3 is most pronounced for the SIC of 80%. For this particular floe field, the highest number of interactions between ice floes and turbines are observed. Therefore, this floe field will be further analysed in the following sections. It was found that the lowest floe speeds are recorded for the floes that are directly in contact with the turbines. Therefore, the floe velocities will first be analysed at the turbine positions.

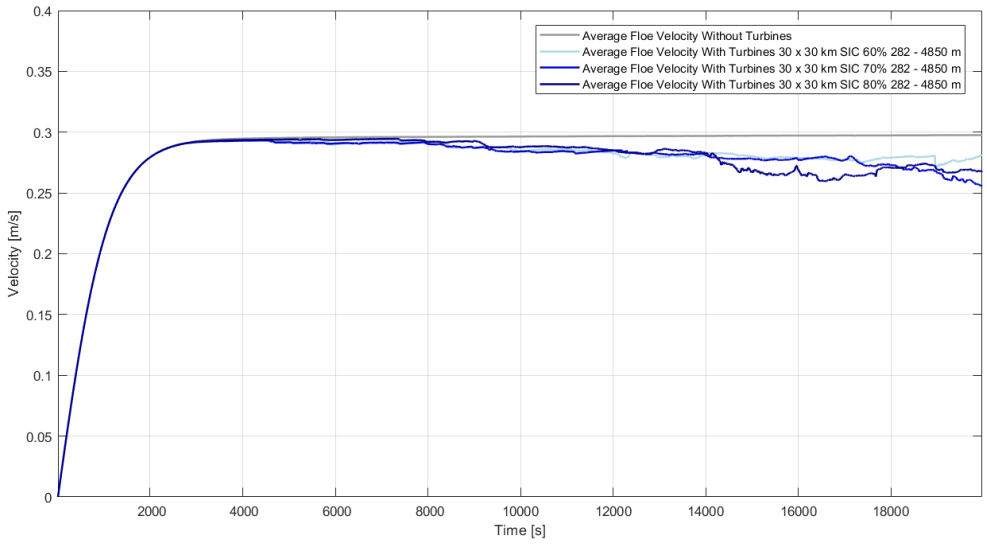

Figure 7.3: Comparison of the average floe velocities for baseline runs.

Ice Drift Speed Reduction at the Turbines

Now, the ice floe velocities at the turbine positions are considered for the floe field of 30 x 30 km, SIC 80% and floe radii of 282 - 4850 m. Figure 7.4 shows the distributions of floe velocities for the first-, second- and third row of turbines by combining the distribution for the individual turbines. Additionaly, the histogram for the floe field without the presence of the OWF is shown. Animations from the simulations show that the first row of turbines segments the ice floes into smaller pieces. This process is primarily dominated by splitting. Depending on the shape and orientation of the segmented floe, they may rotate and get stuck in the second- or third row of turbines. Figure 7.6 shows 2 time instants in which the rotation of floes results in low drift velocities at the second- and third row of turbines. Although near-zero velocities are observed less frequently for the third row of turbines as compared to the first- and second row in Figure 7.4, they can not be ruled out. This is further quantified by computing the average velocity over time at all isolated turbines, shown in the first row of Table 7.1. The velocity loss in the second row of Table 7.1 is computed by comparing the ice drift speed at the turbines to the average ice drift speed in simulations without turbines. Turbines 1, 2 and 3 are located inside row 1, with turbine 2 being the middle one. Turbines 4, 5, 6 are in row 2, and the remaining turbines are in row 3.

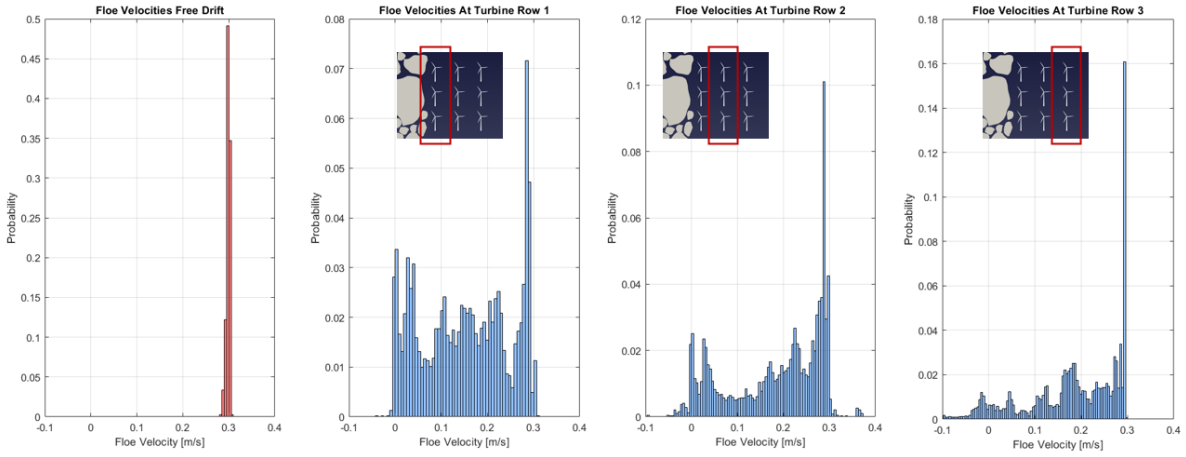

Figure 7.4: Histograms showing the probability of ice floe velocities occurring at the first-, second- and third row of turbines in the wind direction. Negative velocities are associated with ice floes drifting in the wind-opposing direction, caused by interaction among ice floes. The red histogram shows the ice floe velocities for the ice field without the presence of the OWF.

	Free Drift	Turbine 1	Turbine 2	Turbine 3	Turbine 4	Turbine 5	Turbine 6	Turbine 7	Turbine 8	Turbine 9
Velocity Ice	0.297	0.159	0.139	0.159	0.163	0.168	0.219	0.168	0.159	0.222
Velocity Reduction	0%	46.3%	52.9%	46.2%	45.2%	43.4%	26.1%	43.3%	46.3%	25.1%

Table 7.1: Average ice floe velocities at all turbines over time and the corresponding velocity reduction relative to the free drift situation. Turbines 1, 2, 3 are located in row 1, with number 2 being in the middle. Row 2 consists of turbines 4, 5, 6. The remaining turbines form the third row.

From Table 7.1 it can be concluded that there is a significant decay in the velocity of ice floes at the turbines. The reason that the distributions show a peak at 0.3 m/s is due to SIBIS tracking the velocity of the ice floe closest to a structure if there is no contact with ice. The highest velocity reduction of 52.9% is found for the middle turbine in the first row. The outer turbines in row 1 experience a velocity decay that is slightly lower. This can be explained by the fact that the ice floes can rotate around the outer turbines without encountering a neighbouring turbine. At turbine 6 and 9, the ice maintains a high velocity during ice-structure interaction. This results in the smallest velocity reduction among all the turbines. The reason that this was not observed at turbine 4 and 7 - which are the outer turbines at the opposing side of the OWF - is attributed to the rotation and consequential obstruction of a single floe at turbine 4 and 7. Thus, the initial position of the ice floe field affects the results. The average velocity reduction for row 1, 2 and 3 are respectively 48.5%, 38.2% and 38.2%. The difference across

the rows is primarily due to the low velocity reduction at turbine 6 and 9. From this simulation, it is thus not observed that the first row of turbines shields the rows behind it from interaction with the ice floes. This is mainly due to the rotation of floes inside the offshore wind farm after they have been split at the first row of turbines. It was observed that the turbines often act as rotation points, so that the ice floes rotate and consequently interact with a neighbouring turbine. Alternatively, the rotating ice floes may hit other ice, pushing the surrounding ice towards neighbouring turbines. Figure 7.4 shows that this may even lead to negative floe speeds at the turbines, corresponding to the wind-opposing direction. This occurs primarily at the secondary- and tertiary row. Figure 7.5 shows the histograms of ice velocities perpendicular to the wind direction. The floe speeds in this direction are all caused by the interaction and rotation of the floes when interacting with other ice floes or the turbines. Figure 7.5 demonstrates that this results in floe velocities with both positive and negative components not only in the wind-aligned direction but also in the direction perpendicular to the wind. Consequently, the turbines are subjected to multidirectional loading due to the ice drift. This highlights the potential occurrence of directional misalignment between ice drift forces and wind-induced loads under these conditions. It is shown that ice drift speeds up to 0.2 m/s may occur in the direction perpendicular to the wind. Furthermore, the observed floe speeds in this direction are in the velocity range to lead to ice-induced vibrations.

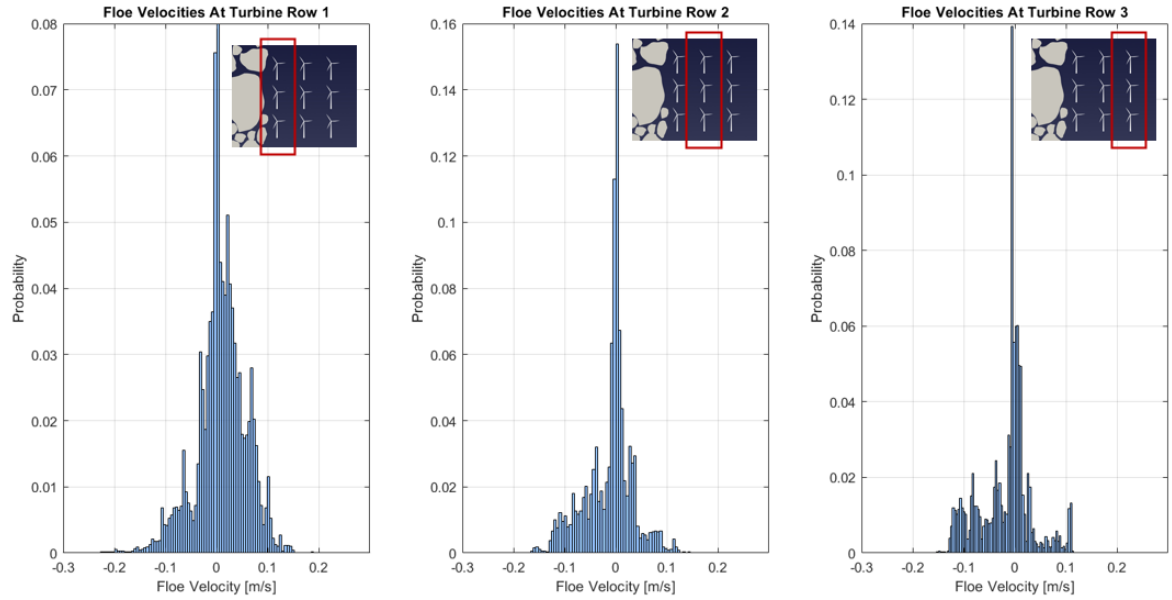

Figure 7.5: Histograms showing the probability of ice floe velocities occurring at the first-, second- and third row of turbines for floe speeds perpendicular to the wind direction.

The rotation of ice floes - caused by ice-ice and ice-structure interaction - inside the OWF can thus lead to a misalignment of the wind- and ice drift speed direction. Hammer et al. (2023) showed that if the wind- and ice drift direction are misaligned, ice-induced vibrations can develop up to higher ice drift speeds as compared to an aligned scenario.

Thus, floes that are indirectly in contact with the turbines - by interacting with an ice floe that is in direct contact - may affect the ice drift speed at the turbines. **This implies that the analysis of the drift speed of ice floes at the turbines should account for both the ice floes in direct- and indirect contact with the structures.**

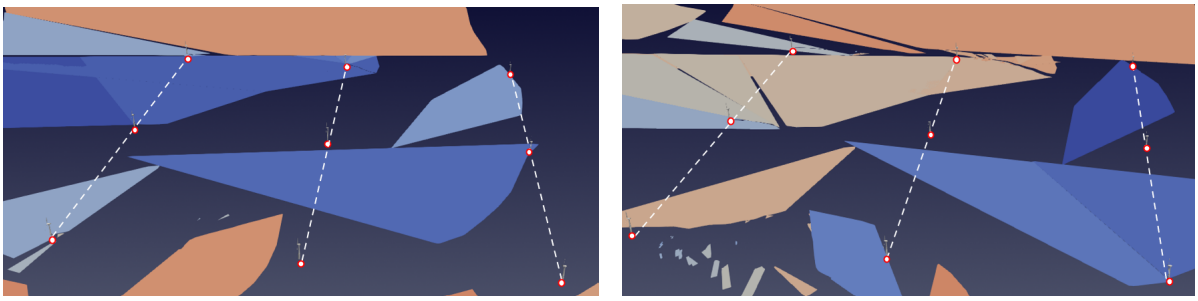

(a) At 14400 seconds a floe is blocked by the second- and third row of turbines.

(b) At 17400 the floe has moved through the wind farm and is now again stuck at the third row of turbines.

Figure 7.6: Time instants when the second- and third row of turbines encounter a floe at low velocity due to rotation. The turbine positions are depicted by the red markers, the turbine rows are indicated by the dashed lines. Blue colours refer to low drift speeds, while the orange colours depict high drift speed (scaled in a range of 0 - 0.4 m/s).

To further investigate the interactions among ice floes, the histograms of the ice floe field velocities with- and without the presence of the offshore wind farm are considered. This is visualized in Figure 7.8 for the floe field of 30 x 30 km, SIC 80% and floe radii of 282 - 4850 m at discrete time steps. Both the probability density function (PDF) and the cumulative distribution function (CDF) are plotted. Table 7.2 presents the average velocities for the ice floes with- and without the presence of turbines, denoted by the parameter μ. The standard deviation σ is also included in the table. The results without turbines present indicate that the ice drift speed is roughly stationary in this case, as μ and σ vary minimally over time. It can be seen that the presence of the turbines leads to a velocity loss and lowers the average floe-velocity. Furthermore, the turbines skew the distribution towards low velocities, increasing σ. In order to further quantify the velocity loss of the ice floes, the 5th percentile ($Q_{0.05}$) of the ice floe velocities is also computed. As this parameter investigates the outliers, it filters out most of the floes that are not in direct- or indirect contact with the turbines. It is observed that there is a significant decay in the 5th percentile drift speed due to the presence of the turbines. This can physically be explained by looking at what is happening inside the ice floe field throughout the simulation.

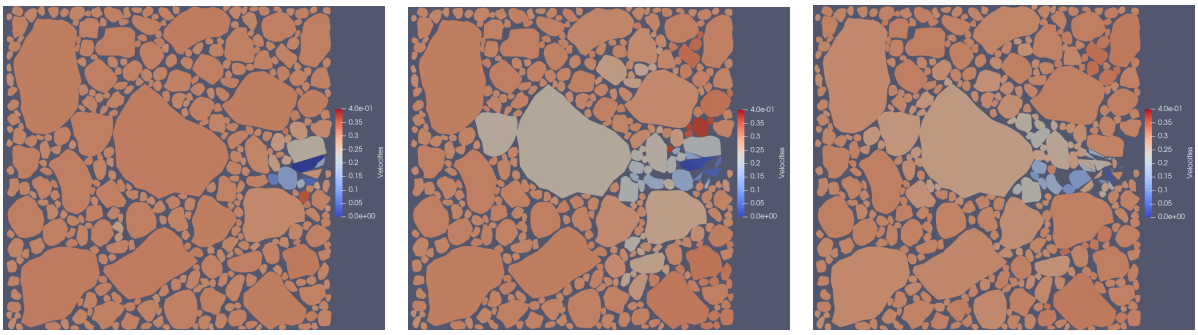

(a) t = 10000 seconds

(b) t = 15000 seconds

(c) t = 20000 seconds

Figure 7.7: Top view floe field 30 x 30 km , SIC 80% and floe radii of 282 - 4850 m. The image dimensions span approximately 30 x 30 km.

In Figure 7.7a and Figure 7.8a, it can be seen that the blocking of a single floe causes the floe field behind it to decelerate. An increasing number of floes stagnates behind it over time, resulting in a probability density function (PDF) that skews towards low velocities at t = 15000 seconds, shown in Figure 7.8c. Figure 7.8c reveals that at t = 15000 seconds, blocking of the floe front causes multiple floes to have velocities near zero, resulting in a very long tail of the cumulative distribution function (CDF) shown in Figure 7.8d. This can also be observed by a very low 5th percentile of the floe velocities that are listed in Table 7.2 at t = 15000 seconds. The built up pressure from the floe field results in a combination of crushing and splitting and subsequently acceleration of the floe field front. This can be seen in Figure 7.8e, as the majority of the near-zero velocities shift towards a speed of 0.1 - 0.2 m/s. At all timesteps, the lowest floe velocities occur for floes that are directly in contact with the turbines. Ice

floes in direct contact with the structures will reduce significantly in speed or stop. **From the histograms in Figure 7.4 and the histograms in Figure 7.8, it is found that these floe speeds are in the critical range where intermittent crushing and frequency lock-in may occur**. This example shows that the correlation between the wind speed and the ice drift speed is lost and low drift speeds may occur for the given wind speed. The resulting multi-modal interaction may lead to ice-induced vibrations and consequentially severe loads on the turbines (Hammer et al., 2022).

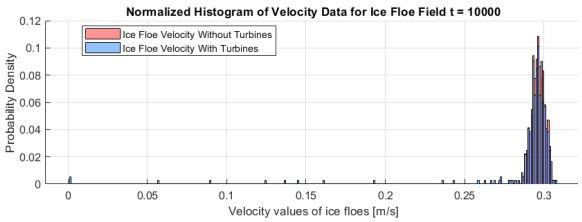

(a) t = 10000 seconds

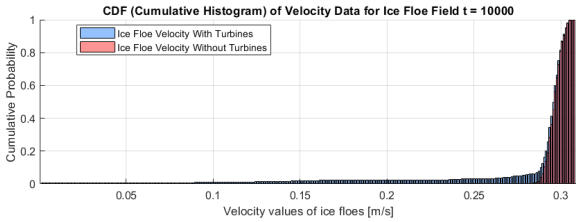

(b) t = 10000 seconds

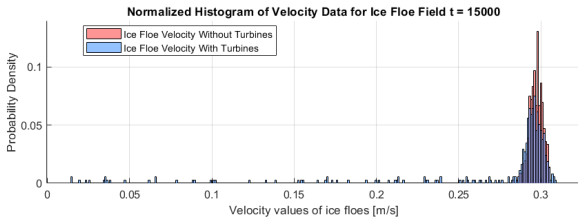

(c) t = 15000 seconds

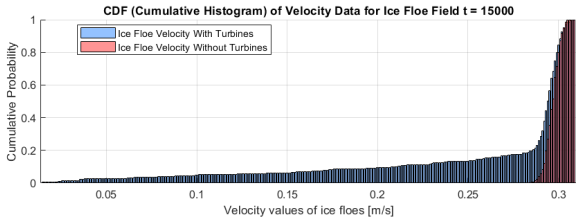

(d) t = 15000 seconds

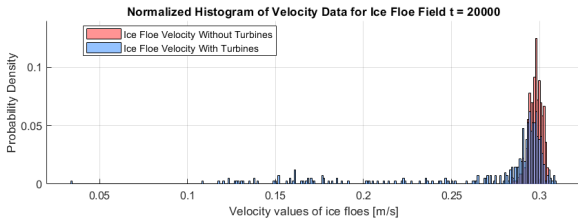

(e) t = 20000 seconds

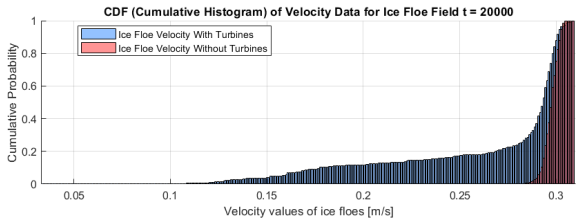

(f) t = 20000 seconds

Figure 7.8: Histograms comparing floe velocities with and without the presence of turbines for a floe field of 30 × 30 km, SIC 80%, and floe radii of 282–4850 m. Both the probability density function (PDF) and cumulative distribution function (CDF) are plotted.

	t = 10000 seconds	**15000 seconds**	**t = 20000 seconds**
Free Drift Scenario [m/s]	μ = 0.296	μ = 0.297	μ = 0.297
	σ = 0.004	σ = 0.004	σ = 0.004
	$Q_{0.05}$ = 0.289	$Q_{0.05}$ = 0.290	$Q_{0.05}$ = 0.291
	$Q_{0.01}$ = 0.286	$Q_{0.01}$ = 0.288	$Q_{0.01}$ = 0.286
With Turbines [m/s]	μ = 0.290	μ = 0.273	μ = 0.273
	σ = 0.033	σ = 0.061	σ = 0.048
	$Q_{0.05}$ = 0.277	$Q_{0.05}$ = 0.101	$Q_{0.05}$ = 0.157
	$Q_{0.01}$ = 0.095	$Q_{0.01}$ = 0.024	$Q_{0.01}$ = 0.122

Table 7.2: Average ice floe velocity for the floes that are both in contact and not in contact with the turbines. The listed values correspond to the 30 x 30 km ice field with SIC 80% and floe radii 282 - 4850 m.

To further distinguish between the free-drift scenario and the ice drift with the turbines present, the 1st percentiles are also computed in Table 7.2. These will give more insight into the tail of the cumulative distributions shown in Figure 7.8. As all 1st percentiles for floe velocities in the presence of the offshore wind farm that are listed in Table 7.2 are well below the free drift 1st percentile, it can be assumed that these floes are in direct- or indirect contact with the turbines. Now, Table 7.3 displays the velocity reduction due to the presence of the turbines by computing the ratio between 1st percentile of the free-drift scenario $Q_{0.01,freedrift}$ and the 1st percentile in the scenario with turbines $Q_{0.01,turbines}$. The 30 x 30 km SIC 80% 282 - 4850 m floe field consists of roughly 300 ice floes. Therefore, the 1st percentile marks the highest velocity observed among the three most slow-moving floes. In addition, the minimum velocity (u_{min}) of all ice floes and the corresponding velocity reduction are also computed and listed in Table 7.3 for multiple time instants. From Table 7.3 it can now be observed that there is a significant velocity loss due to the presence of the turbines at all timesteps, for both the $Q_{0.01}$ and u_{min}. The average velocity reductions for $Q_{0.01}$ and u_{min} are respectively 65.29% and 87.54%.

Time [s]	10000	11000	12000	13000	14000	15000	16000	17000	18000	19000	20000
$\frac{Q_{0.01,\text{turbines}}}{Q_{0.01,\text{freedrift}}}$	33.1%	33.7%	29.9%	37.1%	36.8%	8.4%	34.9%	40.9%	40.4%	43.9%	42.7%
Velocity Reduction	66.9%	66.3%	70.1%	62.9%	63.2%	91.6%	65.2%	59.1%	59.6%	56.0%	57.3%
$\frac{u_{min,\text{turbines}}}{u_{min,\text{freedrift}}}$	0.3%	2.8%	16.2%	16.6%	10.3%	4.9%	11.7%	9.9%	14.6%	37.9%	11.8%
Velocity Reduction	99.7%	97.2%	83.8%	83.4%	89.7%	95.1%	88.3%	90.1%	85.4%	62.1%	88.2%

Table 7.3: Ratio between the 1st percentile- and minimum ice floe velocities with- and without turbines for different time steps. The 1st percentile- and minimum velocities can be assumed to be in direct/indirect contact with the turbines. It is therefore shown that the presence of the turbines leads to a significant velocity loss compared to the free drift situation. The values are based on the 30 x 30 km ice field with SIC 80% and floe radii 282 - 4850 m.

As soon as the first front of floes has encountered the offshore wind farm, the reduction of floe velocities radiates from the position of the turbines in a wind opposing-direction, propagating the speed reduction through the floe field. The compact floe field that is created in front of the wind farm pushes the first front of floes through the wind farm. This initiates splitting or crushing of the floes in contact with turbines when sufficient pressure has built up. In the next section, the effect of the presence of the turbines on the global ice field will therefore be treated.

Spatial Distribution Of Ice Drift Speed Reduction Across the Floe Field

A next step that may be taken is to consider what fraction of the total floe field is affected by the presence of the OWF. This is relevant as it represents the part of the floe field that is either in direct or indirect contact with the structures, and thus represents the part of the ice field that exerts a force onto the turbines. This part of the floe field is extracted as follows:

- Figure 7.9 is created by comparing the drift speeds for all floes for the case with- and without the wind farm. At each timestep, the lowest observed ice floe speed without an OWF is computed. If the ice floe speeds in the simulation with the OWF are below this threshold, they must be affected by the structures. It is then assumed that these floes are either in direct- or indirect contact with the structures. The data is then filtered using this threshold.
- The data is then normalized by the number of floes and corrected for the fact that the number of floes increases over time due to crushing and splitting.
- It should be noted that the data displayed in Figure 7.9 does not tell anything about the spatial extent of the speed reduction. The floe field dimensions and the number of floes vary across the simulations. Therefore, it should only be interpreted in relation to the floe field dimensions and the number of floes for the corresponding ice floe field.

Figure 7.9 shows that as time progresses, an increasing amount of floes is reduced in speed due to the structures. Figure 7.7 shows that this speed reduction radiates mainly in the wind-opposing direction,

although some moderate lateral speed reduction is observed. At 10000 seconds, the speed reduction only travels 4.5 km into the floe field, as seen in Figure 7.7a. This distance is measured from the first row of turbines. Figure 7.7b shows that after 15000 seconds, a large floe that is positioned in the middle of the field reduces in speed and radiates the speed reduction far into the floe field. The speed is then reduced in wind-opposing direction over a distance of $\approx$ 21 km. From Figure 7.7c it is observed the speed reduction has propagated over a distance of $\approx$ 25 km in the wind-opposing direction after 20000 seconds. Figure 7.9 shows that after 20000 seconds, around 30% of the floe field is reduced in speed due to the presence of the OWF for a SIC of 80%. When comparing the simulations in Figure 7.9, it can be seen that a higher SIC leads to a larger proportion of the floe field that 'feels' the OWF. This was expected, as Heorton et al. (2019) stated that a high sea ice concentration allows sufficient collision between ice floes, so that internal stresses can be transmitted over distances greater than the floe width. Likewise, the presence of a single large floe has the same effect. Furthermore, the speed reduction travels more quickly through the wind farm for a high SIC, as the floes are positioned closer to each other.

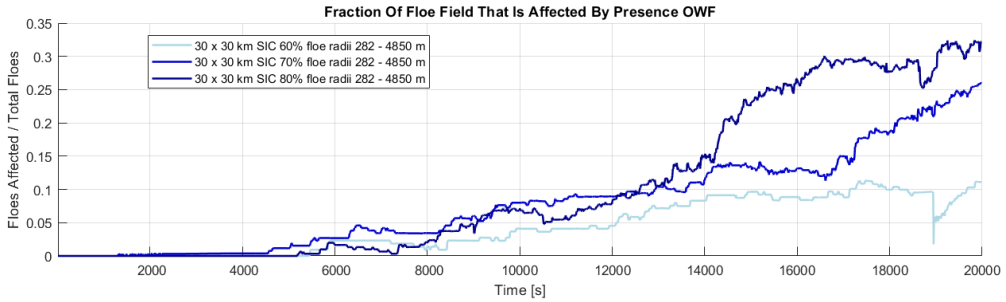

Figure 7.9: Fraction of the ice floe field in the baseline simulations that is affected by the presence of the turbines.

Figure 7.10 shows the velocity distribution for ice floes that are in direct- or indirect contact with turbines in blue for a SIC of 80% and floe radii of 282 - 4850 m. In addition, the floe speeds of floes that are not in contact with turbines are shown. **Clearly, the presence of the turbines lowers the ice drift speed. The lowest ice floe velocities are for the ones that are in direct contact with the turbines, as confirmed by the velocity histograms in Figure 7.4.**

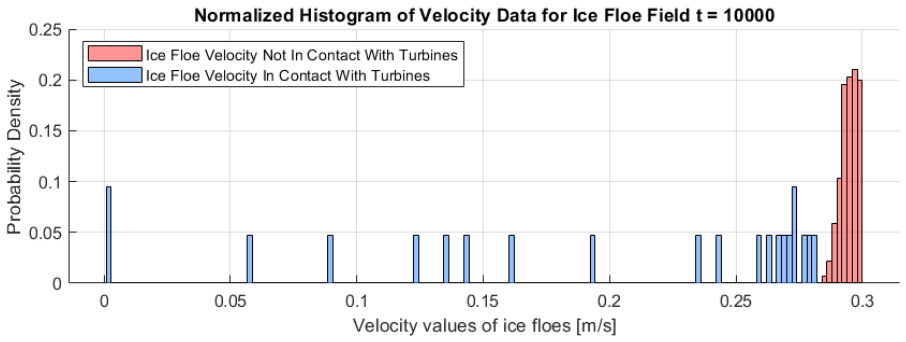

(a) t = 10000 seconds

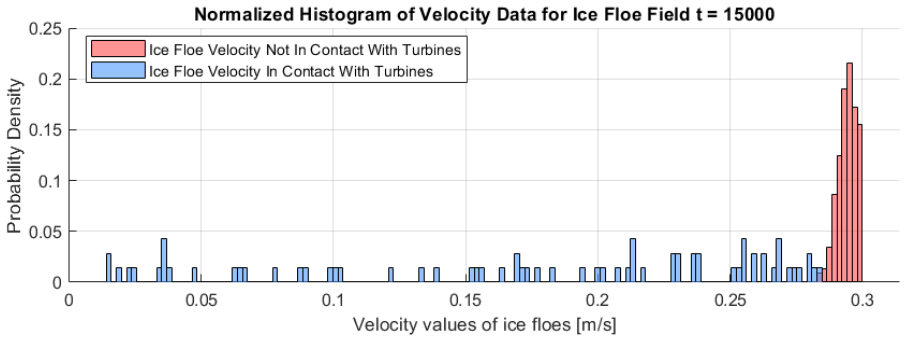

(b) t = 15000 seconds

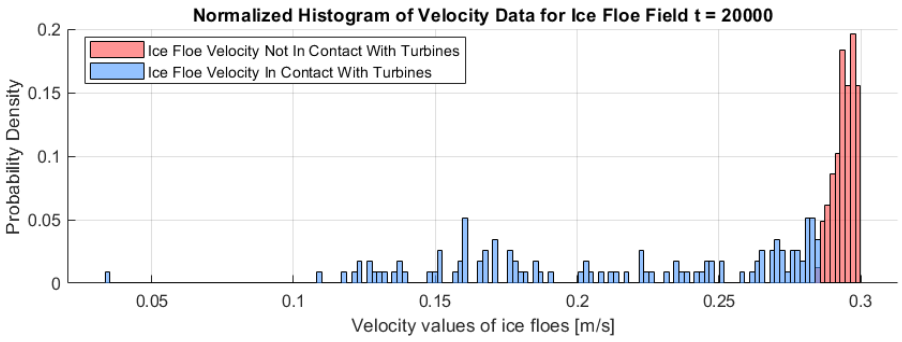

(c) t = 20000 seconds

Figure 7.10: Histograms comparing the floe velocities of ice floes that are in direct/indirect contact with turbines, compared to those uninfluenced by the presence of the OWF.

7.1.2. Influence Maximum Floe Size

In addition to the baseline runs having floe radii of 282 - 4850 m, multiple runs were carried out using a lower maximum floe size of 80 - 1000 m. Figure 7.11 shows the fraction of the floe field that is reduced in speed by the presence of the turbines for floe radii of 80 - 1000 m. It is evident that by lowering the maximum floe size, the propagation of the speed reduction throughout the floe field is very different compared to a floe radius range of 282 - 4850 m (shown in Figure 7.9). Where floe radii up to 4850 m in the baseline simulations show a continuously increasing trend as in Figure 7.9, Figure 7.11 shows an oscillating pattern for floe radii of 80 - 1000 m. This trend is especially pronounced for the floe field having a SIC of 80% and floe radii of 80 - 1000 m. Figure 7.12 captures the ice floe velocities for this specific floe field after 8000, 12000 and 13770 seconds. Figure 7.12a shows that at 8000 seconds, ice-structure contact with multiple large floes results in stagnation of the floe field. At 12000 seconds, these floes have either rotated or have been split. This means that the floe field has accelerated again. At 13770 seconds, the highest peak is observed as 11% of the floe field is affected. The turbines encounter large floes again and the ice must either be split or rotated to accelerate. **The**

continuous acceleration and deceleration of the floe field leads to an oscillation that is caused by a combination of crushing, splitting and rotation at the ice-structure interface related to the floe size. Furthermore, the ice in the wind-opposing direction rotates around the piled-up part of the floe field and drifts around it. This also partly explains the acceleration. For sea ice concentrations of 60% and 70%, the floes can more easily pass the turbines as there is more space for rotation. Therefore, the speed reduction develops more slowly throughout the floe field and a smaller fraction of the floe field is affected by the structures. For the timesteps of 8000, 12000 and 13770 seconds, the speed reduction travels a distance of 8 km, 6 km and 12 km respectively in the wind-opposing direction. This distance is measured from the first row of turbines.

The difference between the continuously increasing trend shown in Figure 7.9 and the oscillating pattern in Figure 7.11 can be accounted to two main mechanisms:

1. When floes of 282 - 4850 m encounter the turbines, the ice needs to be split into more segments compared to a floe of 80 - 1000 m in order to pass in between the turbines. For a floe field with floe radii of 80 - 1000 m, a single split of a floe that is obstructed at the turbines can already ensure that the ice floe can pass the turbines and resume the movement of the accumulated floes in the wind-opposing direction. For much larger floe radii, the floes need to be split multiple times, which takes longer. As the splitting of the floes that are in direct contact with the turbines takes longer, a larger fraction of the ice field stagnates behind it.
2. Secondly, the largest floes in the 282 - 4850 m field have a significant effect on the propagation of speed reduction. When an ice floe with a diameter of for example 6 km experiences a deceleration, the resulting reduction in velocity propagates across the entire floe, i.e. over a distance of 6 km within a single time step. This reflects the assumption that the floe behaves as a rigid body, transferring mechanical energy in a single timestep. This is in accordance with physical expectations. This effect is amplified by the fact that these very large floes are surrounded by a high number of other floes, which will all be affected once the large floe slows down. **The presence of these very large floes also explains why the spatial extent of the speed reduction is much larger for floe radii of 282 - 4850 m as compared to floe radii of 80 - 1000 m**.

From visual analysis of animations of the simulations, it was confirmed that all the peaks and troughs that are present for a SIC of 80% in Figure 7.11 are caused by the respective stagnation and splitting of the largest floes with a radius close to 1000 m. The animation for the floe field of SIC 80% and floe radii of 282 - 4850 m showed that the significant increase that is observed in Figure 7.9 between 14000- and 15000 seconds is due to the deceleration of the very large floe that is positioned in the middle of the ice field (this floe can be seen in Figure 7.7b and has an approximate radius of 4850 m). **The fraction of the ice field that is affected by the presence of the turbines is thus dominated by the presence of very large floes.** As the average floe size increases, this fraction also grows. For ice floe fields characterized by lower sea ice concentrations, the ice drift behaviour is different. As the ice floes approaching from the wind opposing direction encounter the obstructed floe field, the increased spacing in between the floes allows the ice to rotate around the obstructed floes and they are deflected laterally, drifting around the OWF. **For lower sea ice concentrations, there is thus less accumulation behind obstructed floes, since there is more space for redistribution and the ice floes can find a way around the OWF. Therefore, the oscillating pattern is less pronounced**. The reduced confinement also explains why for lower sea ice concentrations, the spatial extent of the speed reduction is lower as compared to high concentrations.

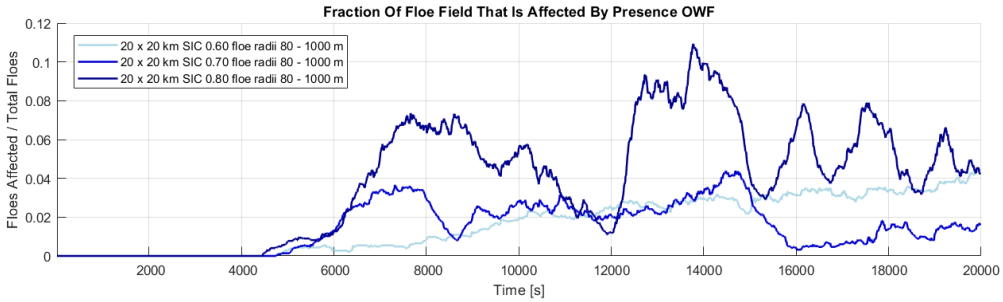

Figure 7.11: Fraction of the ice floe field that is affected by the presence of the turbines for a floe field of 20 x 20 km, floe radii of 80 - 1000 m and varying SIC.

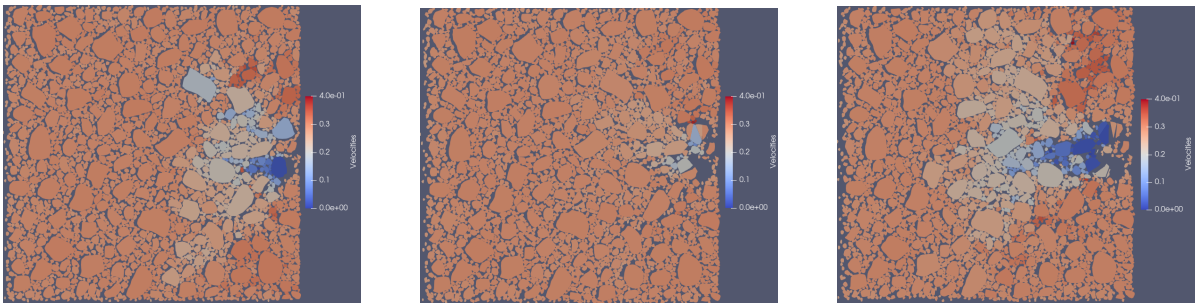

(a) Top view of the floe field for a SIC of 80% and a floe radius of 80 - 1000 m after 8000 seconds of simulated time.

(b) Top view of the floe field for a SIC of 80% and a floe radius of 80 - 1000 m after 12000 seconds of simulated time.

(c) Top view of the floe field for a SIC of 80% and a floe radius of 80 - 1000 m after 13770 seconds of simulated time.

Figure 7.12: Top view of ice floe velocities.

In addition, Figure 7.13 shows the results for a floe field of 12 x 12 km, floe radii of 80 - 300 m and a SIC of 60%. Unfortunately, the floe field generator does not converge towards a SIC of 70% and 80% for this narrow range of floe radius. At timesteps of 8000, 12000 and 13770 seconds, the speed reduction travels respectively 2 km, 2.8 km and 2.9 km, measured from the first row of turbines. Thus, small floe sizes limit the spatial extent of the speed reduction. This is in line with expectation, as it was previously seen that as maximum floe size increases, the speed reduction travels further into the floe field.

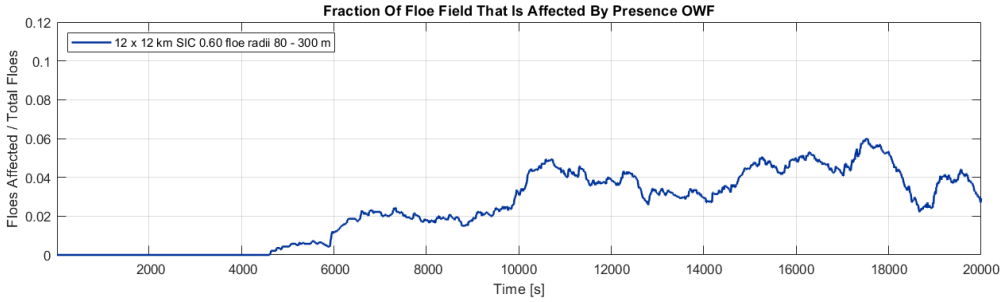

Figure 7.13: Fraction of the ice floe field that is affected by the presence of the turbines for a floe field of 12 x 12 km, floe radii of 80 - 300 m and a SIC of 60%.

7.2. Grown In

7.2.1. Critical Combinations of Wind Speed and Ice Thickness

The first simulations that were performed for the grown-in condition are a 3 x 3 and 4 x 4 turbine layout, having an area of the stationary ice sheet of respectively 25 km^2 and 36 km^2. The buffer distance in between the turbines and the surrounding ice is set to 0.10 m. The wind drag force in SIBIS is computed

as in equation 7.1 (Rabatel, 2025):

$$F_{\text{drag}} = \frac{1}{2}\rho_a \|\vec{u} - \vec{v}\| (\vec{u} - \vec{v}) CA \tag{7.1}$$

The body velocity of the ice is denoted by $\vec{v}$ and $\vec{u}$ is the fluid velocity. C is the drag coefficient that is separated into the form- and skin-drag. A is the cross-sectional area for the computation of form drag, or the longitudinal floe area for the skin drag. The wind drag force must equal the crushing force to initiate crushing of the turbines. The crushing force as described by equation 3.2 can be interpreted as the resistance from the turbines. This leads to the following expression:

$$u_c = \sqrt{\frac{N_{turbines} \cdot 2 \cdot \mathcal{L}_{cr}}{\rho_a \cdot C \cdot A}} \tag{7.2}$$

In which $N_{turbines}$ is the number of turbines that is frozen in. The results from the simulations for the 3 x 3 and 4 x 4 turbine layout can now be compared to the analytical expression in equation 7.2. The blue area in Figure 7.14 represents the combinations of wind speed and ice thickness for which the resistance of the turbines exceeds the external forcing from the wind. In this part of the graph, the grown-in ice sheet is not expected to (re)-initiate movement. Above the black line, the wind forcing becomes sufficient to promote an intimate contact condition. This regime is displayed by the red area. The blue line displays the analytical solution. Figure 7.14 demonstrates that a deviation is found between the simulations and the analytical solution. This is due to the accuracy of the wind speed that was retrieved from the simulations, as only a limited amount was performed. For several combinations of ice thickness and wind speed, crushing is observed. The full-thickness crushing and simultaneous loading of all turbines at low relative velocities leads to severe ice induced vibrations in this case (Hammer et al., 2023).

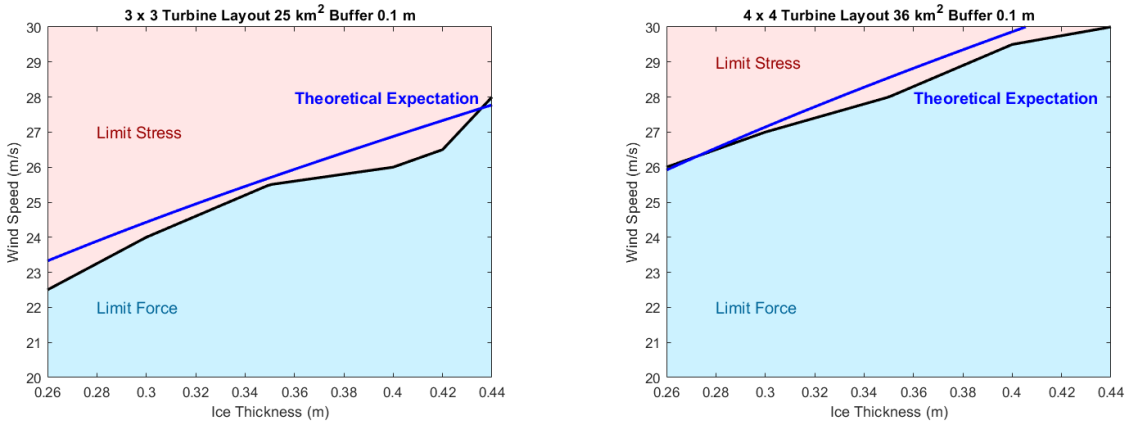

(a) 3 x 3 turbine configuration

(b) 4 x 4 turbine configuration

Figure 7.14: Critical wind speeds in combination with multiple ice thicknesses that lead to crushing of the grown-in ice sheet.

The movement of the stationary ice sheet and the resulting forces on the structures may be further analysed by examining two scenarios for a 3 x 3 layout, an ice area of 25 km^2, an ice thickness of 0.44 m and several wind speeds. Figure 7.15 shows the ice floe velocity and structural loads on a single turbine for a wind speed of 28 m/s and 21 m/s, corresponding to limit stress and limit force conditions respectively. Limit stress is the process that occurs when there is sufficient driving force from the wind to envelop the structure and generate ice actions across the full width of the structure. Limit force occurs when the driving force from the wind is insufficient to fully envelop the structure. For a wind speed of 28 m/s, the ice floe velocity is increasing and leads to a crushing force of 2 MN for a single turbine. For a wind speed of 21 m/s, the ice velocity initially increases due to the distance in between the turbines and surrounding ice of 0.10 m. Then, the velocity drops to zero, but the force remains constant at 1.25 MN over time. Thus, the limit stress scenario leads to the highest forces on the structure. This occurs if there is sufficient wind force to generate ice actions across the total width of the structure. A wind

speed of 28 m/s results in contact across the entire width of 7.51 m. For a wind speed of 21 m/s, the wind force is insufficient to fully envelop the structure, as the contact width only develops up to 7.03 m. Therefore, contact over the full width does not occur and the resulting force is lower.

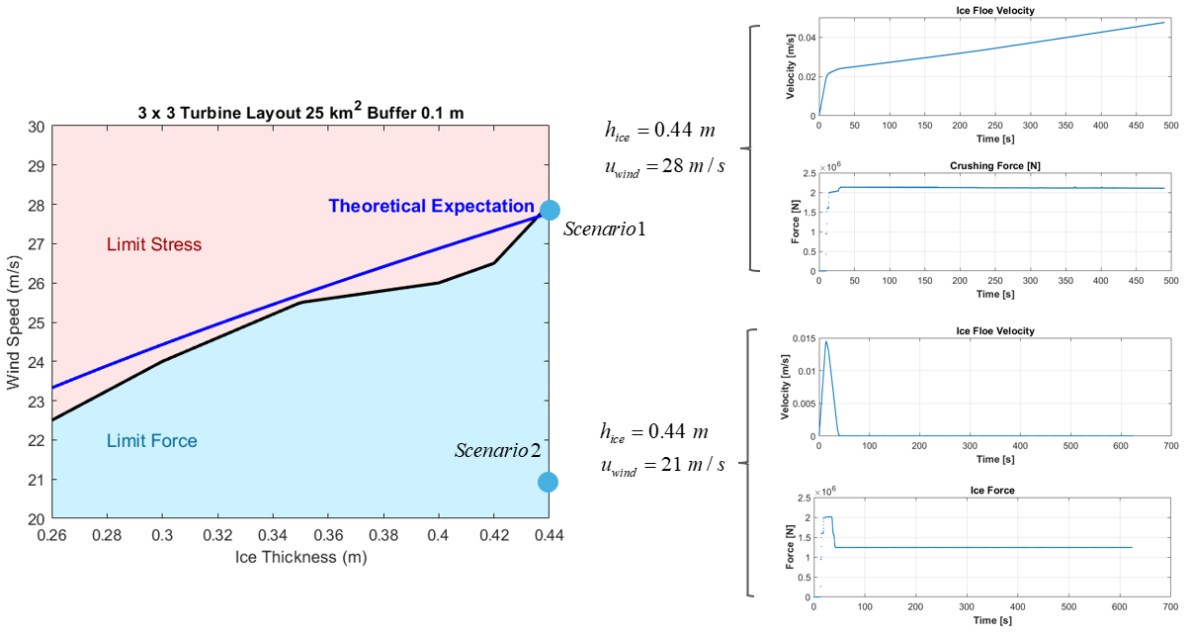

Figure 7.15: Simulations to address the effect of ice area and number of grown in turbines. The ice floe velocity and the ice loads that are shown are corresponding to a single turbine.

Figure 7.14 shows that the critical wind speed needed to (re)-initiate movement of the stationary ice sheet for the 4 x 4 layout is considerably higher than the 3 x 3 layout. In the next part it will be explained what causes the difference in critical wind speed for these two layouts.

7.2.2. Varying the Number of Grown-In Turbines and the Area of the Ice Sheet

The turbines provide resistance against the motion of the ice sheet while the ice area governs the driving force from the wind. For the 3 x 3 turbine layout with an ice sheet area of 25 km^2, this ratio is equal to 9/25 = 0.36. To verify if the critical wind speed can be predicted by this ratio, another simulation was performed with the same ratio. This leads to a 4 x 4 turbine layout with an ice area of 44.44 km^2. The distance in between the turbines is 1 km and the distance from the outer turbines to the open water is 1833.5 m. What follows from equation 7.2 is that the critical wind speed for these two simulations should be equal:

$$\frac{u_{c1}}{u_{c2}} = \frac{\sqrt{\frac{N_{\text{turbines}_{3\times3}} \cdot 2 \cdot \mathcal{L}_{cr}}{\rho_a \cdot C \cdot A_1}}}{\sqrt{\frac{N_{\text{turbines}_{4\times4}} \cdot 2 \cdot \mathcal{L}_{cr}}{\rho_a \cdot C \cdot A_2}}}$$

For both simulations, the full-width crushing force is equal to 2 MN. As the longitudinal floe area is much larger than the cross-sectional area, A is equal to 25 km^2 and 44.44 km^2 and the drag coefficient is set to the skin drag coefficient of 0.002. This simplifies the expression to:

$$\frac{u_{c1}}{u_{c2}} = \frac{\sqrt{\frac{9 \cdot 2 \cdot 2 \cdot 10^6}{1 \cdot 0.002 \cdot 25 \cdot 10^6}}}{\sqrt{\frac{16 \cdot 2 \cdot 2 \cdot 10^6}{1 \cdot 0.002 \cdot 44.44 \cdot 10^6}}} = 1$$

To verify if the presented analytical solution is correct for this number of turbines and ice sheet area, the simulations have been performed in SIBIS. The results are shown in Figure 7.16.

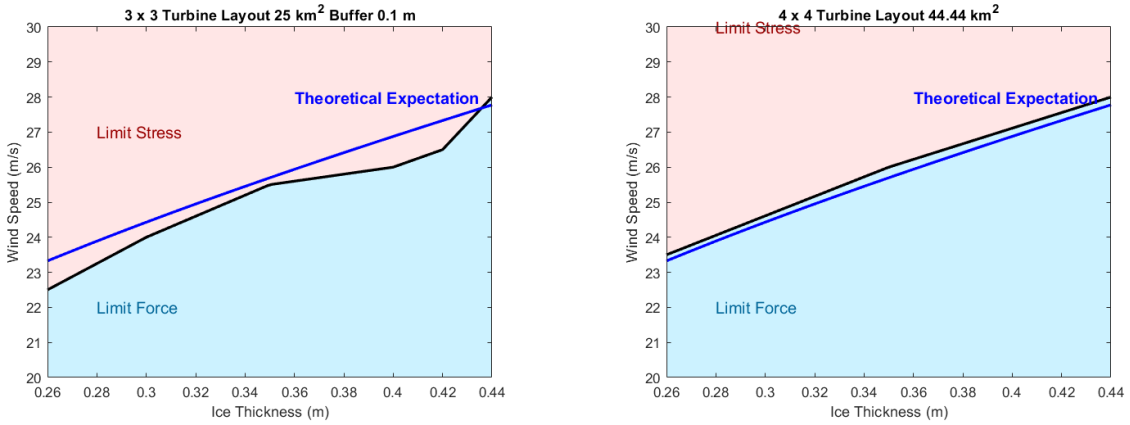

(a) 3 x 3 - 25 km^2 configuration

(b) 4 x 4 - 44.44 km^2 configuration

Figure 7.16: Comparison of the critical wind speed needed to (re)-initiate motion of the stationary ice sheet for two simulations having the same ratio of the number of turbines relative to the ice area.

Comparing Figure 7.16a to Figure 7.16b, it is observed that the critical wind speed is indeed equal, although some deviations from the theoretical expectation occur for the 3 x 3 - 25 km^2 simulation that are due to the number of performed simulations and numerical errors that may occur.

7.2.3. Extrapolation to the Baltic Eagle Offshore Wind Farm layout

Based upon equation 7.2 a prediction can be made for the critical wind speeds for larger offshore wind farms. In this section, the Baltic Eagle wind farm will be used as an example to demonstrate the expected results for large-scale wind farms that consist of a high number of turbines. The Baltic Eagle consists of 50 turbines that span a total area of approximately 8 x 8 km, as can be seen in Figure 7.17a The distance from the outer turbines to the edge of the ice sheet is again assumed to be 1500 m. This results in a 10 x 11 km ice sheet that covers the wind farm in grown-in conditions. Figure 7.17b is obtained by implementing these values into equation 7.2.

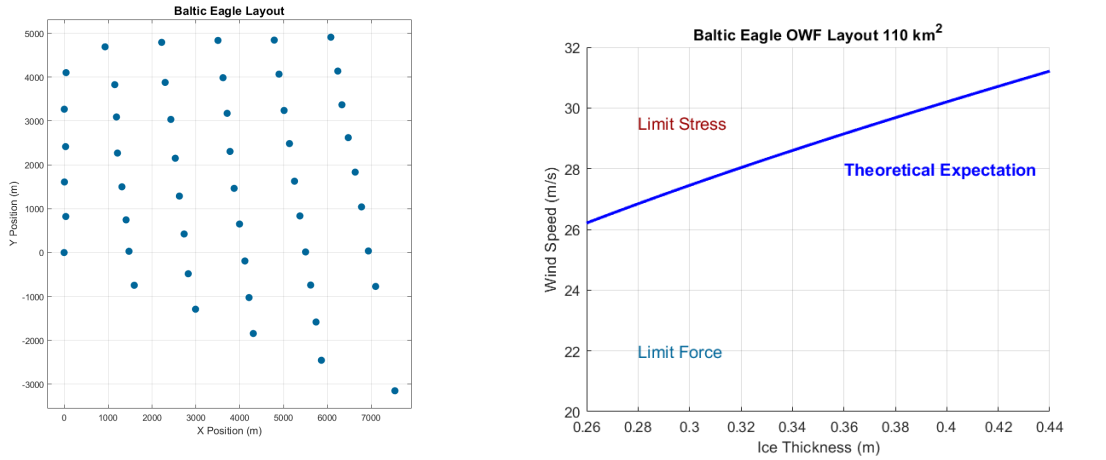

(a) Overview of the Baltic Eagle offshore wind farm layout.

(b) Critical wind speeds required to initiate movement of the stationary grown-in ice sheet that covers the Baltic Eagle wind farm for multiple ice thicknesses.

Figure 7.17: Overview of the grown in scenario for the Baltic Eagle offshore wind farm.

The large number of turbines for the Baltic Eagle wind farm provides a high number of anchor points

for the ice to grow onto. If the wind farm would be fully grown-in, the wind-forcing acting on this large ice body will be sufficient to overcome the resistance from the turbines for multiple combinations of ice thickness and wind speed. Simulations indicate that crushing may be initiated if the wind speed exceeds the critical threshold for a duration of several seconds, a scenario that may occur during wind gusts. From Figure 7.17b it is observed that the critical threshold is approximately 26 m/s. Extreme wind speeds - including those exceeding 26 m/s - are often associated to storm events in the Baltic Sea. For example, during a storm in January 2019, wind speeds reached 32.5 m/s, highlighting the potential for such extreme conditions to occur (Björkqvist, 2020). With a lack of historic storm data in the Baltic Sea, it is assumed that storm frequency in the Baltic Sea follows the same general trend as in The Netherlands. Historic data indicates that storms in The Netherlands tend to occur more frequently during winter than in spring (Vautard, 2019). However, the thickness of winter ice is generally close to 0.44 m (Gravesen, 2009), making it more difficult for the wind forcing to overcome the resistance from the turbines. Thus, a combination of spring ice - having a thickness of 0.26 m - and a spring storm may be the most likely scenario to initiate crushing.

7.2.4. Buffer Distance Turbines - Ice

In the previous section the results were discussed using a buffer distance of 0.10 m in between the ice and the turbine. Now the buffer distance is set to 0.01 m, 0.10 m and 1 m to analyse the effect of the ice confinement surrounding the turbine on the ice-structure interaction. Only the results for the 3 x 3 turbine configuration are discussed, since it can be assumed that the results for a 4 x 4 will only quantitatively differ but not qualitatively.

Figure 7.18 displays the critical combinations of wind speed and ice thickness that lead to crushing of the ice at the turbines for the varying buffer distances. The minor deviation between the three simulations is most likely due to the limited number of simulations that is used for determining the critical wind speed, and numerical errors that may occur in SIBIS. It is not expected that the wind-forcing required for crushing is dependent on the buffer width.

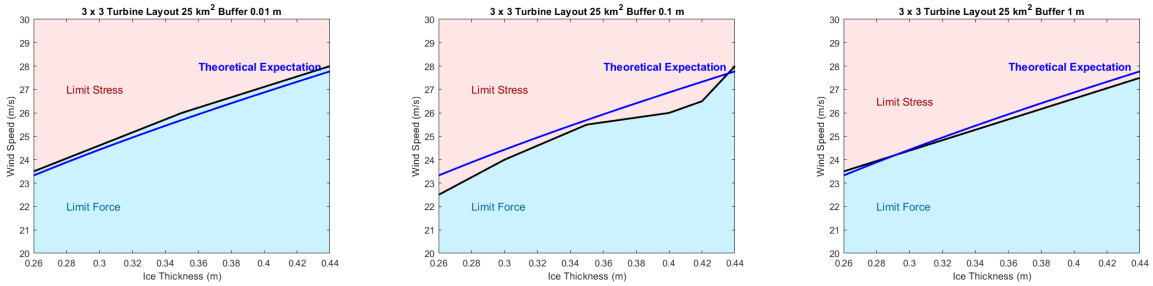

(a) Buffer distance 0.01 m. **(b)** Buffer distance 0.10 m. **(c)** Buffer distance 1 m.

Figure 7.18: Critical combinations of wind speed and ice thickness to initiate crushing for varying buffer distances.

For both a distance of 0.01 m and 0.10 m it is found that the transition between no crushing and crushing is very sudden. Crushing is only initiated once the critical combination of wind speed and ice thickness is sufficient for continuous crushing, which is defined as a limit stress condition. In this scenario, there is sufficient driving force from the wind to generate ice actions across the total width of the structure. This can be explained for the example of an ice thickness of 0.35 m, a gap distance of 0.01 m and wind speeds of 25.5 m/s and 26 m/s respectively. For the lower of the two wind speeds, no movement of the ice sheet happens, while for the wind speed of 26 m/s, sustained crushing is observed. Thus, crushing continues once it is initiated, as the wind-forcing is sufficient to overcome the resistance from the turbines.

A buffer distance of 1 m leads to different results as compared to 0.1 and 0.01 m. Although the wind speed required for a limit stress condition is not any different, an intermediate regime can be defined, namely limit momentum. For a buffer distance of 1 m, the ice has more time to build up speed before it starts interacting with the turbine. Therefore, the ice drift speed at the moment of interaction with the structures is higher. Due to this high speed, crushing will occur at lower wind speed as compared to buffer distances of 0.10 m and 0.01 m. However, the crushing is only momentarily

and will not sustain for a long period as the interaction is limited by the kinetic energy of the ice. This is defined as a limit momentum condition. Now Figure 7.19 shows the critical combinations of ice thickness and wind speed that lead to both limit stress and limit momentum for a buffer distance of 1 m. The orange area shows the combinations for which limit momentum occurs. The analysis is extended by evaluating this scenario for an ice thickness of 0.44 m with wind speeds of 28 m/s and 24 m/s, leading to limit stress and limit momentum respectively. Figure 7.19 shows that in limit stress, the crushing force is equal to 2 MN on a single turbine. For the limit momentum condition, the ice force stabilizes at 1.5 MN. Initially, the ice force peaks at 2 MN, but this only lasts for 200 seconds, up until the point where crushing stops. Figure 7.15 also shows an initial peak load for a wind speed of 21 m/s. However, this is not considered as limit momentum as it only lasts for a few seconds after contact with the ice. Figure 7.20 shows the observed crushing for a 1 m gap in between the structure and the ice, an ice thickness of 0.26 m and various wind speeds. Only a wind speed of 23.5 m/s leads to limit stress and a crushing path length of 119 m after 2330 seconds, as in Figure 7.20c. For Figure 7.20a and Figure 7.20b, the wind speed only induces limit momentum and the crushing paths stop at 26 m and 49 m respectively.

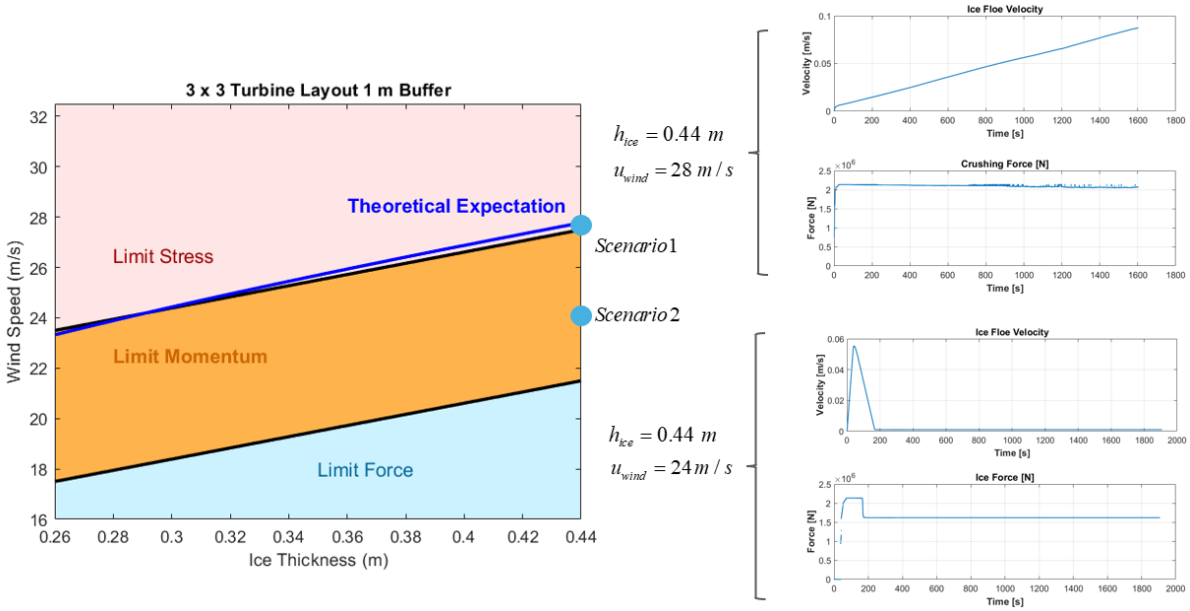

Figure 7.19: Critical combinations of ice thickness and wind speed that lead to limit momentum and limit stress for a buffer distance of 1 m. The ice floe velocity and ice loads are depicted for a single turbine.

(a) Observed crushing for a 1 m buffer distance, ice thickness 0.26 m and wind speed of 22.5 m/s. The crushing stops after 660 seconds and a crushing path length of 26 m, which is the instant shown in the image. No limit stress occurs.

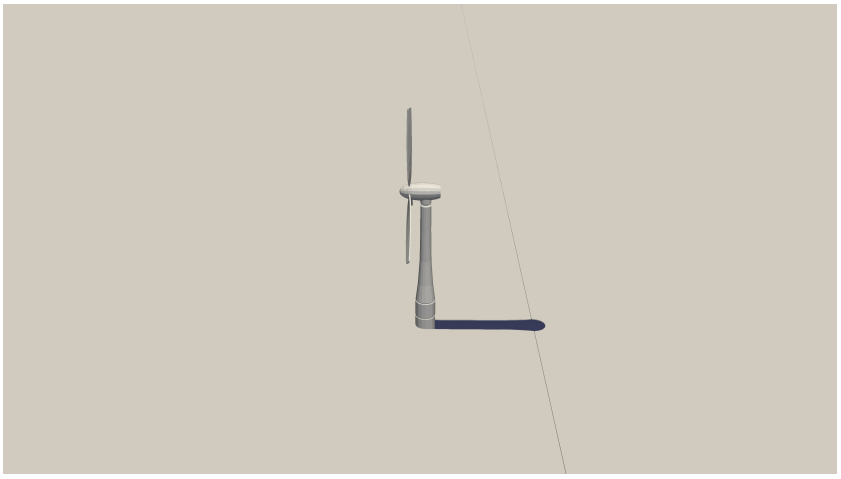

(b) Observed crushing for a 1 m buffer distance, ice thickness 0.26 m and wind speed of 23 m/s. The crushing stops after 1270 seconds and a crushing path length of 49 m, which is the instant shown in the image. No limit stress occurs.

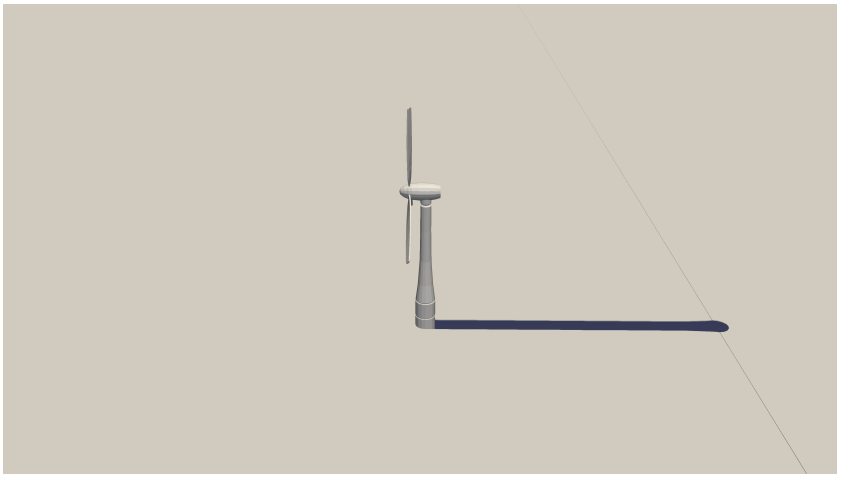

(c) Observed crushing for a 1 m buffer distance, ice thickness 0.26 m and wind speed of 23.5 m/s. The observed crushing length is 119 m after 1410 seconds (the instant shown in the image) and increasing further with time. This is the wind speed for which limit stress occurs.

Figure 7.20: Crushing path lengths for a buffer distance of 1 m and varying wind speeds.

8

Discussion and Recommendations

The present chapter comprises of multiple parts. First, it discusses in Section 8.1 what implications the selection of boundary conditions in Chapter 3 may have on the results that are presented in Chapter 7. Secondly, Section 8.2 explains the issues that arose during the image processing and what effects they may have. Third, it is discussed in Section 8.3 what effects should be considered for the scenarios in which the floes originate from outside of OWF, and how they may be further studied. Section 8.4 discusses the limitations of the results for the frozen in wind farm. Lastly, Section 8.5 presents how the results would change for an offshore wind farm that is modelled after the existing Baltic Eagle wind farm. Throughout these sections, recommendations are provided by the author regarding several aspects that can be explored in further research.

8.1. Reliability of Selected Boundary Conditions

This thesis assumed a constant wind speed of 10 m/s at a height of 10 m for the situation in which the floes originate from outside of the OWF. This may have some implications for the macroscale ice drift that is observed across the simulations. From visual analysis of animation of the simulations it was observed that a wind speed of 10 m/s is sufficient to sustain continuous ice floe movement and rarely lead to obstruction of the ice floes at the turbines. Furthermore, the wind speed is sufficient to initiate crushing at the ice-structure interface. It is important to note that the macroscale drift is dependent on the selected wind speed. It is speculated that if a lower wind speed would be used, obstruction of the ice floes may be observed more frequently, as the driving force from the wind is insufficient to initiate crushing. In this scenario, the first row of turbines may act as a complete barrier to further ice drift, leading to the accumulation of ice floes in the wind opposing direction without significant splitting or crushing at the floe front. It is expected that the velocity reduction relative to the free drift speed in this scenario is more significant as compared to a wind speed of 10 m/s. Conversely, selecting a wind speed exceeding 10 m/s is likely to result in more frequent occurrences of ice floe crushing, with obstructions becoming increasingly rare. The velocity reduction relative to the free drift speed will likely be lower as compared to a wind speed of 10 m/s.

In Section 3.1, it was explained that the choice is made to set the current speed of the water to zero. This assumption was made as the near-surface current speed in the Baltic Sea is highly varying in both magnitude and direction and depends primarily on weather. The temporal variation of water currents underneath the ice is often neglected due to a shortage of presently available observations. This may have some implications for the ratio of ice drift speed to surface wind speed:

- When the water surface currents and the wind direction are fully-aligned, this will increase the ratio. The ice drift speed now stabilizes at 0.40 m/s.
- If the water surface current and the wind direction are misaligned, the ratio will most likely fall in between 3 - 4%. However, the misalignment between wind- and ice loading direction may have implications for the structure.

In the presence of a water current, the ratio of ice drift speed to surface wind speed is expected to vary between 3 - 4%. At a drift speed of 0.4 m/s, it is expected that the floes will experience a notable velocity reduction at the turbines. Generally, the floe speeds at the turbines will be higher as compared to the other ratios as the driving force from the wind is higher. The higher drift speed will lead to a more forceful accumulation of floes behind the floe front, exerting greater pressure. This may facilitate more splitting and crushing of the floe front. Furthermore, it is speculated that the driving force from the wind

will reduce the probability of floes being obstructed by the turbines, as this wind speed is sufficient to initiate crushing and splitting. Introducing a current that is aligned with the wind direction thus leads to the same results a increasing the wind velocity. If the wind- and current direction are misaligned, ice-induced vibrations can develop up to higher ice drift speeds as compared to an aligned scenario (Hammer et al., 2023). Therefore this should be a point of consideration for further research.

The ice strength coefficient that was used throughout the simulations is similar as to those used in offshore wind projects in the Kattegat and Baltic Proper regions (in the Southern Baltic Sea), which varied between 0.66 MPa and 1.1 MPa. Accounting for the velocity effect (ice loads being higher at low ice drift speed) may increase the ice strength coefficient to values between 1.3 MPa and 2.2 MPa (Hendrikse, 2024). The value of C_R = 0.725 MPa in this thesis is therefore low compared to what is used in general, as it reflects an average annual strength value rather than a maximum. The value is rather specific, since it was previously used to reproduce a specific ice load onto a turbine. Using a lower ice strength coefficient promotes the (re)-initiation of motion of the stationary ice sheet, lowering the critical wind speeds. If the floes originate from outside of the OWF, lowering C_R may increase the occurrence of crushing instead of splitting. Other ice parameters such as density, shear strength, Youngs Modulus, poisson ratio and fracture toughness are related to first year sea ice. Winter ice in the Southern Baltic Sea is predominantly first year ice. Therefore the selected values align well with the mechanical behaviour of ice that would be expected during winter in the Southern Baltic Sea. A level ice thickness of 0.26 to 0.44 m was used based upon an extreme value analysis for a 50-year return period. Considering the seasonal evolution of sea ice in the Baltic Sea, it is likely that these values overestimate the ice thickness as winter transitions into spring.

As explained in the introduction, SIBIS does not incorporate the effect of wave fields since it does not account for first- and second-order hydrodynamic effects. However, several studies have explored the correlation between wave fields and the evolution of the ice floe size distribution in Arctic waters. Roach et al. (2019) presents that ocean wave-induced fracturing is the dominant process affecting the floe size distribution during the melt-season. The fracturing leads to a reduction of floe size. The principles presented by Roach et al. (2019) primarily hold for oceanic waves. However, Dumont et al. (2011) states that the mechanism of wave-induced fracturing are similar, regardless of whether the waves originate from oceanic- or sea-environments. Wave-induced fracturing is likely to occur in the Baltic Sea, in particular during storm events when the significant wave height can reach up to 4.46 m (Soomere et al., 2011). The reduction in maximum floe size could potentially lead to a less-severe loading condition on the offshore wind farm. Furthermore, SIBIS does not include the formation of ocean wakes behind the turbines, which could have an effect on the floe motions. For example, the ice motions may feed back onto local ocean currents, as the formation of a wake in the surface ocean current could be induced by sea ice being obstructed.

The selected mesh settings and maximum split length were based upon several key issues that occurred throughout the research. During ice-structure interaction in SIBIS, the ice breaking of floes involves multiple complex operations based on polygon clipping. In crushing, the clipping process identifies the intersection between the structure contour and the floe shape, returning the floe shape without this intersection. During ice breaking (crushing, bending, splitting), the floe shape is clipped by the structure contour to identify the broken pieces. The ice-structure interaction is resolved in multiple phases:

1. The collision detection phase determines contact points between 3D mesh bodies (turbines, floes, etc.).
2. The contact resolution phase determines contact forces applied to the bodies.
3. If contact forces exceed ice breaking limits, an ice failure is created, and the floe is broken. During this ice breaking phase, only the floe shape and the structure contour at the waterline (2 polygons) are considered, and clipping processes are used to determine the ice failure.
4. The last phase consists of the floe 3D mesh reconstruction from its shape using an extrusion.

Clipping is thus an essential part of the mesh engine. Throughout performing the simulations, it was found that very large ice floes can result in failure of the clipping. This occurs when the turbine enters a very large ice floe via crushing, creating a very narrow channel compared to the floe diameter. When the maximum split length is limited, the turbines must continue crushing. At one point, this will lead to

incorrect clipping, resulting in a polygon with a hole. To address this issue, the mesh engine of SIBIS was updated. It was found that for some floe geometries, the updated mesh engine is still unable to handle the very large floes that the turbines encounter. This was predominantly the case for the floe field with radii of 282 - 4850 m. The value for β that was used results in a high threshold that must be exceeded to initiate splitting. It was therefore chosen to not define a maximum splitting length in SIBIS. Under conditions that would typically result in an error, the ice floe undergoes splitting instead of crushing. This should be combined with the mesh settings as described in Table 3.2.

As the high threshold load that was used for splitting is transferred onto the structure, it may result in significant loads on the turbines that must be exceeded before fracture occurs. It is expected that for most floe geometries - primarily for small ice floes - the choice of β is not expected to significantly affect the results. This is because the splitting load increases with increasing distance towards the open water, which is low for small floes. However, it remains unknown what implications the selected splitting model - in terms of β - may have for large ice floes. The significant load that is required for splitting these large floes could affect the occurrence of crushing. Furthermore, it remains unknown what effect the current definition of the splitting length has. Without introducing a maximum splitting length - as was done in this thesis - the very large ice floes are split instantaneous during ice-structure contact, given that the threshold splitting load is exceeded. If a maximum split length was defined, large ice floes are expected to split only once the turbine has penetrated the ice sufficiently close to the edge of the ice sheet. The crushing that has taken place prior to the fracture will reduce the ice drift speed as compared to splitting of the floe. Furthermore, the floe may be rotated by neighbouring floes during crushing, creating a non-straight crushing path. This ultimately changes the floe geometry. Even when disregarding the absence of crack propagation, it is thus speculated that the selection of the splitting model can affect the macroscale ice drift.

8.2. Acquiring an Ice Floe Size Distribution of the Southern Baltic Sea

Image processing was identified to be the most accurate way of obtaining an ice floe size distribution that is representative of the Southern Baltic Sea. However, the floe size distributions that results from image processing often show concave-down curvature for larger floe sizes. This behaviour is most likely due to the satellite imagery failing to capture the largest floes, in combination with the cut-off of floes at the image borders that happens during the image processing. Therefore, the number of very large floes is underestimated due to the image processing. This would lead to a lower x_{max} than is generally observed from the satellite images, as the floes that are not captured or cut-off often tend to be the largest. While the reduction of maximum floe size that results from these processes is difficult to quantify, Figure 5.3 shows that the concave-down curvature is not very pronounced. Furthermore, the averaging of x_{max} across the 20 images allows for multiple images that contain very large floes in the middle of the image which are not being cut-off. For example, one of the images captured on February 28 captured a floe having a size of 774 km^2. This floe is significantly larger compared to the other maximum floe sizes. It is therefore speculated that this observation alleviates the average x_{max} across the image processing results.

During the image processing, only images from the month of February were selected as only these images provided sufficient ice cover and low cloud cover. Denton et al. (2022) found that during summer the FSD generally steepens, indicating that the proportion of small floes to large floes is increasing. This is due to the melt and breakup of floes that starts during spring and continues in summer. However, the steeping of the power law exponent was found to initiate in May. During the winter months, the variability was minimal. It is therefore expected that selecting images solely from February does not introduce any significant error in obtaining an ice floe field that is representative of winter conditions.

Since no images with sufficient ice cover were available for the Southern Baltic Sea, images from the Northern Baltic Sea were used instead. These were combined with ice parameters for the Southern Baltic Sea. In the Northern Baltic Sea, the ice cover is generally thicker and more stable. Small floes are often glued together due to ice growth to form a single large floe. Therefore, larger floes are more common. As the conditions in the Southern Baltic Sea are milder, the ice is thinner and smaller floes are observed more frequently (Meier et al., 2021; Horvat et al. 2015). This could potentially steepen

the slope of the FSD as compared to what was found in this thesis, corresponding to a higher proportion of small to large floes. Furthermore, the maximum observed floe size in the Southern Baltic Sea will most likely be lower. It is unknown to what extend the FSDs for the two regions will differ. It is therefore difficult to quantify the effect of using an FSD of the Northern Baltic Sea.

8.3. Ice Drift Speed Reduction for Ice Floes that Originate from Outside of the OWF

Figure 7.4 shows that the second- and third row of turbines are not protected from ice-structure interaction by the first row of turbines. Although this shielding effect was not found for the 282 - 4850 m SIC 80% ice field, it did occur for the 80 - 1000 m SIC 60% field. This can be attributed to a single large floe that is stuck at the fist row of turbines for the latter simulation, forcing the ice around it and protecting the turbines behind it. It is speculated that the shielding effect is also related to the average floe size. For small floe sizes, a large proportion of the floes drift in between the turbines without interaction. For large floe sizes, the floes may even interact with the second- or third row of turbines as a single split is not sufficient to allow the passage without interaction. It is also speculated that this may be attributed to the creation of very long fracture lines during splitting of large floes. This creates more elongated floes having parallel-opposite edges. Van den Berg (2019) argued that these floe geometries may induce bridging and accumulation of floes. This will be further explained later in this section.

It was observed that the length of the ice floe field in the wind-direction has a major influence on the macroscale ice-structure interaction. As the initial floe front interacts with the turbines, the trailing floes will accumulate behind the stagnated front. This exceeds great pressure onto the floes at the positions of the turbines. In many cases, the pressure from the accumulated floe field forces crushing or splitting of the floes at the turbines. This thesis has only implemented floe fields having a rectangular shape. Thus the length of the floe field varies between 12, 20 and 30 km depending on the floe size range that is used. It is expected that once the length of the floe field drops below a certain N times the average floe diameter, the macroscale ice-structure interaction will change as the pressure onto the floe front is notably lower. For example, if the length of the floe field is approximately equal to 2 times the average floe diameter, only a single row of floe will accumulate behind the floe front.

This thesis identified that the spatial extent of the speed reduction across the ice floe field can primarily be attributed to the average floe size across the floe field. As the average floe size increases, the deceleration of ice floes reaches further into the ice field. Furthermore, the constant deceleration and acceleration due to splitting, crushing and rotation causes an oscillating pattern of the fraction of the floe field that is affected by the turbines. It is speculated that the timescale of the oscillation increases as the average floe size becomes larger. It is expected that a floe field of 282 - 4850 and SIC 80% (as shown in Figure 7.9) would eventually show an oscillating pattern as in Figure 7.11 for a floe size of 80 - 1000 m and SIC 80% but with a longer timescale. As the splitting of the very large floes takes a significant time, a timescale of 20000 seconds is most likely too short to unveil an oscillation. Furthermore, it remains unclear whether Figure 7.3 already shows a steady state, in the sense that the average velocity does not reduce any further. This would require performing simulations for a longer time period. For lower sea ice concentrations, there is less accumulation behind obstructed floes, since there is more space for redistribution and the ice floes can find a way around the OWF. Therefore, the oscillating pattern is less pronounced.

Currently, SIBIS enables the user to identify the floes by their label. For example, floe 5 is split into floe 6 and 7 after a splitting event. However, if the two child floes would be related via their label to the parent floe (floe 5 is split into 5.1 and 5.2), a more thorough analysis could be performed on the spatial extend of the speed reduction. This would also require implementing the tracking of the floe centroids in SIBIS. As the floe area can be tracked in the updated version of SIBIS (Version V3 1.2), the FSD before- and after interacting with the OWF could be analysed if the centroids are tracked. For further research, it would then be interesting to explore what kind of FSD would be expected for an OWF that is positioned behind the OWF that first encounters the ice floe field. As the large ice floes are split into smaller floes, it is expected that the secondary OWF will encounter a lower number of very large floes.

Tracking the centroids of the ice floes would enable capturing the spatial extent of the velocity reduction over time, instead of measuring it based on visualization of the simulations at only a few timesteps.

Plotting the average speed versus the distance to the turbine would enable to show the functional form of the velocity decay and help providing a theory to predict the reduction. The propagation of the speed reduction could then be coupled to the fraction of the floe field that is affected by the presence of the OWF. Then, this fraction can be related to the total mass of the ice that is pushing onto the structures, as this is relevant for the loading of the individual turbines. It could then be analysed whether this leads to a maximumm load on the turbines.

The wind direction that is selected in this thesis aligns with the parallel edges of the offshore wind farm. Furthermore, the floe front is aligned with the first row of turbines. It remains unknown how the selected wind direction will affect the results, as changing the wind direction - or the orientation of the OWF - by 45 degrees could lead to different results. This will most likely influence the row-wise shielding, as the distance in between the turbines from the perspective of the ice floes changes. It is highly likely that the turbine located at the corner closest to the ice floes would experience the highest loads. For further research, it would therefore be interesting to explore the effect of varying wind direction.

Fracturing of ice floes during splitting can only occur along straight lines in SIBIS. Figure 7.6 shows that this may lead to very elongated floe shapes with sharp edges. Van den Berg (2019) argues that floe shapes having parallel opposite edges - such as rectangular floes - are more prone to bridging and floe accumulation in front of the structures, as they may lead to a greater length and stability of force chains. It is expected that the introduction of irregular fracture lines may have an effect on the accumulation of floes inside- and in front of the offshore wind farm.

8.4. Occurrence of the Intimate Contact Condition

This thesis introduced that the critical wind speed in frozen in conditions across multiple OWF configurations can be predicted by the critical wind drag force required to (re)-initiate sustained movement of the ice sheet. The distance from the outer turbines to the open water was set to 1500 to enforce crushing. It remains unknown to what extent the ice will grow beyond the outer turbines. It is speculated that in reality this distance will most likely be lower than 1500 m. In that case, the area of the ice sheet would generally be lower and the critical wind speeds would be higher for the given number of turbines. Consequently, this thesis may underestimate the critical wind speed thresholds compared to those expected under real-world conditions. Figures 7.15 and 7.19 show the time series of the ice velocity and ice loads at the position of a turbine for a duration of several minutes, as design scenarios are typically simulated for 10 minute time series. If velocity dependent crushing would be included, the ice force would follow a pattern that resembles the ice induced vibrations that are expected for this velocity range. Moreover, it remains unclear how including discontinuous wind speeds that vary in time would change the ice-structure interaction in this scenario.

Furthermore, it should be noted that equation 7.2 has only been verified for a square-shaped wind farm and ice sheet, with evenly distributed turbines. Therefore, several aspects could lead to different behaviour than observed so far:

- If some turbines are positioned further from each other, this may locally reduce the critical speed needed to a limit stress condition, as the local density of turbines decreases. However, it is uncertain if the ice growth can still bridge the gap in between two turbines if they are positioned very far from each other. Positioning the turbines closer to each other will promote ice growth. However, as the density of turbines increases, it will also increase the resistance.
- In reality, it may be possible that the edge of the ice sheet is very close to one of the outer turbines. Locally, this can lead to a split that initiates at the turbine and propagates towards the open water. After splitting, the open water may be closer to one of the other turbines. This can then lead to a secondary splitting event. This process may continue until the complete ice sheet has been broken into smaller fragments. In this scenario, the limit stress condition is most likely not expected at the critical wind speeds as previously described. Rather, it depends on the area and geometry of the ice sheet after splitting and the number of turbines connected to the ice sheet. It is also likely that irregular crack paths and crack propagation would influence this process.

The buffer distance in between the turbines and the surrounding ice remains an unknown parameter. Therefore, it was varied across the simulations to analyse how it affects the critical combinations of wind speed and ice thickness. It was shown that for a buffer distance of 0.01 and 0.1 m the transition

between limit force and limit stress is very sudden. For a buffer distance of 1 m, limit momentum was identified as crushing may be initiated for lower wind speeds. However, this crushing is found to be only momentarily. The combinations of critical wind speeds and ice thickness to initiate sustained crushing are therefore not expected to be dependent on the buffer distance. It was observed that the limit stress condition leads to higher forces on the structures as compared to limit momentum and limit force. The deviations between the wind speed thresholds as shown in Figure 7.18 are assumed to be caused by the limited number of simulations that have been performed.

Finally, Hendrikse (2024) formulates the possibility of ridge building from drift ice around the edges of the OWF during a frozen in condition. These ridges may protect the inner structures from high ice loads, while increasing the loads on the outer turbines. Currently, it is unclear whether the inner structures can be designed for lower ice loads. The formation of ice ridges around the frozen in ice sheet was not considered in this thesis. Further research into this topic may provide opportunities for the strategic placement of substations and wind farm layout optimization.

8.5. Generalization of Results

During this thesis, two distinct scenarios have been simulated to analyse the influence of an offshore wind farm on the ice drift speed in the Southern Baltic Sea. Due to limited computational power, the choice was made to limit the simulations for the two scenarios to a 3 x 3 and 4 x 4 turbine layout. A primary reason for this was that a larger OWF also requires a significantly larger floe field to ensure confinement in the direction perpendicular to the wind direction. In reality, an offshore wind farm such as the Baltic Eagle may have 50 turbines. In future research, it should be investigated to what extent this scaled-down version of the OWF affects the simulation results. This holds true for both simulation scenarios.

The results in Chapter 7 show that the lowest floe speed is often achieved for a single floe that is obstructed by the turbines. For floe fields with a high average diameter - such as the 282 - 4850 m - the ratio between the large floe diameters and the full-scale OWF dimensions will be very different as for a 3 x 3 turbine layout. It is therefore expected that for the largest floes, the interaction with the OWF will be notably different for a full scale turbine layout. Instead of drifting around the wind farm, the floes are forced to drift through it via splitting or crushing. It was speculated that the presence of very large floes also affects the shielding of secondary- and tertiary rows. This may differ as the ratio of floe size to OWF changes. For a full scale OWF such as the Baltic Eagle wind farm, it should also be studied if the loading for the inner turbines is any different as compared to the outer turbines in the direction perpendicular to the wind direction. In this thesis, it was presented that the ice drift speed is lower at the inner turbines, but it remains uncertain whether this also holds true for a full scale OWF.

The remaining uncertainty concerning the role of very large floes onto the obstruction and consequential shielding of turbines can be eliminated if a high number of simulations could be performed, simulating a longer time period ($\approx$ 24 hours). Metrikin et al. (2015) states that the ice-structure interaction is a stochastic process since the bearing capacity of a broken ice field depends on the distribution and shapes of a large amount of individual floes. Thus, a small perturbation of an individual interaction event - for example rotation instead of fracture of an ice floe - may lead to substantially different response of the floe field, leading to a different global action onto the turbines. This indicates that not only the effect of very large floes, but also other obscured effects can be resolved via this approach. A floe field of 282 - 4850 m and SIC 80% could be generated a high number of times using the synthetic floe field generator, each time creating a randomized floe field.

The extrapolation of the critical wind speeds to the Baltic Eagle wind farm was not validated in this thesis as the presented equations have only been validated for a square OWF with evenly distributed turbines and a square ice sheet. The turbines in the Baltic Eagle wind farm are not evenly distributed. This could possibly promote crushing locally. It is speculated that in reality the process will not only depend on the critical wind drag force for (re)-initiation of the ice sheet. Imperfections of the ice sheet may locally promote crushing, as the ice sheet will be inhomogeneous in reality, which is not accounted for by SIBIS. Variations in ice strength and ice thickness could affect the results. Furthermore, the distribution of wind loading onto the ice sheet may be affected by the presence of a high number of turbines. The inner part of the ice sheet may experience lower wind forcing as compared to the edges. Moreover, the

results may be sensitive to the choice of input parameters. For example, if the ice strength coefficient would be lower due to melting, the critical threshold for wind speed at which the ice starts crushing is decreased. A higher skin friction coefficient - related to high surface roughness - could also lead to a reduced threshold. Finally, the buffer distance in between the turbines and the ice is most likely not equal across all turbines. This may lead to an uneven distribution of the loading onto the turbines.

9
Conclusion

Offshore wind turbines have been shown to experience most severe loading at low relative velocities, as intermittent crushing and multi-modal ice structure interaction lead to ice-induced vibrations. The velocities of ice floes at the turbines are expected to be related to the sea ice concentration, floe size, ice-ice interaction and the presence of neighbouring turbines. This thesis therefore described the ice-structure interaction between ice floes and offshore wind turbines on macroscale. The turbines may act as obstruction, affecting the ice drift speed by lowering the ice floe drift velocity. The presence of multiple turbines may also lead to a stationary ice sheet during a frozen in condition, as turbines act as anchor points for the ice, thus promoting ice growth. This led to the main research question:

How does the presence of an offshore wind farm affect the ice drift speed for both an ice floe field that originates from outside the offshore wind farm and a grown-in condition in the Southern Baltic Sea?

To address the main research question, two scenarios were simulated: (1) the drift of ice floes originating from outside of the OWF and (2) the drift of an ice floe that is initially frozen-in around the turbines. This thesis employed image processing of observational data from satellite imagery to acquire an ice floe size distribution that is representative of the Southern Baltic Sea. The image processing was then connected to the generation of synthetic floe fields on the scale of an OWF. This enabled modelling of ice drift under varying floe field configurations, mimicking the diverse and dynamic nature of ice floe fields.

The posed research questions are answered as follows:

RQ1: *How does the presence of an offshore wind farm affect the drift speed of ice floes when they originate from outside of the offshore wind farm?*

The presence of the offshore wind farm significantly lowers the drift speed of ice floes. This is observed for both a single turbine and multiple turbines. The results show that the correlation between the wind speed and the ice drift speed is lost and that the lowest drift speeds occur for ice floes that are in direct contact with the turbines. Without any turbines present, the ice floe field velocities follow a Gaussian distribution with a mean of 0.29 m/s. The presence of the turbines skews the Gaussian distribution towards low velocities, leading to a long tail of the CDF of the ice velocities. The ice velocities at the turbines were on average found to reduce by 41.6% as compared to the case without turbines. The 1st percentile of ice floe velocities was found to reduce by 65.3% due to the presence of the structures. The velocities that are observed at the turbines are in the velocity range to promote intermittent crushing and multi-modal ice-structure interaction, leading to ice-induced vibrations. The ice that is not in direct contact may push and rotate the floes at the turbines, changing their drift speed. Furthermore, turbines may act as rotation points for ice floes, affecting the ice drift speed at other turbines. This may lead to ice drift speeds having both positive and negative components not only in the wind-aligned direction but also in the direction perpendicular to the wind. This multidirectional loading promotes a misalignment of the wind- and ice drift speed direction. During such a misaligned scenario, ice-induced vibrations can develop up to higher ice drift speeds. This interaction among ice floes and neighbouring turbines emphasizes the importance of macroscale modelling of an OWF, as the analysis of the drift speed of ice floes at the turbines should account for both the ice floes in direct- and indirect contact with the structures. Although no shielding effect of the secondary- and tertiary row was observed, it is discussed that this may be related to the maximum floe size and more simulations should be performed. Sensitivity of the results to the sea ice concentration and maximum floe size were analysed and coupled to the

spatial extent of the speed reduction across the floe field.

RQ2: *What critical combination of wind speed and ice thickness is required to (re-)initiate the movement of a stationary ice sheet in a frozen-in offshore wind farm, leading to an intimate contact condition?*

The (re)-initiation of a stationary ice sheet that covers the offshore wind farm can result in a limit stress condition for several combinations of wind speed and ice thickness that are typical in the Southern Baltic Sea. The required wind speed to promote the resulting intimate contact condition across various OWF-layouts is related to the critical wind drag force and resistance from the turbines, introducing an analytical equation that was used to verify simulation results and extrapolate the results to larger offshore wind farms, covering a higher number of turbines. For the example of the Baltic Eagle offshore wind farm, it was found that all wind speeds above 26 m/s have the potential to initiate a limit stress condition at the ice-structure interface for ice thicknesses typical of the Southern Baltic Sea. The limitations were analysed in combination with varying the buffer distance between the turbines and the surrounding ice. It was found that the limit stress condition leads to higher ice forces on the structures as compared to the limit momentum- and limit force condition.

10 Literature

- Alfred Wegener Institute. (2019, April 3). *Example of a floe field in the Arctic characterized by a low sea ice concentration. phys.org.* https://phys.org/news/2019-04-transpolar-drift-falteringsea-ice-nursery.html
- Åström, J., Robertsen, F., Haapala, J., Polojärvi, A., Uiboupin, R., Maljutenko, I. (2024). *A large-scale high-resolution numerical model for sea-ice fragmentation dynamics. the Cryosphere, 18(5), 2429–2442.* https://doi.org/10.5194/tc-18-2429-2024
- Bateson, A. W., Feltham, D. L., Schröder, D., Hosekova, L., Ridley, J. K., Aksenov, Y. (2020). *Impact of sea ice floe size distribution on seasonal fragmentation and melt of Arctic sea ice. the Cryosphere, 14(2), 403–428.* https://doi.org/10.5194/tc-14-403-2020
- Bateson, A. W., Feltham, D. L., Schröder, D., Wang, Y., Hwang, B., Ridley, J. K., Aksenov, Y. (2022). *Sea ice floe size: its impact on pan-Arctic and local ice mass and required model complexity. the Cryosphere, 16(6), 2565–2593.* https://doi.org/10.5194/tc-16-2565-2022
- Bhat, S. (1988). *Analysis for splitting of ice floes during summer impact. Cold Regions Science and Technology, 15(1), 53–63*. https://doi.org/10.1016/0165-232x(88)90038-9
- Björkqvist, J., Rikka, S., Alari, V., Männik, A., Tuomi, L., Pettersson, H. (2020). *Wave height return periods from combined measurement–model data: a Baltic Sea case study. Natural Hazards and Earth System Sciences, 20(12), 3593–3609.* https://doi.org/10.5194/nhess-20-3593-2020
- Brenner, S. (2024). *Floe Field Generator Code*. https://github.com/sdbrenner/makeFloeField/blob/main/README.md
- Cieślikiewicz, W., Cupiał, A. (2024). *Long-term statistics of atmospheric conditions over the Baltic Sea and meteorological features related to wind wave extremes in the Gulf of Gdańsk. Oceanologia, 66(2)*. https://doi.org/10.1016/j.oceano.2023.10.002
- Cole, S. T., Toole, J. M., Lele, R., Timmermans, M., Gallaher, S. G., Stanton, T. P., Shaw, W. J., Hwang, B., Maksym, T., Wilkinson, J. P., Ortiz, M., Graber, H., Rainville, L., Petty, A. A., Farrell, S. L., Richter-Menge, J. A., Haas, C. (2017). *Ice and ocean velocity in the Arctic marginal ice zone: Ice roughness and momentum transfer. Elementa Science of the Anthropocene, 5.* https://doi.org/10.1525/elementa.241
- Croasdale, K. R. (1975). *Ice Forces on Marine Structures. IAHR Third International Symposium on Ice Problems*. https://www.iahr.org/library/infor?pid=28689
- Denton, A. A., Timmermans, M. (2022). *Characterizing the sea-ice floe size distribution in the Canada Basin from high-resolution optical satellite imagery. The Cryosphere, 16(5), 1563–1578*. https://doi.org/10.5194/tc-16-1563-2022
- Dumont, D., Kohout, A., Bertino, L. (2011). *A wave-based model for the marginal ice zone including a floe breaking parameterization. Journal of Geophysical Research Atmospheres, 116(C4)*. https://doi.org/10.1029/2010jc006682
- European Union, European Space Agency. (2018-2024). *Copernicus Browser. documentation.dataspace.copernicus.eu.* https://browser.dataspace.copernicus.eu/?zoom=5&lat=50.16282&lng=20.78613&themeId=DEFAULT-THEME&visualizationUrl=U2FsdGVkX19Sh5%2Fyf1HUZpiVwktBHgGZoeyv6UsB9U4uj6RUN9QR8%2Fl1B8puRgyhH%2BRJmQb7zLq2QrKjOWunXJ8IcQpASmGwULPrUI6NdGal%2FbkbMyeakVhB8h1Z5GRf&datasetId=S2_L2A_CDAS&demSource3D=%22MAPZEN%22&cloudCoverage=30&dateMode=SINGLE

- Finnish Meteorological Institute. (n.d.). *Ice conditions. en.ilmatieteenlaitos.fi.* https://en.ilmatieteenlaitos.fi/ice-conditions/
- Finnish Meteorological Institute. (2022, September 12). *The currents in the Baltic Sea. en.ilmatieteenlaitos.fi.* https://en.ilmatieteenlaitos.fi/seacurrents
- Finnish Meteorological Institute. (2025, February 28). *Sea Level Variations on the Finnish Coast. en.ilmatieteenlaitos.fi.* https://en.ilmatieteenlaitos.fi/sea-level-variations
- Gao, G., Chen, C., Qi, J., Beardsley, R. C. (2011). *An unstructured-grid, finite-volume sea ice model: Development, validation, and application. Journal of Geophysical Research Atmospheres, 116.* https://doi.org/10.1029/2010jc006688
- Gravesen, H., Bülow Jørgensen, L., Vilhelm Høyland, K., Bicker, S. (2023). *Ice drift and ice action on offshore wind farm structures. Proceedings of the 27th International Conference on Port and Ocean Engineering Under Arctic Conditions*. https://ntnuopen.ntnu.no/ntnu-xmlui/bitstream/handle/11250/3120157/POAC23%2BDrifting%2Bice%2Btoward%2BOWF%2B230505.pdf?sequence=1&isAllowed=y
- Gravesen, H., Kärnä, T. (2009). *Ice Loads for Offshore Wind Turbines in Southern Baltic Sea.*
- Hammer, T. C., Hendrikse, H. (2023). *Experimental study into the effect of wind-ice misalignment on the development of ice-induced vibrations of offshore wind turbines. Engineering Structures, 286, Article 116106.* https://doi.org/10.1016/j.engstruct.2023.116106
- Hammer, T. C., Owen, C. C., van den Berg, M. A., Hendrikse, H. (2022). *Classification Of Ice-Induced Vibration Regimes Of Offshore Wind Turbines. In Proceedings of the ASME 2022 41st International Conference on Ocean, Offshore and Arctic Engineering Article OMAE2022-78972 The American Society of Mechanical Engineers (ASME)*. https://doi.org/10.1115/OMAE2022-78972
- Hammer, T. C., Willems, T., Hendrikse, H. (2022). *Dynamic ice loads for offshore wind support structure design. Marine Structures, 87, 103335*. https://doi.org/10.1016/j.marstruc.2022.103335
- Hanssen-Bauer, I., T. Gjessing, Y. (1987). *Observations and model calculations of aerodynamic drag on sea ice in the fram strait. Tellus 40A, 151–161.* https://a.tellusjournals.se/articles/1740/files/submission/proof/1740-1-43300-1-10-20220928.pdf
- Hendrikse, H. (2024). *Ice engineering challenges for offshore wind development in the Baltic Sea. In T. Kolerski (Ed.), Proceedings of the 27th IAHR International Symposium on Ice (Gdansk, 2024) Article 30436 (IAHR International Symposium on Ice). IAHR.* https://www.iahr.org/library/infor?pid=30436
- Heorton, H. D. B. S., Tsamados, M., Cole, S. T., Ferreira, A. M. G., Berbellini, A., Fox, M., Armitage, T. W. K. (2019). *Retrieving sea ice drag coefficients and turning angles from in situ and satellite observations using an inverse modeling framework. Journal of Geophysical Research Oceans, 124(8), 6388–6413.* https://doi.org/10.1029/2018jc014881
- Herman, A., Jedrasik, J., Kowalewski, M. (2011). *Numerical modelling of thermodynamics and dynamics of sea ice in the Baltic Sea. Ocean Science, 7(2), 257–276.* https://doi.org/10.5194/os-7-257-2011
- Hopkins, M. A., Thorndike, A. S. (2006). *Floe formation in Arctic sea ice. Journal of Geophysical Research Atmospheres, 111(C11).* https://doi.org/10.1029/2005jc003352
- Hordoir, R., Axell, L., Höglund, A., Dieterich, C., Fransner, F., Gröger, M., Liu, Y., Pemberton, P., Schimanke, S., Andersson, H., Ljungemyr, P., Nygren, P., Falahat, S., Nord, A., Jönsson, A., Lake, I., Döös, K., Hieronymus, M., Dietze, H., Haapala, J. (2019). *Nemo-Nordic 1.0: a NEMO-based ocean model for the Baltic and North seas – research and operational applications. Geoscientific Model Development, 12(1), 363–386.* https://doi.org/10.5194/gmd-12-363-2019
- Horvat, C., Tziperman, E. (2015). *A prognostic model of the sea-ice floe size and thickness distribution, the Cryosphere, 9(6), 2119–2134.* https://doi.org/10.5194/tc-9-2119-2015
- Hwang, B., Ren, J., McCormack, S., Berry, C., Ayed, I. B., Graber, H. C., Aptoula, E. (2017). *A practical algorithm for the retrieval of floe size distribution of Arctic sea ice from high-resolution*

satellite Synthetic Aperture Radar imagery. Elementa Science of the Anthropocene, 5. https://doi.org/10.1525/elementa.154

- Iovino, D., Storto, A., Masina, S., Cipollone, A., Stepanov, V. (2014). *GLOB16, the CMCC Global Mesoscale-Eddying Ocean. SSRN Electronic Journal*. https://doi.org/10.2139/ssrn.2603170
- Karvonen, J. A., Cheng, B. (2024). *Baltic sea ice thickness estimation based on X-band SAR data and background information. Annals of Glaciology, 1–11.* https://doi.org/10.1017/aog.2024.24
- Leppäranta, M. (2011). *The drift of sea ice. Springer.*
- Lietuvos Respublikos energetikos ministerija. (2023, October 6). *Wind speed measurement: The Baltic Sea offers favourable conditions for the development of wind farms. LRV.LT.* https://enmin.lrv.lt/en/news/wind-speed-measurement-the%-baltic-sea-offers-favourable-conditions-for-the-development-of-wind-farms/
- Lilover, M. -j. (2012). *Tidal currents as estimated from ADCP measurements in "practically non-tidal" Baltic Sea. 2012 IEEE/OES Baltic International Symposium (BALTIC), 1–4.* https://doi.org/10.1109/baltic.2012.6249181
- Lu, P., Li, Z., Cheng, B., Leppäranta, M. (2011). *A parameterization of the ice□ocean drag coefficient. Journal of Geophysical Research Atmospheres, 116(C7).* https://doi.org/10.1029/2010jc006878
- Lu, W., Lubbad, R., Løset, S. (2014). *In-plane fracture of an ice floe: A theoretical study on the splitting failure mode. Cold Regions Science and Technology, 110, 77–101.* https://doi.org/10.1016/j.coldregions.2014.11.007
- Medvedev, I. P., Rabinovich, A. B., Kulikov, E. A. (2013). *Tidal oscillations in the Baltic Sea. Oceanology, 53(5), 526–538.* https://doi.org/10.1134/s0001437013050123
- Meier, H. E. M., Dieterich, C., Gröger, M., Dutheil, C., Börgel, F., Safonova, K., Christensen, O. B., Kjellström, E. (2022). *Oceanographic regional climate projections for the Baltic Sea until 2100. Earth System Dynamics, 13(1), 159–199.* https://doi.org/10.5194/esd-13-159-2022
- Metrikin, I. (2014). *A software framework for simulating stationkeeping of a vessel in discontinuous ice. Model. Identif. Control: Norwegian Resear. Bull., 35 (4):211–248.* http://hdl.handle.net/11250/2392045
- Metrikin, I., Gürtner, A., Bonnemaire, B., Tan, X., Fredriksen, A., Sapelnikov, D. (2015). *SIBIS: a numerical environment for simulating offshore operations in discontinuous ice. Proceedings of the International Conference on Port and Ocean Engineering Under Arctic Conditions.* https://trid.trb.org/view/1429255
- Nakayama, Y., Ohshima, K. I., Fukamachi, Y. (2011). *Enhancement of Sea Ice Drift due to the Dynamical Interaction between Sea Ice and a Coastal Ocean. Journal of Physical Oceanography, 42(1), 179–192.* https://doi.org/10.1175/jpo-d-11-018.1
- NREL. (2023, June). *Tahkoluoto offshore wind farm grown-in by sea ice. nrel.gov.* https://www.nrel.gov/news/program/2023/exploring-offshore-wind-energy-opportunities-in-the-great-lakes.html
- N. Serre, S. Kerkeni, C. Peyrega, M. Rabatel, D. Sapelnikov, and A. Ervik (2019).*Numerical simulation of broken ice interaction with offshore structures: validation exercises. In Proc. of 25th International Conference on Port and Ocean under Arctic Conditions (POAC'19)(Delft, The Netherlands).*
- Paquette, E., Brown, T. G. (2017). *Ice crushing forces on offshore structures: Global effective pressures and the ISO 19906 design equation. Cold Regions Science and Technology, 142, 55–68.* https://doi.org/10.1016/j.coldregions.2017.07.010
- Perovich, D. K., Jones, K. F. (2014). *The seasonal evolution of sea ice floe size distribution. Journal of Geophysical Research Oceans, 119(12), 8767–8777.* https://doi.org/10.1002/2014jc010136

- Persson, A. (2000). *Back to basics: Coriolis: Part 1 — What is the Coriolis force? Weather, 55(5), 165–170.* https://doi.org/10.1002/j.1477-8696.2000.tb04052.x
- Petty, A. A., Tsamados, M. C., Kurtz, N. T. (2017). *Atmospheric form drag coefficients over Arctic sea ice using remotely sensed ice topography data, spring 2009–2015. Journal of Geophysical Research Earth Surface, 122(8), 1472–1490.* https://doi.org/10.1002/2017jf004209
- Roach, L. A., Bitz, C. M., Horvat, C., Dean, S. M. (2019). *Advances in modeling interactions between sea ice and ocean surface waves. Journal of Advances in Modeling Earth Systems, 11(12), 4167–4181.* https://doi.org/10.1029/2019ms001836
- Roach, L. A., Horvat, C., Dean, S. M., Bitz, C. M. (2018). *An emergent sea ice floe size distribution in a global coupled Ocean□Sea Ice model. Journal of Geophysical Research Oceans, 123(6), 4322–4337.* https://doi.org/10.1029/2017jc013692
- Siemens Gamesa Renewable Energy. (2018). *Nissum Bredning Offshore Wind Farm.*
- Sinsabvarodom, C., Chai, W., Leira, B. J., Høyland, K. V., Næss, A. (2022). *Ice rose diagrams for probabilistic characterization of the ice drift behavior in the Beaufort Sea. Ocean Engineering, 266, 112708.* https://doi.org/10.1016/j.oceaneng.2022.112708
- Sinsabvarodom, C., Leira, B. J., Høyland, K. V., Næss, A., Chai, W. (2024). *A generalized ice drift spectrum based on measurements in the Beaufort Sea. Ocean Engineering, 296, 116832.* https://doi.org/10.1016/j.oceaneng.2024.116832
- Soomere, T., Weisse, R., Behrens, A. (2012). *Wave climate in the Arkona Basin, the Baltic Sea. Ocean Science, 8(2), 287–300.* https://doi.org/10.5194/os-8-287-2012
- Stern, H. L., Schweiger, A. J., Stark, M., Zhang, J., Steele, M., Hwang, B. (2018). *Seasonal evolution of the sea-ice floe size distribution in the Beaufort and Chukchi seas. Elementa Science of the Anthropocene, 6.* https://doi.org/10.1525/elementa.305
- Stern, H. L., Schweiger, A. J., Zhang, J., Steele, M. (2018). *On reconciling disparate studies of the sea-ice floe size distribution. Elementa Science of the Anthropocene, 6.* https://doi.org/10.1525/elementa.304
- Team Renewable Arctic Finland. (2021, June 29). *Offshore wind turbines in the Bothnian Bay encouter drifting sea ice. teamrenewablearctic.fi.* https://teamrenewablearctic.fi/2021/06/29/better-understanding-of-ice-is-essential-when-planning-offshore-wind-in-the%-northern-baltic-sea/
- Ten Broecke, P. (2016, February 11). *High concentration floe field in the Arctic. scientificamerican.com.* https://www.scientificamerican.com/article/arctic-sea-ice%-hits-new-january-low/
- Tikanmäki, M., Heinonen, J. (2021). *Estimating extreme level ice and ridge thickness for offshore wind turbine design: Case study Kriegers Flak. Wind Energy, 25(4), 639–659.* https://doi.org/10.1002/we.2690
- Timco, G., Weeks, W. (2009). *A review of the engineering properties of sea ice. Cold Regions Science and Technology, 60(2), 107–129.* https://doi.org/10.1016/j.coldregions.2009.10.003
- Van Den Berg, M., Lubbad, R., Løset, S. (2019). *The effect of ice floe shape on the load experienced by vertical-sided structures interacting with a broken ice field. Marine Structures, 65, 229–248.* https://doi.org/10.1016/j.marstruc.2019.01.011
- Van der Stap, F. L., Nielsen, M. B., Hendrikse, H. (2024). *A preliminary assessment of frozen-in offshore wind turbines. In T. Kolerski (Ed.), Proceedings of the 27th IAHR International Symposium on Ice (Gdansk, 2024) Article 30378 (IAHR International Symposium on Ice). IAHR.* https://www.iahr.org/library/infor?pid=30378
- Vautard, R., Van Oldenborgh, G. J., Otto, F. E. L., Yiou, P., De Vries, H., Van Meijgaard, E., Stepek, A., Soubeyroux, J., Philip, S., Kew, S. F., Costella, C., Singh, R., Tebaldi, C. (2019). *Human influence on European winter wind storms such as those of January 2018. Earth System Dynamics, 10(2), 271–286.* https://doi.org/10.5194/esd-10-271-2019

- Virkar, Y., Clauset, A. (2014). *Power-law distributions in binned empirical data. The Annals of Applied Statistics, 8(1).* https://doi.org/10.1214/13-aoas710
- Wagner, T. J. W., Eisenman, I., Ceroli, A. M., Constantinou, N. C. (2022). *How winds and ocean currents influence the drift of floating objects. Journal of Physical Oceanography, 52(5), 907–916.* https://doi.org/10.1175/jpo-d-20-0275.1
- Zhang, Q., Skjetne, R. (2014). *Image processing for identification of Sea-Ice floes and the floe size distributions. IEEE Transactions on Geoscience and Remote Sensing, 53(5), 2913–2924.* https://doi.org/10.1109/tgrs.2014.2366640
- Zhang, W., Harff, J., Schneider, R. (2011). *Analysis of 50-year wind data of the southern Baltic Sea for modelling coastal morphological evolution – a case study from the Darss-Zingst Peninsula. Oceanologia, 53, 489–518.* https://doi.org/10.5697/oc.53-1-ti.489
- Zhou, L., Cai, J., Ding, S. (2023). *The identification of ice floes and calculation of sea ice concentration based on a deep learning method. Remote Sensing, 15(10), 2663.* https://doi.org/10.3390/rs15102663

A
Appendix

A.1. Conversion Image Dimensions From Pixels To Meters

The code in this section explains how the pixel dimensions from the image processing results can be converted to meters to correctly scale the images from the Copernicus Browser. This requires exporting the the imagery from the Copernicus Browers in TIFF format. The code can be run after the image processing code from Denton et al. (2022) has been executed.

```
% Extract geospatial data
stats = regionprops(L, 'Area');
info = geotiffinfo(imName);

% Convert pixels from TIFF image to meters
deg_to_rad = pi / 180; % Conversion factor from degrees to radians
pixelSizeX = info.PixelScale(1) * 111320 * cos(60 * deg_to_rad);
pixelSizeY = info.PixelScale(2) * 110570
areas = [stats.Area];
areas = areas(:);
areas = areas * pixelSizeY * pixelSizeX;
```

A.2. Conversion Floe Outlines From Floe Field Generator to XML-format SIBIS

The code from Brenner (2024) creates a MATLAB matrix of floe outlines for each floe with as a list of x- and y-coordinates. This code converts the matrix to an XML-format that can be read by SIBIS.

```
% XML file name
xmlFileName = 'ijsveld_SIC0.80_80_300_12x12km.xml';

% Create XML document
docNode = com.mathworks.xml.XMLUtils.createDocument('Floes');
rootElement = docNode.getDocumentElement();

% Loop through each floe outline
for i = 1:numel(floeOutlines)
    currentOutline = floeOutlines{i}; % Access matrix in cell
    if isempty(currentOutline)
        continue; % Skip empty outlines
    end
    xCoords = currentOutline(:, 1); % First column is x
    yCoords = currentOutline(:, 2); % Second column is y

    % Create Floe element
    floeElement = docNode.createElement('Floe');
    floeElement.setAttribute('value', num2str(i));

    % Create Vertices element
```

```
    verticesElement = docNode.createElement('Vertices');

    % Loop through each row of x and y coordinates
    for j = 1:size(currentOutline, 1)
        % Create Vertex element
        vertexElement = docNode.createElement('Vertex');
        vertexElement.setAttribute('x', num2str(xCoords(j), '%.6f'));
        vertexElement.setAttribute('y', num2str(yCoords(j), '%.6f'));

        % Append Vertex to Vertices
        verticesElement.appendChild(vertexElement);
    end

    % Append Vertices to Floe
    floeElement.appendChild(verticesElement);

    % Append Floe to root
    rootElement.appendChild(floeElement);
end

% Write the XML document to a file
xmlwrite(xmlFileName, docNode);

disp(['XML file created: ' xmlFileName]);
```

A.3. Write Floe Outlines to Counterclockwise Order

The floe outlines should be defined in a counterclockwise order before they can be read by SIBIS. This code therefore rearranges the floe outlines in XML-format to a counterclockwise order. This is a continuation of the code in Section A.2.

```
% Load the XML file
xmlFileName = 'ijsveld_SIC0.60_80_300_12x12km.xml';
docNode = xmlread(xmlFileName);

% Extract the Floe elements
floes = docNode.getElementsByTagName('Floe');

% Function to calculate the signed area of a polygon
function area = signedPolygonArea(vertices)
    % Shoelace formula
    x = vertices(:, 1);
    y = vertices(:, 2);
    area = 0.5 * sum(x .* circshift(y, -1) - y .* circshift(x, -1));
end

% Loop through each Floe
for i = 0:floes.getLength-1
    floe = floes.item(i);
    vertices = floe.getElementsByTagName('Vertex');
    nVertices = vertices.getLength;

    % Initialize an empty array for coordinates
    coords = [];

    % Extract coordinates
```

```
    for j = 0:nVertices-1
        vertex = vertices.item(j);
        xStr = char(vertex.getAttribute('x'));
        yStr = char(vertex.getAttribute('y'));

        % Check if attributes are valid numbers
        if isempty(xStr) || isempty(yStr)
            warning('Skipping vertex with missing attributes in Floe %d.',
                i+1);
            continue;
        end

        x = str2double(xStr);
        y = str2double(yStr);

        if isnan(x) || isnan(y)
            warning('Skipping vertex with invalid attributes in Floe %d.',
                i+1);
            continue;
        end

        coords = [coords; x, y]; %#ok<AGROW> Concatenate valid coordinates
    end

    % Skip empty coordinate sets
    if isempty(coords)
        warning('Floe %d has no valid vertices.', i+1);
        continue;
    end

    % Calculate signed area
    signedArea = signedPolygonArea(coords);

    % Reverse order if area is negative (clockwise orientation)
    if signedArea < 0
        coords = flipud(coords); % Reverse the order of vertices
    end

    % Update the XML file with the new coordinate order
    for j = 0:size(coords, 1)-1
        vertex = vertices.item(j);
        vertex.setAttribute('x', num2str(coords(j+1, 1), '%.6f'));
        vertex.setAttribute('y', num2str(coords(j+1, 2), '%.6f'));
    end
end

% Save the updated XML document
updatedXmlFileName = 'ijsveld_SIC0.60_80_300_12x12km_CounterClock.xml';
xmlwrite(updatedXmlFileName, docNode);

disp(['Updated XML file created: ' updatedXmlFileName]);
```